Femtosecond Laser-based investigations of Magnetic Circular Dichroism in near-threshold Photoemission

Dissertation in Physics
to obtain the degree of
"Doktor der Naturwissenschaften"
at the Department of Physics
Johannes Gutenberg University Mainz

Kerstin Hild
born in Weilburg (Germany)
Mainz, April 28, 2011

Supervisor:
Referees:

Day of Defense: July 21, 2011

Abstract

During the last decades magnetic circular dichroism (MCD) has attracted much interest and evolved into various experimental methods for the investigation of magnetic thin films. For example, synchrotron-based X-ray magnetic circular dichroism (XMCD) displays the absolute values of spin and orbital magnetic moments. It thereby benefits from large asymmetry values of more than 30 % due to the excitation of atomic core-levels. Similarly large values are also expected for threshold photoemission magnetic circular dichroism (TPMCD). Using lasers with photon energies in the range of the sample work function this method gives access to the occupied electronic structure close to the Fermi level. However, except for the case of Ni(001) there exist only few studies on TPMCD moreover revealing much smaller asymmetries than XMCD-measurements. Also the basic physical mechanisms of TPMCD are not satisfactorily understood.

In this work we therefore investigate TPMCD in one- and two-photon photoemission (1PPE and 2PPE) for ferromagnetic Heusler alloys and ultrathin Co films using ultrashort pulsed laser light. The observed dichroism is explained by a non-conventional photoemission model using spin-resolved band-structure calculations and linear response theory.

For the two Heusler alloys Ni_2MnGa and Co_2FeSi we give first evidence of TPMCD in the regime of two-photon photoemission. Systematic investigations concerning general properties of TPMCD in 1PPE and 2PPE are carried out at ultrathin Co films grown on Pt(111). Here, photon-energy dependent measurements reveal asymmetries of 1.9 % in 1PPE and 11.7 % in 2PPE. TPMCD measurements at decreased work function even yield larger asymmetries of 6.2 % (1PPE) and 17 % (2PPE), respectively. This demonstrates that enlarged asymmetries are also attainable for the TPMCD effect on Co(111). Furthermore, we find that the TPMCD asymmetry is bulk-sensitive for 1PPE and 2PPE. This means that the basic mechanism leading to the observed dichroism must be connected to Co bulk properties; surface effects do not play a crucial role. Finally, the enhanced TPMCD asymmetries in 2PPE compared to the 1PPE case are traced back to the dominant influence of the first excitation step and the existence of a real intermediate state.

The observed TPMCD asymmetries cannot be interpreted by conventional photoemission theory which only considers direct interband transitions in the direction of observation (Γ-L). For Co(111), these transitions lead to evanescent final states. The excitation to such states, however, is incompatible with the measured bulk-sensitivity of the asymmetry. Therefore, we generalize this model by proposing the TPMCD signal to arise mostly from direct interband transitions in crystallographic directions other than (Γ-L). The necessary additional momentum transfer to the excited electrons is most probably provided by electron-phonon or -magnon scattering processes. Corresponding calculations on the basis of this model are in reasonable agreement with the experimental results so that this approach represents a promising tool for a quantitative description of the TPMCD effect.

The present findings encourage an implementation of our experimental technique to time- and spatially-resolved photoemission electron microscopy, thereby enabling a real time imaging of magnetization dynamics of single excited states in a ferromagnetic material on a femtosecond timescale.

Kurzfassung

Während der letzten Jahrzehnte hat sich der Magnetische Zirkulardichroismus (MCD) zu einer vielseitigen und unverzichtbaren Methode zur Untersuchung magnetischer dünner Schichten entwickelt. So liefert beispielsweise der Röntgenzirkulardichroismus (XMCD) durch die Anregung kernnaher Elektronenniveaus absolute Werte für das magnetische Spin- und Bahnmoment und profitiert dabei von hohen Asymmetriewerten von mehr als 30 %. Ähnlich hohe Werte verspricht auch der Magnetische Zirkulardichroismus in der Schwellen-Photoemission (TPMCD), bei dem Laser mit Photonenenergien im Bereich der Proben-Austrittsarbeit verwendet werden, um Informationen über die besetzte elektronische Struktur in der Nähe der Fermi-Kante zu erhalten. Abgesehen von Messungen an Ni(001) existierten bisher jedoch nur wenige Untersuchungen zum TPMCD-Effekt. Diese wiesen zudem weitaus kleinere Asymmetriewerte auf als XMCD-Messungen und der zugrunde liegende physikalische Mechanismus ist noch nicht hinreichend verstanden.
In dieser Arbeit wird der TPMCD-Effekt in Ein-Photon-Photoemission und Zwei-Photonen-Photoemission (1PPE und 2PPE) an ferromagnetischen Heusler-Schichten und Co-Dünnfilmen mit Hilfe von Ultrakurzpulslasern untersucht. Die beobachteten Asymmetrien werden durch ein neues Photoemissionsmodell erklärt, das auf Spin-aufgelösten Bandstrukturrechnungen und einem linearen Response-Formalismus basiert.
Für die beiden Heusler-Legierungen Ni_2MnGa und Co_2FeSi weisen wir den TPMCD-Effekt erstmals im 2PPE-Regime nach. Systematische Untersuchungen zu generellen Eigenschaften des Dichroismus werden an ultradünnen Co-Filmen auf Pt(111) durchgeführt. Hierbei ergeben Messungen in Abhängigkeit der Photonenenergie Asymmetrien von 1.9 % für 1PPE und 11.7 % für 2PPE. TPMCD-Messungen bei gesenkter Austrittsarbeit liefern sogar noch höhere Asymmetrien von 6.2 % (1PPE) bzw. 17 % (2PPE). Dies macht deutlich, dass auch für den TPMCD-Effekt an Co(111) hohe Asymmetriewerte erreicht werden können. Die Messungen zeigen weiterhin, dass die TPMCD-Asymmetrie eine volumen-sensitive Größe ist: Die Entstehung des Dichroismus wird offenbar wesentlich durch die Volumeneigenschaften des Co beeinflusst, Oberflächeneffekte spielen hingegen eine untergeordnete Rolle. Darüber hinaus kann die in allen Messungen gegenüber 1PPE erhöhte 2PPE-Asymmetrie auf einen dominanten Einfluss des ersten Anregungsschrittes und die Existenz eines realen Zwischen-Niveaus zurückgeführt werden.
Die beobachteten TPMCD-Effekte lassen sich nicht mit der herkömmlichen Photoemissions-Theorie erklären, die nur direkte Interband-Übergänge in Beobachtungsrichtung (Γ-L) berücksichtigt. Für Co(111) führen diese in evaneszente Endzustände. Die Anregung in solche ist jedoch unvereinbar mit der gemessenen Volumensensitivität der TPMCD-Asymmetrien. Daher erweitern wir dieses Modell, indem wir den Dichroismus auf direkte Interband-Übergänge in anderen kristallographischen Richtungen als (Γ-L) zurückführen. Der dabei zur Elektronenemission benötigte zusätzliche Impulsübertrag wird vermutlich durch Elektron-Phonon/ Magnon-Streuprozesse bereitgestellt. Entsprechende Rechnungen auf Grundlage dieses Modells liefern Asymmetrien, die für 1PPE und 2PPE in guter Übereinstimmung mit den gemessenen Werten sind, so dass dieser Zugang die Möglichkeit einer quantitativen Beschreibung des TPMCD-Effektes eröffnet.
Die gegenwärtigen Ergebnisse stellen zeit- und ortsaufgelöste Photoemissionselektronenmikroskopie-Untersuchungen in Aussicht, mit deren Hilfe die Magnetisierungsdynamik angeregter Einzelzustände in ferromagnetischen Materialien mit einer Zeitauflösung im Femtosekundenbereich beobachtet werden kann.

Contents

1 Introduction

The phenomenon of circular dichroism caused by different absorption probabilities for circularly left and circularly right polarized light in suitable materials appears in living nature in surprisingly diverse forms and beautiful coloring. Such interactions with light can be observed for beetles, many birds as well as butterflies. Thus, especially the dazzling beetles have been traditionally used in many Asian countries for the decoration of textiles before they also attracted strong scientific interest [1]. During the last centuries dichroic effects have been investigated for many more objects such as special crystals and chiral molecules. In this context, it was also shown that they do not only appear in non-magnetic structures but are also present in ferromagnetic materials for which they are systematically investigated since the discovery of the photoelectric effect.
In photoemission excited by linearly or circularly polarized light the detected spin-averaged photocurrent of a magnetized material reveals an asymmetry upon reversal of the photon helicity. This phenomenon is called magnetic linear/circular dichroism (MLD/MCD) and originates from the simultaneous presence of spin-orbit coupling (SOC) and exchange splitting in ferromagnets. Since both effects strongly influence the electronic structure of a material MCD measurements deliver plenty of information on the electronic properties of magnetic thin films and surfaces. During the last decades magnetic dichroic effects have thus attracted much interest and have therefore been investigated mainly in two photon energy regimes.
X-ray magnetic circular dichroism (XMCD) uses synchrotron radiation with photon energies between 400-1000 eV to excite electrons from the core levels of a magnetic material. The corresponding measurements provide element specific information, i. a. by displaying the absolute values of spin and orbital magnetic moments [2, 3]. Since XMCD is based on the excitation of discrete atomic core levels with a large spin-orbit coupling it benefits from large asymmetry values of more than 30 % [4] and can therefore also be used as a contrast mechanism for magnetic domain imaging by means of photoemission electron microscopy [5].
In contrast, magnetic circular dichroism in valence band photoemission (MCD) excites electrons from the valence band region of a material using photon energies in the range of 5 to 40 eV. It therefore gives immediate access to the relativistic band structure of a ferromagnet. Especially augmented to energy- and angle-resolved photoemission spectroscopy, MCD in valence band photoemission is able to map the dispersion of single initial-state valence bands and to derive their relativistic symmetry character from the dichroic spectra [6]. Furthermore, it allows for direct insights into spin-orbit induced hybridization effects in the band-structure scheme and measures the strength of spin-orbit coupling as well as exchange splitting [7].
In contrast to the development of MCD in valence band photoemission to a powerful experimental technique, it is only scarcely investigated in the regime of threshold photoemission where the photon energy is only slightly larger than the sample work function ($h\nu \sim 2.5$ -

6 eV). The electrons are therefore excited from occupied initial states close to the Fermi energy to final states slightly above the vacuum level. This means that only a small region of initial states contributes to the signal. Accordingly, MCD in near-threshold photoemission would deliver insight into the electronic structure in the direct vicinity of the Fermi level. In this sense, it might also favor enlarged asymmetries due to a strong selection of participating bands. However, until a few years ago only little work was performed on magnetic dichroism in near-threshold photoemission.
Using a mercury arc lamp ($h\nu < 5$ eV) Marx et al. demonstrated magnetic linear dichroism in one-photon photoemission electron microscopy (PEEM) for a 100 nm thick polycrystalline Fe film revealing a much smaller asymmetry of 0.37 % compared to XMCD measurements [8]. A more auspicious access to near-threshold magnetic dichroism is provided by the use of tunable ultrashort pulse lasers instead of conventional laboratory light sources. The former do not only possess the required photon energies, but they also pioneer experiments in the regime of multi-photon photoemission enabling completely new excitation mechanisms beyond conventional photoemission. In this context, recent measurements by Nakagawa and Yokoyama have shown that near-threshold MCD asymmetries of the order of 10 % in one-photon photoemission can be obtained for perpendicularly magnetized Ni films on Cu(001) using ultrashort pulsed laser light [9]. These experiments point out that enlarged MCD asymmetries are also attainable in near-threshold photoemission and strongly encourage systematic investigations of other magnetic materials. The findings moreover motivate the inspection of MCD in the multi-photon photoemission regime. The detection of enhanced asymmetries for one- as well as for two-photon photoemission might pave the way for the imaging of magnetization dynamics in threshold photoemission with maximum spatial and time resolution using ultrashort pulsed lasers in combination with microscopy techniques such as PEEM. This would also display the potential of near-threshold MCD for magnetic storage technology. Experiments following the investigations of Ni(001) would not only aim at searching for large magnetic asymmetries in one- and multi-photon photoemission processes, but the investigations should also yield information about the underlying physical mechanisms of MCD in near-threshold photoemission which are not yet satisfactorily understood.
In the framework of this thesis we investigate near-threshold MCD in one- and two-photon photoemission (1PPE and 2PPE) for ferromagnetic Heusler alloys and ultrathin Co films using ultrashort pulsed laser light. For the two Heusler alloys we will give first evidence of near-threshold MCD in the regime of 2PPE. The ultrathin Co films grown on Pt(111) are used for systematic investigations concerning the dependence of the 1PPE- and 2PPE-MCD on the photon energy and the angle of light incidence. Moreover, the dependence on the thickness of the magnetic film and the magnetic anisotropy as well as on the sample work function is investigated for 1PPE and 2PPE. The use of Co/Pt samples is advantageous since they constitute well-studied systems revealing a high perpendicular magnetic anisotropy and large magneto-optical Kerr effects. For the investigation of MCD they are of special interest since Co exhibits a large exchange-splitting, and Pt reveals an enhanced spin-orbit coupling. The results for Co/Pt(111) will demonstrate that large MCD effects in near-threshold photoemission are also possible for other materials than Ni(001). Furthermore, we will comment on

the sensitivity of the measured asymmetries with respect to the bulk and the surface of the Co sample. Additionally, the influence of the two excitation steps in a 2PPE process is explicitly analyzed. Based on the experimental findings we will furthermore give an interpretation of the MCD asymmetries in terms of direct interband transitions in the band-structure scheme of Co(111). In particular, we will show that the conventional model of photoemission that only considers transitions in the direction of normal electron emission cannot be applied to the case of Co(111). Instead, we will generalize this approach to a model which includes transitions in all other crystallographic directions of the band-structure scheme. Calculations on basis of this theory will be directly compared to our experimental findings.

This work is organized as follows:

In **Chapter 2** we describe the relevant theoretical concepts. Thereby, we mainly focus on the two physical phenomena of photoemission and magnetic circular dichroism which are discussed in Ch. 2.1 and Ch. 2.2, respectively. Ch. 2.3 additionally illustrates the theoretical approach used for the calculation of the MCD asymmetries. Please note that in contrast to existing publications we will not use the term *threshold photoemission magnetic circular dichroism* (TPMCD) in this work. Strictly speaking TPMCD means magnetic circular dichroism measured directly at the photoemission threshold which applies only to some of our investigations. In literature this term is used to easily distinguish these excitation processes from those of XMCD on the one hand and from MCD in conventional valence band photoemission on the other hand. To be as precise as possible, we therefore use the terms *MCD in near-threshold photoemission* and *near-threshold MCD* for dichroic signals measured in the vicinity of the threshold ($h\nu - \Phi \leq 1\,\mathrm{eV}$).

In **Chapter 3** we describe the experimental techniques. Since the measurements for this thesis have been carried out at the University of Mainz as well as at the Institute for Molecular Science in Okazaki (Japan), both setups for the detection of magnetic circular dichroism in near-threshold photoemission and for the magneto-optical Kerr effect are described.

In **Chapter 4** we present and discuss the experimental results. The chapter is divided into four sections, each dealing with a different issue in the framework of near-threshold MCD. In order to present each section as self-contained as possible from the previous ones each starts with its own motivation and ends with a summary and conclusions.

In **Chapter 5** we summarize the results of this work and illuminate the scientific findings which can be drawn from their interpretation.

2 Theoretical foundations

In this chapter we describe the physical mechanisms that underly the experimental results. Since magnetic circular dichroism is investigated using photoemission we present the basic theoretical concepts behind both phenomena.
In the field of photoemission we mainly turn our attention to the most important theoretical approaches, namely the three-step and the one-step model. The characteristics and differences of the two approaches are presented and the meaning of both concepts with respect to this work is illuminated. Also multi-photon photoemission processes, in particular two-photon photoemission (2PPE), and the regime of threshold photoemission are qualitatively discussed in this section.
To understand the origin of MCD we firstly introduce the irreducible representations of the electronic states as well as the dipole selection rules. The MCD is then derived from direct interband transitions between initial and final electronic states in the band-structure scheme. This is explicitly carried out for the case of the (111) surface, at the same time demonstrating that MCD is caused by the simultaneous presence of spin-orbit coupling and exchange-splitting.
The last section is devoted to *ab initio* calculations of the MCD asymmetry which are carried out in strong analogy to a model also used for the magneto-optical Kerr effect, additionally considering the energy conservation for the photoemitted electrons. Thereby, we mainly focus on the bandstructure calculations and the evaluation of the optical conductivity tensor which are both essential for the derivation of the MCD signals. The MCD asymmetry is then directly expressed in terms of the optical conductivity.

2.1 The Theory of Photoemission

2.1.1 Einstein equation

The first description of photoemission was given by Einstein in 1905 [10]. In the photoelectric effect a material emits electrons, when it is illuminated with light of particular energy. Due to the disagreement with Maxwell's wave theory of light Einstein proposed that only by the absorption of discrete light quanta (photons) of appropriate energy the electrons can escape from the material. Thereby, the number of these photoelectrons increases with increasing light intensity, while their kinetic energy is proportional to the frequency of the incident radiation. These findings lead to the Einstein equation describing the energy balance of a photoemission process,

$$E_{\mathrm{kin}} = h\nu - \Phi - E_{\mathrm{B}}, \tag{2.1}$$

where hν is the energy of a photon; Φ is the work function of the material resembling a potential barrier which has to be overcome by the electron. The binding energy of an electron is denoted by $E_{\mathrm{B}}(>0)$, and E_{kin} describes the electron's kinetic energy in vacuum. In the days of Einstein knowledge was restricted to Eq. (2.1) and its implications. Other photoelectric regimes such as multi-photon photoemission (e. g. two-photon photoemission) have not been possible until the advent of ultrashort pulse lasers. Since this issue is very important for the experiments that will be discussed in this thesis we briefly recall its basic characteristics.

One-and two-photon photoemission processes

The process of one-photon photoemission is directly captured by the Einstein equation. The left side of Fig. 2.1 depicts a sketch of a 1PPE process: An electron is excited from an initial state of energy E_i to a final state E_f by absorbing one photon of energy hν. To escape into vacuum the electrons have to overcome the vacuum level E_{V}. Thereby, the energetic difference between E_{V} and the Fermi level E_{F} is the sample work function, $\Phi = E_{\mathrm{V}} - E_{\mathrm{F}}$, while $E_{\mathrm{B}} = |E_i - E_{\mathrm{F}}|$ marks the electron's binding energy. Fig. 2.1 and Eq. (2.1) also show that for a 1PPE process the photon energy must be larger than the sample work function implying $E_{\mathrm{kin}} \geq 0$; otherwise the process cannot take place. With the present-day availability of high photon fluences and excellent focusing conditions multi-photon processes also enable photoemission with h$\nu < \Phi$. For this work especially two-photon photoemission is of great importance.
In a 2PPE process the electron absorbs a first photon and is excited to a real $|r\rangle$ or virtual $|v\rangle$ intermediate state. By absorbing a second photon of the same laser pulse the electron is excited to a final state E_f above the vacuum level (see the right side of Fig. 2.1). The lifetime of a real intermediate state depends on the excitation energy and can be determined in experiments. One finds for the lifetime τ [11, 12]

$$\tau \sim \frac{1}{(E^* - E_{\mathrm{F}})^2}, \tag{2.2}$$

where E^* is the energy of the real intermediate state. Typical values lie between 1-30 fs [11]. Emission is triggered effectively, if the lifetime of the real intermediate state is large, i. e. if the energetic difference $(E^* - E_{\mathrm{F}})$ is small. Therefore, excitation into unoccupied real states close to the Fermi edge is advantageous. The lifetime of virtual intermediate states is expected to be much smaller which might be shown by future experiments. The general difference between excitations into a real and a virtual intermediate state is often expressed as the sum of two terms in the electron distribution per time and volume interval which is formed after the optical excitation [13]:

$$P^{2\mathrm{p}}(E,\omega) = P^{\mathrm{c}}(E,\omega) + P^{\mathrm{s}}(E,\omega). \tag{2.3}$$

While the first term marks a sequential process (c stands for cascade), the second one describes simultaneous excitations (s for simultaneous). These are characterized by electronic excitations into virtual intermediate states upon absorption of the first photon. The simultaneous absorption of a second photon triggers the transition to a final state E_f. In contrast to

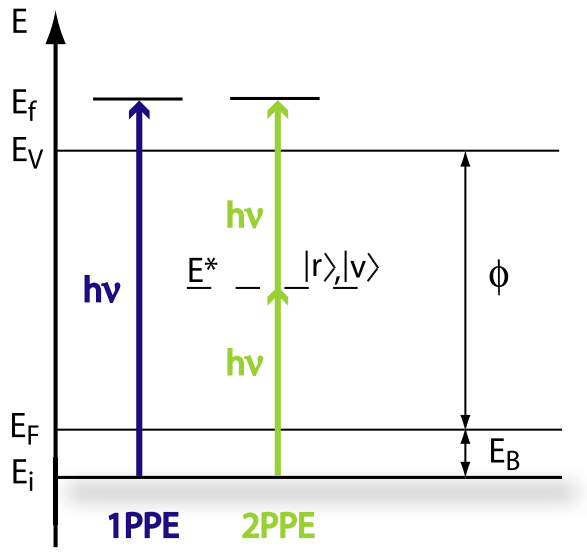

Figure 2.1: (left side) Sketch of a one-photon photoemission process. E_i marks the initial state from which an electron is excited to a final state E_f by absorbing a photon of energy hν. Thereby, it has to overcome the vacuum level E_V. (right side) Schematic view of a two-photon photoemission process. An electron is excited into vacuum by absorbing two photons of the same laser pulse (2h$\nu > \Phi$). The intermediate state carries the energy E^* and can be real $|r\rangle$ or virtual $|v\rangle$; $|E_i - E_\mathrm{F}|$ reflects the binding energy E_B, $E_\mathrm{V} - E_\mathrm{F}$ is the sample work function Φ. $E_f - E_\mathrm{V}$ is the photoelectron's kinetic energy.

the coherent simultaneous excitations, sequential excitations proceed in an incoherent manner. This means that the electrons are firstly excited to a real intermediate state where they can form a so-called hot-electron distribution. This distribution temporally changes by different relaxation processes before the second photon is absorbed. The most common relaxation process on a femtosecond time scale is electron-electron scattering. Generally, the relaxation produces secondary electrons which populate states between $|r\rangle$ and $|E_\mathrm{F}\rangle$ and can contribute to the 2PPE spectrum.

Threshold photoemission

In the regime of threshold photoemission the photon energy is just slightly higher than the sample work function, meaning h$\nu \geq \Phi$ for a single photon process. The electrons still escape from the material, but following Eq. (2.1) they only exhibit a narrow distribution of kinetic energies. With respect to the universal curve [14] this also means that their inelastic mean free path is enhanced, and the electrons mostly stem from the bulk of the material. For some materials such as Ni(001) it was demonstrated that magnetic circular dichroism is especially enlarged at the photoemission threshold and rapidly decreases in the vicinity of the threshold [9] which is attributed to band-structure effects. The enhancement of MCD asymmetry directly at threshold also explains the interest in investigating MCD in near-threshold photoemission.

2.1.2 The three-step model

After the first description of the photoelectric effect different theoretical models have been developed to analyze the process in detail. An extensive summary of the different concepts and related phenomena is given in Ref. [15] to which the following sections mainly refer. In all concepts one generally distinguishes between *core level photoemisssion* which means the excitation of photoelectrons out of atomic core levels using soft or hard X-rays and *valence band photoemission* commonly carried out at much lower photon energies, e. g. in the UV-range. Since this work is not related to the previous one we will refer only to the case of valence band photoemission. All theories of photoemission have to describe the excitation of many electrons from initial states and their escape into vacuum leaving the remaining system in a modified final state. Thus they are dealing with a complicated *many-body process*. In the regime of valence band photoemission an electron is excited from a valence state and creates a hole in the sea of valence electrons. The creation of a photohole is analog to adding a positive potential to which the remaining system might react. This response, also known as *screening*, is assumed to be instantaneous, and a possible interaction between the photoelectron and the rest of the system is neglected. This assumption arising in all photoemission theories is called the *sudden approximation*.
After this preliminary remarks we introduce the so-called *three-step model* which is the most frequently used concept for a photoemission process. This phenomenological approach was introduced by Berglund and Spicer [16] and - although not completely correct - successfully

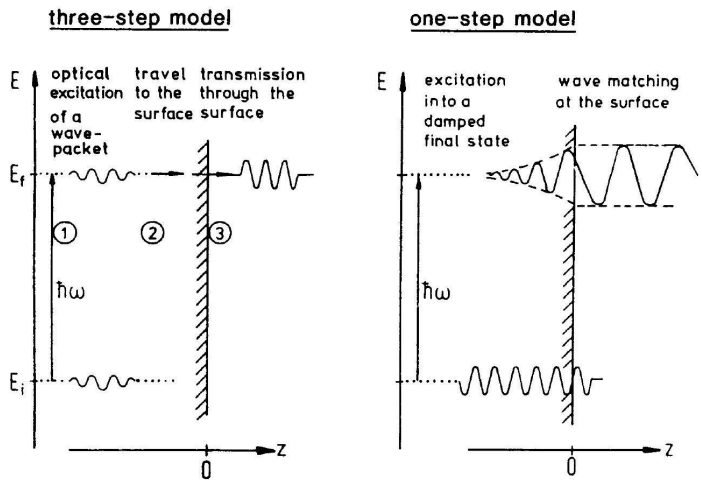

Figure 2.2: (left side) Schematic drawing of the three-step model dividing the photoemission process into three independent steps (taken from Ref. [15]): 1. optical excitation of the electron in the bulk; 2. travel of the photoelectron to the surface; 3. transition from the solid into vacuum thereby overcoming the surface barrier. (right side) Sketch of a one-step process. Within one single step the electron is excited into a damped final state which couples to a free electron wave in vacuum. In this model, all information referring to step two and three in the three-step model is included in the final wave function which couples to a free electron wave in vacuum.

describes photoemission in many cases by separating the effect into three independent steps: In a first step the electron is optically excited in the solid. Then it passes the material towards the surface and finally penetrates it to escape into vacuum. The left side of Fig. 2.2 gives an illustration of the three-step model; the particular steps will be discussed in the following.

Optical excitation of bulk interband transitions

In contrast to atomic systems the valence electronic states in a solid are described by energy bands. In the valence bands the electrons are delocalized, and the electronic states therefore depend on the wave vector $\vec{k}$ resulting in an energy dispersion $E(\vec{k})$ which is also called the *band structure* of a material. Furthermore, the common photon energies in ultraviolet photoelectron spectroscopy (UPS) and angle-resolved photoelectron spectroscopy (ARUPS) are $<$ 100 eV, and the momentum of the photon can thus be neglected. This means that all optical transitions from an initial state $|i\rangle$ to a final state $|f\rangle$ in a band-structure scheme are momentum conserving *direct* transitions ($\Delta\vec{k} = 0$). In a reduced scheme of the Brillouin zone these transitions proceed in a vertical manner, while in an extended scheme a reciprocal lattice vec-

tor has to be added [1]:

$$\vec{k}_f = \begin{cases} \vec{k}_i & \text{reduced zone scheme} \\ \vec{k}_i + \vec{G} & \text{extended zone scheme} \end{cases} \tag{2.4}$$

with $\vec{k}_f$ and $\vec{k}_i$ being the wave vectors of the final and initial electronic band states and $\vec{G}$ an adequate reciprocal lattice vector. Now the main goal consists in finding an expression for the photocurrent which is generated by direct transitions from initial states $\left|i, \vec{k}_i\right\rangle$ to final states $\left|f, \vec{k}_f\right\rangle$ inside the solid considering momentum as well as energy conservation. The description of transitions between initial and final states is thereby closely related to the indication of transition probabilities using Fermi's Golden Rule. Based on these ideas, the photocurrent can be written as

$$I \propto \left|\tilde{M}^1_{if}\right|^2 \delta(\vec{k}_i - \vec{k}_f + \vec{G})\, \delta(E_f - E_i - \hbar\omega) \tag{2.5}$$

with the transition matrix element

$$\tilde{M}^1_{if} = \langle \Psi_f \left| H_{\text{int}} \right| \Psi_i \rangle \,. \tag{2.6}$$

The tilde ' ˜ ' indicates that the momentum conservation is not implicitly contained in the matrix element, but is implemented explicitly by the first δ-function in (2.5). The initial and final states are described by the wave functions Ψ_i and Ψ_f which are eigenstates of the single electron Hamiltonian in the solid, $H_0 = \frac{p^2}{2m} + V(\vec{r})$. This operator defines the unperturbed system. In the three-step model Ψ_i and Ψ_f are Bloch states and connected by a direct interband transition (indicated by the superscript 1 in (2.6)). The perturbation operator H_{int} describes the interaction of an electron with the incident photon field. In the most general form we have

$$H_{\text{int}} = \frac{e}{2mc}(\vec{A}\cdot\vec{p} + \vec{p}\cdot\vec{A}) - e\phi + \frac{e^2}{2mc^2}\vec{A}\cdot\vec{A}\,; \tag{2.7}$$

$\vec{A}$ and ϕ are the vector and scalar potential of the photon field, respectively, and $\vec{p} = -i\hbar\vec{\nabla}$ is the electron momentum operator. For a monochromatic electromagnetic wave in vacuum we can use the gauge $\phi = 0$. Moreover, the fact that the two polarization vectors of the electromagnetic wave are perpendicular to its wave vector, $\vec{k}$, implies $\vec{\nabla}\cdot\vec{A} = i\vec{k}\cdot\vec{A} = 0$. Neglecting non-linear processes in the expression for H_{int} Eq. (2.7) is simplified to[2]

$$H_{\text{int}} = \frac{e}{mc}(\vec{A}\cdot\vec{p}). \tag{2.8}$$

[1] A reduced zone scheme only shows the first Brillouin zone and is formed by folding back the bands of the higher order Brillouin zones (extended scheme) into the first one. This is done by adding an adequate reciprocal lattice vector $\vec{G}$. Because of the periodicity of the lattice both descriptions are equivalent. In this work we will always refer to the reduced zone scheme.

[2] Assuming moderate fields where $\vec{A}\cdot\vec{p} >> \frac{e}{c}\vec{A}^2$ we can neglect the term $\vec{A}\cdot\vec{A}$. Furthermore, we have used $\vec{A}\cdot\vec{p} + \vec{p}\cdot\vec{A} = 2\vec{A}\cdot\vec{p} - i\hbar(\vec{\nabla}\cdot\vec{A}) = 2\vec{A}\cdot\vec{p}$.

Since for the energy range discussed here the wavelength of the incident photons is much larger than the interatomic distances $\vec{A}$ can be assumed as constant $\vec{A} = \vec{A}_0$. Furthermore, one derives the equivalence $\langle \Psi_f | \vec{A} \cdot \vec{p} | \Psi_i \rangle \propto \vec{A} \langle \Psi_f | [H_0, \vec{r}] | \Psi_i \rangle \propto \langle \Psi_f | \vec{A} \cdot \vec{r} | \Psi_i \rangle$, where we have again neglected second order contributions of $\vec{A}$. As mentioned, the momentum conservation (2.4) is taken into account by the first δ-function in Eq. (2.5). The second δ-function refers to the energy conservation in the solid. Note that the wave vector-dependence of the energies is not explicitly written out in (2.5).
In the energy range commonly used in valence band photoemission (5 - 40 eV) the inelastic mean free path of the excited electrons is comparatively short and damped inside the material [14]. This is considered by a complex wave vector normal to the sample surface,

$$k_\perp = k_\perp^1 + i k_\perp^2, \tag{2.9}$$

and leads to a 'smearing' of the momentum conservation law [15]. Eq. (2.5) is therewith changed to

$$I \propto \frac{\left| \tilde{M}_{if}^1 \right|^2}{(k_{i\perp}^1 - k_{f\perp}^1)^2 + (k_{f\perp}^2)^2} \, \delta\big(\vec{k}_i - \vec{k}_f + \vec{G}\big) \, \delta\big(E_f - E_i - \hbar\omega\big). \tag{2.10}$$

While the interaction of the excited photoelectron with the remaining system can be neglected (sudden approximation), we necessarily have to take into account the interaction between the remaining electrons of the system: Whenever a photohole is created in the excitation process, it does not belong to one special final state - as it was the case without electron-electron interaction - but can be found in any one of the possible s final states in a many electron system. In the following we indicate the initial as well as the final state wave functions in an appropriate manner, so that electron-electron interaction can be taken into account. Assuming a system of N electrons the initial state can be written as a product of the wave function of the photoelectron's initial state $\phi_i(\vec{k}_i)$ (replacing Ψ_i in Eq. (2.6)) and the wave function of the other $(N-1)$ electrons $\Psi_i(N-1)$,

$$\Psi_i(N) = \phi_i(\vec{k}_i) \Psi_i(N-1). \tag{2.11}$$

Analogously, the final state can be expressed as

$$\Psi_f(N) = \phi_{f,E_{\mathrm{kin}}}(\vec{k}_f) \cdot \sum_s \Psi_{f,s}(N-1), \tag{2.12}$$

where $\phi_{f,E_{\mathrm{kin}}}(\vec{k}_f)$ is the final state wave function of the photoexcited electron (replacing Ψ_f in Eq. (2.6)), and $\Psi_{f,s}(N-1)$ marks the wave functions of the s possible final states of the remaining electrons. Accordingly, the energy of the final states is $E_s(N-1)$, while the energy of the initial state $\Psi_i(N)$ is $E_0(N)$. With this (2.10) changes to

$$\begin{aligned} I \;\propto\; & \sum_{s,i} \left| \langle \tilde{\phi}_{f,\,E_{\mathrm{kin}}} | \, \vec{r} \, | \tilde{\phi}_i \rangle \right|^2 \left| \langle \tilde{\Psi}_{f,s}(N-1) | \tilde{\Psi}_i(N-1) \rangle \right|^2 \frac{1}{\left(k_{i\perp}^1 - k_{f\perp}^1\right)^2 + \left(k_{f\perp}^2\right)^2} \\ \times \;\; & \delta\big(\vec{k}_i - \vec{k}_f + \vec{G}\big) \, \delta\big(E_{\mathrm{kin}} + E_s(N-1) - E_0(N) - \hbar\omega\big). \end{aligned} \tag{2.13}$$

The tilde '~' has the same meaning as above. The function

$$A(\vec{k},E)=\sum_s\left|\left\langle\tilde{\Psi}_{f,s}(N-1)\middle|\tilde{\Psi}_i(N-1)\right\rangle\right|^2 \tag{2.14}$$

is called the *spectral function* and describes the overlap between the final states $\tilde{\Psi}_{f,s}(N-1)$ and the ground state $\tilde{\Psi}_i(N-1)$. It thus gives the probability for removing an electron from an electronic system in the ground state. Note that for non-interacting electrons Eq. (2.14) results in unity, since final and groundstate are the same. Electron-electron interaction can now explicitly be regarded by adding a so-called *self energy*

$$\Sigma(\vec{k},E)=\mathrm{Re}\,\Sigma+i\,\mathrm{Im}\,\Sigma \tag{2.15}$$

to the one-electron energy $E^0(\vec{k})$. Via the one-particle *Green's function* of the N-electron system [3]

$$G(\vec{k},E)=\frac{1}{E-E^0(\vec{k})-\Sigma(\vec{k},E)} \tag{2.16}$$

$A(\vec{k},E)$ results in

$$A(\vec{k},E)=\frac{1}{\pi}\frac{\mathrm{Im}\,\Sigma}{\left(E-E^0(\vec{k})-\mathrm{Re}\,\Sigma\right)^2+\left(\mathrm{Im}\,\Sigma\right)^2}. \tag{2.17}$$

Note that the poles of (2.16), $E^1(\vec{k})-E^0(\vec{k})-\Sigma\big(\vec{k},E^1(\vec{k})\big)=0$, yield the energetic spectrum of the interacting system (with the assumption $\mathrm{Re}\,\Sigma\gg\mathrm{Im}\,\Sigma$). E^1 is the (renormalized) electron energy in the interacting system. It differs from E^0, since the electrons are surrounded by clouds of virtual excitations, both moving coherently with each other. These combined particles are called *quasiparticles*.
Now we can formulate the complete expression for the photocurrent in a crystalline solid which is evoked by an optical excitation:

$$\begin{aligned}I(E,\hbar\omega)\;\propto\;&\sum_{i,f}\frac{\mathrm{Im}\,\Sigma(\vec{k}_i)}{\left(E-E^0(\vec{k}_i)-\mathrm{Re}\,\Sigma(\vec{k}_i)\right)^2+\left(\mathrm{Im}\,\Sigma(\vec{k}_i)\right)^2}\cdot\frac{\left|\tilde{M}^1_{i,f}\right|^2}{\left(k^1_{i\perp}-k^1_{f\perp}\right)^2+\left(k^2_{f\perp}\right)^2}\\&\times\delta\big(\vec{k}_i-\vec{k}_f+\vec{G}\big)\,\delta\big(E^1(\vec{k}_f)-E^1(\vec{k}_i)-\hbar\omega\big)\cdot f(E,T),\end{aligned} \tag{2.18}$$

where $f(E,T)$ is the Fermi distribution, and we have explicitly indicated the dependence of the energies on the wave vectors. The Fermi distribution assures that in the sum over all initial states only the occupied ones contribute. Furthermore, $\tilde{M}^1_{i,f}$ represents the matrix element introduced in Eq. (2.6) for the single photoelectron.

[3] The spectral function is directly connected to the one-particle Green's function $G(\vec{r}_1,\vec{r}_2,t)$ of a N-electron system which gives the probability for a propagation of an electron from $(\vec{r}_1,t=0)$ to $(\vec{r}_2,t>0)$. Fourier-transformed to the reciprocal space, $G(\vec{k}_1,\vec{k}_2,E)$ describes the probability for an electron scattering from a state $\vec{k}_1$ to a state $\vec{k}_2$ under an energy transfer E. If we consider only the diagonal elements of the Green's function we finally obtain $G(\vec{k},E)$ which yields the spectral function by $A(\vec{k},E)=\frac{1}{\pi}\left|\mathrm{Im}\,G(\vec{k},E)\right|$. Determining $G(\vec{k},E)$ under consideration of the self-energy therefore directly delivers $A(\vec{k},E)$.

Transport to the surface

In a second step the excited photoelectrons travel to the solid surface. During transport they undergo inelastic scattering processes that reduce the number of electrons escaping into vacuum. The most dominant scattering mechanism is electron-electron interaction. In the three-step model scattering processes are captured by the electron's inelastic mean free path

$$\lambda(E,k) = \tau v_{\mathrm{g}} = \frac{\tau}{\hbar}\frac{dE}{dk}, \tag{2.19}$$

where v_{g} is the group velocity in the final state and $\frac{1}{\tau}$ is the scattering frequency which is assumed to be isotropic and only dependent on E. Moreover, the transport is characterized by the fraction of all photoelectrons which are created within one mean free path from the surface. This is described by a coefficient

$$d(E,k) \approx \frac{\alpha\,\lambda}{1+\alpha\,\lambda}, \tag{2.20}$$

where α marks the absorption coefficient for light. For (2.20) two extrema are possible: $\alpha\,\lambda \gg 1 \Rightarrow d(E,k) \to 1$. This means that all photoexcited electrons reach the surface without being involved in an inelastic scattering process. For $\alpha\,\lambda \ll 1 \Rightarrow d(E,k) \to \alpha\,\lambda$, the electron's mean free path is much smaller than the penetration depth of the light α^{-1}, and only the fraction $\alpha\,\lambda$ reaches the surface without inelastic scattering.

Transmission through the surface and escape into vacuum

The third step describes the transition of the photoelectrons from the solid to vacuum, for which they have to overcome the surface potential barrier: Inside the material the electrons are expected to behave like free electrons moving in a potential of depth $E_{\mathrm{V}} - E_0$, where E_{V} is the vacuum energy and $E_0(<0)$ is the minimum energy of the lowest valence band. For escape into vacuum the component of the electrons' kinetic energy perpendicular to the surface must therefore be larger than $E_{\mathrm{V}} - E_0$; otherwise the electron is reflected back into the material,

$$\frac{\hbar^2}{2m}\vec{k}_{f\perp}^{\,2} \geq E_{\mathrm{V}} - E_0. \tag{2.21}$$

This implies that a minimum value of the normal component $|\vec{k}_{f\perp}|$ of the electron wave vector in the final state is needed for transmission, $|\vec{k}_{f\perp}|_{\min} = \frac{\sqrt{2m}}{\hbar}(E_{\mathrm{V}} - E_0)^{1/2}$. Eq. (2.21) only refers to the perpendicular component of the electron momentum. Due to the two-dimensional translation invariance of the surface the parallel momentum is conserved at the transition:

$$\vec{k}_{f\parallel}(\mathrm{int}) = \vec{k}_{f\parallel}(\mathrm{ext}) = \vec{p}_{\parallel}/\hbar. \tag{2.22}$$

The situation at the solid vacuum interface is sketched in Fig. 2.3 which illustrates that a transition of electrons from solid to vacuum is equivalent to the diffraction of light at the interface between an optically dense and an optically light material.

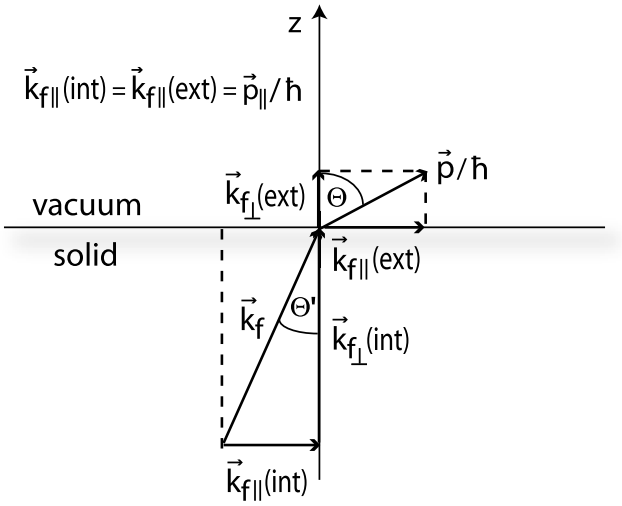

Figure 2.3: Relation between wave vector and momentum components of the electron at the transition between solid and vacuum. While the parallel component $\vec{k}_{f\parallel}$ is conserved during the transition, the perpendicular component $\vec{k}_{f\perp}$ is changed. The situation reflects Snell's diffraction law for the case of electron trajectories (according to Ref. [15]).

With the help of Fig. 2.3 one can therefore derive a diffraction law for electron trajectories in strong analogy to Snell's diffraction law in optics. Using the conservation law for the parallel component of the momentum $\left(\vec{p}_{\parallel}(\mathrm{int}) = \vec{p}_{\parallel}(\mathrm{ext})\right)$ one finds:

$$\begin{aligned} \left|\vec{p}_{\parallel}(\mathrm{int})\right| &= \left|\vec{k}_{f\parallel}(\mathrm{int})\hbar\right| = \left|\sin\theta'\vec{k}_f(\mathrm{int})\hbar\right| = \sin\theta'\Big(2mE_{\mathrm{kin}}(\mathrm{int})\Big)^{\frac{1}{2}} \\ &= \sin\theta'\Big(2m(E_f - E_0)\Big)^{\frac{1}{2}} = \left|\vec{p}_{\parallel}(\mathrm{ext})\right| = \left|\sin\theta\,\vec{p}\right| = \sin\theta\Big(2mE_{\mathrm{kin}}(\mathrm{ext})\Big)^{\frac{1}{2}}, \end{aligned} \tag{2.23}$$

where θ' and θ are the diffraction angles inside and outside the material with respect to the surface normal. Eq. (2.23) shows that θ is always larger than θ' and ranges from $0°$ to $90°$. At the limiting angle of $\theta = 90°$ the electrons would be emitted parallel to the sample surface, for larger angles they are totally reflected into the material. Apparently, $\theta = 90°$ also marks the limit for the angle distribution inside the material. For $\sin\theta = 1$ the maximum angle inside the solid is given by

$$\sin\theta'_{\mathrm{max}} = \sqrt{\frac{E_{\mathrm{kin}}(\mathrm{ext})}{E_{\mathrm{kin}}(\mathrm{int})}} = \sqrt{\frac{E_{\mathrm{kin}}}{E_f - E_0}} = \sqrt{\frac{h\nu - \Phi}{h\nu - \Phi + eV_0}}, \tag{2.24}$$

where $E_{\mathrm{V}} - E_0 = eV_0$ is the crystal potential and $E_f - E_{\mathrm{V}} = h\nu - \Phi$ assuming $E_{\mathrm{B}} = 0$. Reaching θ'_{max} is equivalent to receiving the minimum value of $k_{f\perp}$ given by (2.21). The

angles $\theta'_{\min} \leq \theta' \leq \theta'_{\max}$ span the so-called *inner escape cone* which is especially important in the regime of threshold photoemission: For a photon energy of $h\nu = 4.65\,\text{eV}$ and an assumed work-function value of $\Phi = 4.5\,\text{eV}$ the maximum kinetic energy of the electrons in vacuum reaches $E_{\text{kin}} = 0.15\,\text{eV}$. With a typical inner potential of $eV_0 = 15\,\text{eV}$, $\theta'_{\max}$ yields $5.7°$. This example points out that for excitations in the vicinity of the threshold the escape cone effect limits possible transitions close to the normal emission direction. The opening of the cone with increasing E_{kin}, however, admits small values of $k_{\|}$.
Considering the upper energy and momentum conditions (2.21) and (2.22) respectively, the transmission of electrons from the solid to vacuum is finally encoded in a transmission factor: In the three-step model the wave function of the final state is described by a Bloch wave, consisting of a superposition of plane waves with the reciprocal lattice vectors $\vec{G}$,

$$\Psi_f(\vec{k}) = \sum_{\vec{G}} u_f(\vec{k}, \vec{G}) e^{i(\vec{k}+\vec{G})\cdot\vec{r}}. \tag{2.25}$$

The escape of a photoelectron is given by a coupling of a plane wave component to a free propagating wave in vacuum. Components of energy $E_f(\vec{k})$ with the same value of $(\vec{k}_{\|} + \vec{G}_{\|})$ escape in the same direction from the material and must be treated as a coherent superposition. The total transmission factor $\left|T(E_f, \vec{k}_{f\|})\right|^2$ for such a superposition can be expressed by the sum of the transmission factor for each plane wave resulting in

$$\left|T(E_f, \vec{k}_{f\|})\right|^2 = \left|t(E_f, \vec{k}_{f\|})\right|^2 \Big| \sum_{(k+G)_\perp > 0} u_f(\vec{G}, \vec{k}) \Big|^2. \tag{2.26}$$

The sum is only performed over components traveling towards the surface. For a detailed expression of $\left|t(E_f, \vec{k}_{f\|})\right|^2$ we refer to Ref. [15]. Note that in the case of significant spin-orbit interaction the transmission step gives rise to an electron spin polarization and to 'dichroism-like' intensity effects if the electrons inside the solid are spin-polarized. In the case of total yield measurements which are exclusively performed for this work these effects are absent due to an averaging over all emission angles [17, 18].
Having analyzed all three steps we can state a final expression for the photocurrent. To simplify matter we neglect electron-electron interaction in the first step as well as the damped mean free path of the excited electrons. The summation is carried out only over occupied initial states. For the second step the transport coefficient $d(E, k)$ and for the third step the total transmission factor $\left|T(E_f, \vec{k}_{f\|})\right|^2$ additionally have to be taken into account. Furthermore, we have to care about the conservation of the parallel component of the electron momentum as well as for energy conservation during transition from the solid into vacuum. Following Ref. [15] this finally yields

$$\begin{aligned} I(E, \vec{k}_{f\|}, \hbar\omega) \;\propto\; & \sum_{f,i} \left|\tilde{M}^1_{fi}(\vec{k}_i, \vec{k}_f)\right|^2 d(E_f, \vec{k}_f) \left|T(E_f, \vec{k}_{f\|})\right|^2 \\ & \times\; \delta\big(E_f(\vec{k}_f) - E_i(\vec{k}_i) - \hbar\omega\big)\, \delta\big(E - E_f(\vec{k}_f) + \Phi\big) \\ & \times\; \delta\big(\vec{k}_i + \vec{G} - \vec{k}_f\big)\, \delta\Big(\vec{k}_{f\|} - \frac{\vec{p}_{\|}(\theta, \phi)}{\hbar}\Big). \end{aligned} \tag{2.27}$$

The second δ-function thereby describes the energy condition for the transition from material into vacuum, meaning that only photoelectrons with kinetic energies of $E_f - E_\mathrm{V}$ outside the material can be detected. The last one regards the conservation of the parallel component of the electron momentum. The indication of the electron's emission direction (θ, ϕ) should reveal the nature of the experiment as an angle-resolved technique.
Although the three-step model delivers a comprehensive description of photoemission and often serves as a useful approximation for the analysis of photoemission spectra, it is not completely correct. Particularly the effect of the surface on the photoemission process is not sufficiently taken into account: In the three-step model the final state is always assumed to be Bloch-like. However, final states which are located close to the surface cannot be described by propagating Bloch waves and are thus ruled out. Furthermore, the surface generally reveals an electronic structure which is different from that of the bulk (due to reduced coordinations) and therefore has a different effect on the photocurrent. This is also not taken into account. Another problem arises with respect to Eq. (2.8): $\vec{\nabla} \cdot \vec{A} = 0$ is valid for the bulk but does not hold for the surface. At the surface $\vec{\nabla} \cdot \vec{A}$ is expected to change and cannot be neglected as recent experiments have shown [19, 20, 21, 22]. Also the description of the escape of photoelectrons into vacuum by a simple transmission factor might be too naive. From an experimental point of view, it is often argued that the three-step model cannot explain the appearance of the Fermi edge in UPS-investigations for most of the metals. In these systems the Fermi edge is observed, although direct interband transitions between two Bloch states are not possible in the band-structure scheme around the Fermi level. In order to handle these problems and to give a more correct description, i. e. by properly taking into account the influence of the sample surface, the one-step model has been developed.

2.1.3 The one-step model

The one-step model strongly alludes to the theory of low energy electron diffraction (LEED). In LEED a monochromatic beam of low-energy electrons ($E \approx 50 - 150\,\mathrm{eV}$, velocity $-\vec{v}$) impinges a surface and splits into a beam penetrating the material and another beam which is specularly reflected with velocity $\vec{v}$. If we neglect the reflected beam and invert the directions of the two remaining beams, we arrive at the situation of a photoemission experiment keeping in mind that a photon is needed for initialization of the process. Due to the apparent closeness to the LEED theory this concept is called *inverse LEED theory of photoemission*. In analogy to the three-step model one can derive an expression for the photocurrent

$$I\left(E, \hbar\omega, \vec{v}/\left|\vec{v}\right|\right) \propto \vec{v} \cdot \sum_{\text{occupied},i} \left|\left\langle \Psi^\mathrm{L}(\vec{r}, E, \vec{k}_f) \middle| A_0\, \vec{p} \middle| \Psi_i(\vec{r}, \vec{k}) \right\rangle\right|^2 \delta(E_f - E_i - \hbar\omega). \qquad (2.28)$$

where $\vec{v}/\left|\vec{v}\right|$ is the unit-vector along the direction of the electron beam and $\vec{k} = x\hat{e}_x + y\hat{e}_y + z\hat{e}_z$ [4]. We have again neglected electron-electron interaction and the sum is explicitly carried

[4] Here, we have used $H_\mathrm{int} = \vec{A_0} \cdot \vec{p} = A_0\, \hat{e} \cdot \vec{p} \propto A_0\, \vec{v} \cdot \vec{p}$. In the first step we have used the dipole approximation; $\hat{e}$ is the unit-vector along the direction of the electric field and points in the same direction as $\vec{v}$.

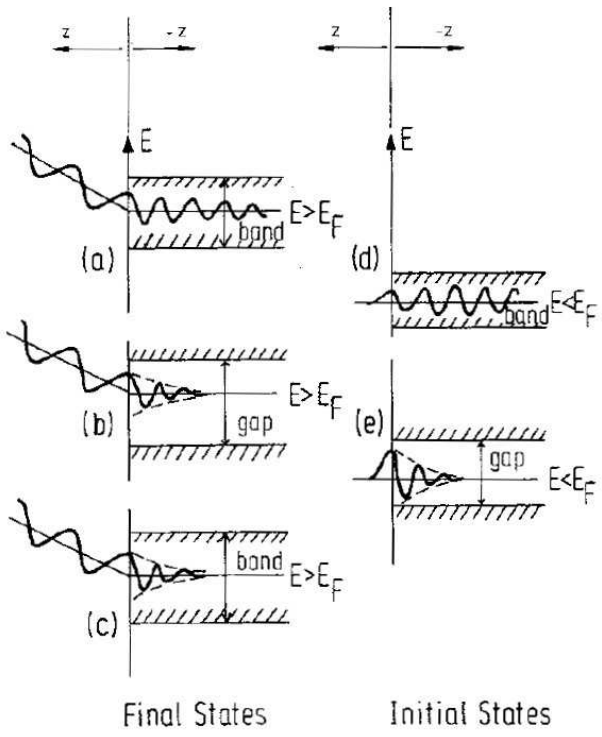

Figure 2.4: Final and initial wave functions in the one-step model (taken from Ref. [15]). Final states (left side) (a) weakly damped Bloch wave; (b) evanescent state in a band gap; (c) evanescent state in a band. All final states couple to a free electron wave in vacuum. Initial states (right side) (d) bulk Bloch state; (e) surface state in a gap.

out over occupied initial states. The final state Ψ^{L} is a time-reversed LEED-state. It always contains a wave which freely propagates outside the material and therefore provides the coupling to vacuum. This already indicates that the third step (and also the second) arising in the three-step model do not have to be added artificially, but the whole information is incorporated in Ψ^{L} making the process a real one step mechanism. The right side of Fig. 2.2 shows a sketch of the one-step process. Generally, one distinguishes three different forms of Ψ^{L} which are depicted on the left side of Fig. 2.4. For the initial state there are two possibilities shown on the right side of Fig. 2.4.

As final state a Bloch wave with only small damping can occur in the solid (a). Also an evanescent state in a band gap (b) or in a band (c) of the material are possible. Evanescent states are exponentially damped final states which can appear in bands as well as in band gaps. The large damping is equivalent to an enlarged imaginary part of the wave vector and is mainly attributed to inelastic scattering processes. Evanescent states have their maximum amplitude right at the surface and drop exponentially towards the bulk [23]. With respect to band states

the term 'evanescent state' can synonymously be used for a 'strongly damped Bloch state'. Since the propagating as well as the highly damped final states are treated on an equal footing Ψ^{L} consists of a sum of both,

$$\Psi^{\mathrm{L}} \propto \exp\left(i\vec{k}_{f\parallel}\cdot\vec{\rho}\right)\sum_m t_m \exp\left(ik_{\perp m}z\right) u_m(\vec{r},\vec{k}_{f\parallel},E), \tag{2.29}$$

where $\vec{\rho} = x\hat{e}_x + y\hat{e}_y$ is a vector in the $(x-y)$-surface plane and t_m is the transmission coefficient. The waves are described by two-dimensional Bloch functions. In analogy to Eq. (2.9) we decompose

$$k_{\perp m} = k^1_{\perp m} + i\,k^2_{\perp m}. \tag{2.30}$$

In the case of $k^2_{\perp m} = 0$ the final state is a propagating wave. Damping is switched on by finite values of $k^2_{\perp m}$. The magnitude of these values separates Bloch waves with small damping from evanescent waves with enlarged damping. For the initial state a Bloch wave as well as a surface state in a band gap is possible, and one can write

$$\Psi_i = \exp\left(i\vec{k}_{i\parallel}\cdot\vec{\rho}\right)\sum_n C_n \exp\left(ik_{\perp n}z\right) v_n(\vec{r},\vec{k}_{i\parallel},E_i), \tag{2.31}$$

with $k_{\perp n} = k^1_{\perp n} + i\,k^2_{\perp n}$.
Note that by setting $k^2_{\perp n} = 0$ and by considering only small values of $k^2_{\perp m}$ one refers to a propagating initial and a weakly damped final Bloch function which reflects the situation in the three-step model. Furthermore, one can separate the matrix element $M_{f,i}$ into a bulk and a surface part. Ignoring the surface term leads to an expression for the photocurrent representing the result of the three-step model. This means that the three-step model can be recovered from the one-step formalism. For details see Ref. [23, 24].
Finally, we want to comment on the usefulness of both models for the photoemission experiments presented in this work. We have mentioned that the one-step formalism delivers a correct description of the photoemission process by explicitly taking into account the surface of the material. Thereby, emission into evanescent states often taking place due to the lack of a real final or intermediate state, is fully described. For reasons we will discuss below our measurements can only be interpreted by direct interband transitions between initial Bloch states and final weakly damped Bloch states. Excitations to evanescent final states are excluded. Moreover, the use of photon energies in the range of the sample work function (threshold photoemission) reveals an enhanced mean free path of the excited electrons. This means that in contrast to conventional valence band photoemission, where photon energies ranging from $\sim$ 20-40 eV trigger very surface sensitive excitations (c. f. UPS), the electrons in our experiment can be excited from the bulk of the material and excitations to evanescent states which are located close to the surface will only play a minor role. For these reasons it is more convenient to think of the present photoemission experiments in the light of the three-step model.

2.2 Magnetic circular dichroism in valence band photoemission

Having illustrated the basic theoretical concepts of valence band photoemission the following paragraph introduces the physical phenomenon of *magnetic circular dichroism* (MCD) in valence band photoemission, to which this work is primarily devoted. As already suggested by the term itself MCD reveals a difference for the absorption of left-circularly (σ^+) and right-circularly (σ^-) polarized light in magnetic materials. This means that due to the different nature of the two circular polarizations the absorption of σ^+ and σ^-- radiation differs from each other in a material magnetized along a certain direction. This difference is sometimes expressed 'macroscopically' using the frequency-dependent absorption coefficients of the material for the two circular polarizations [25],

$$\Delta\mu(\omega) = \mu^+(\omega) - \mu^-(\omega). \tag{2.32}$$

The 'microscopic' reason for MCD is traced back to an interplay between the spin-orbit coupling (SOC), which leads to a lifting of degeneracies in the electronic states and the exchange interaction in ferromagnetic materials, which results in a spin-polarization of electronic states [26]. Thereby, only the simultaneous appearance of both effects allows for the detection of MCD. This will be discussed in detail in Ch. 2.2.2. Since the electronic structure is strongly influenced by SOC and exchange-splitting electrons excited by a photoemission process also carry information about SOC- and exchange-splitting-induced effects. Especially photoelectrons of a magnetized material excited by left- and right-circularly polarized light should yield complete information on MCD. In analogy to Eq. (2.32) one can therefore measure an intensity difference $I^{\sigma^+} - I^{\sigma^-}$ of the photoelectrons for the two circular polarizations at fixed magnetization. Normalizing leads to the so-called *MCD asymmetry* which is often used for the interpretation of MCD measurements,

$$A = \frac{I^{\sigma^+} - I^{\sigma^-}}{I^{\sigma^+} + I^{\sigma^-}}. \tag{2.33}$$

A detailed derivation of the MCD asymmetry for the case of a (111) surface will be given in Ch. 2.2.2. The circumstance that MCD originates from a simultaneous appearance of spin-orbit coupling and exchange-splitting can only be explained by knowing which initial and final states in a band-structure scheme might participate in the photoemission process. Which transitions finally take place depends on the symmetry of the electronic states and the dipole operator [27]. Both decide about the existence of the transition matrix elements via *dipole selection rules* [28, 29] to which we will refer in Ch. 2.2.1.

Moreover the geometry of the photoemission experiment is of great importance, since it determines the symmetry characters of electronic states involved in the photoexcitation and therefore implicitly decides about the occurrence of MCD and the information contained in the measured spectra. Experimental geometries are classified by the arrangement of the photon wave vector $\vec{k}$, the photon helicity $\vec{\Lambda}_\sigma$, the magnetization direction $\vec{M}$ and the direction of electron emission. In this context, MCD only exists, if the two geometries defined by $(\vec{k}, \vec{\Lambda}_\sigma, \vec{M})$

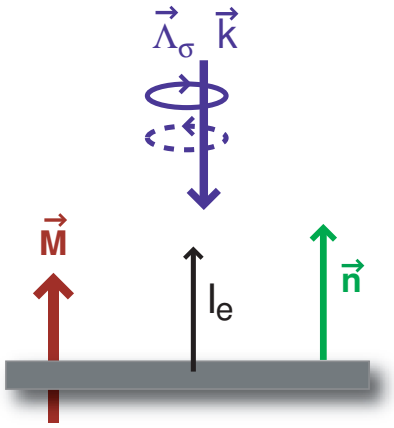

Figure 2.5: Totally symmetric experimental setup using circularly polarized light (according to Ref. [26]). The magnetization $\vec{M}$, the helicity $\vec{\Lambda}_\sigma$ and the wave vector $\vec{k}$ of the incident light as well as the direction of electron emission are all aligned parallel (antiparallel) to the surface normal $\vec{n}$.

and $(\vec{k}, \vec{\Lambda}_\sigma, -\vec{M})$ at the same direction of electron emission are inequivalent with respect to the point group of the material [5]. This means that no symmetry operation of the point group can transfer one geometry into the other which is especially true for totally symmetric setups [26]. Furthermore, only for totally symmetric arrangements a maximum number of different relativistic symmetry characters is attributed to the electronic bands. With the help of relativistic dipole selection rules this enables a direct relation between electronic excitations in the band structure and the observed dichroism. Single features in the dichroic spectra can therefore be directly attributed to the symmetry character of the relativistic band structure [6]. In setups of extreme symmetry $\vec{k}$, $\vec{\Lambda}_\sigma$ and $\vec{M}$ are aligned parallel (antiparallel) to each other and perpendicular to the sample plane. The magnetization easy axis points out of the sample plane. Also electron emission takes place in the direction of the surface normal. Fig. 2.5 shows an experimental setup of 'total' symmetry using circularly polarized light. A consequence of the totally symmetric setup is the fact that the dichroism obtained by changing the light helicity at fixed magnetization is equivalent to the one obtained by changing the magnetization direction and keeping instead the light helicity fixed; both cases deliver the same result. Simultaneously switching $\vec{\Lambda}_\sigma$ and $\vec{M}$ would therefore yield zero dichroism. The reason for this so-called *exchange dichroism* is due to the axial nature of both vectors $\vec{M}$ and $\vec{\Lambda}_\sigma$. For experimental setups with lower geometry this equivalence is no longer fulfilled [26].
Finally, we want to point out that MCD is often numbered among the magneto-optical phenomena [25, 9] as those also result from an interplay between spin-orbit coupling and ex-

[5] The point group **G** contains all symmetry operations which leave a point in the unit cell of the crystal lattice invariant.

change interaction. We will come back to that in Ch. 2.2.3.

2.2.1 Irreducible representations of electronic states and dipole selection rules

All electronic states can be classified by so-called *irreducible representations* of the crystal's symmetry group: The symmetry group is the point group **G** of the material which is described by a set of irreducible single-group representations which on their part also classify the electronic states. This classification is important because it enables a distinction of electronic bands along the high symmetry directions. The single-group representations only refer to the spatial symmetries in a system and can only be used in the non-relativistic limit. They are shown in the left column of Table 2.1 for the [111] direction of a cubic crystal (since in this work the [111] direction is mostly investigated we refer only to this high symmetry direction).

[111]		
Λ^1	Λ_6^1	
Λ^2	Λ_6^2	
$\Lambda_\diamond^3$	$\Lambda_{4,5}^3$	$\Lambda_{4,5}^3 \xrightarrow{\lvert\uparrow\rangle} \Lambda_6^1$
	Λ_6^3	$\Lambda_6^3 \xrightarrow{\lvert\downarrow\rangle} \Lambda_6^1$

Table 2.1: (left column) Non-relativistic single-group representations. (center column) Relativistic double-group representations for the [111] direction of a cubic crystal (according to Ref. [26]). (right column) Corresponding relativistic dipole selection rules for a totally symmetric setup and right circularly polarized light. For left circularly polarized light $|\uparrow\rangle$ and $|\downarrow\rangle$ have to be interchanged. Superscripts denote the spatial symmetry, subscripts the double-group symmetry.

The superscript indicates the spatial symmetry. Also note that Λ^3 is specially marked to indicate its twofold degeneracy in the energy eigenvalues. Single-group representations are thus used to distinguish electronic states in the band structure of non-magnetic materials in the non-relativistic limit, i. e. relativistic effects like spin-orbit coupling are neglected. In a non-magnetic material (with spatial inversion symmetry) all states are doubly-degenerate with

respect to the spin. This is called *Kramers degeneracy* meaning $E(\vec{k},\uparrow) = E(\vec{k},\downarrow)$ [26]. In contrast, for ferromagnets the exchange splitting leads to a net magnetization in the material. Since the system is no longer invariant under time reversal the total symmetry is lowered which is directly reflected by a lifting of the Kramers degeneracy, $E(\vec{k},\uparrow) \neq E(\vec{k},\downarrow)$. Each band is then still classified by the non-relativistic single-group representation of Table 2.1 (left column), but it is now also classified according to its spin character. Consequently a band with Λ^1-symmetry in the non-magnetic case is split into two independent bands described as $\Lambda^{1\downarrow}$ and $\Lambda^{1\uparrow}$ in ferromagnets, and an excitation channel exists for each spin character [26]. Often the representations are also indicated by Λ^1+ and Λ^1-. The plus/minus signs thereby mark the respective behavior under time reversal.
Additional inclusion of spin-orbit coupling requires a relativistic treatment of the electronic system resulting in a description by relativistic irreducible double-group representations which are shown in the middle column of Table 2.1. Thereby the double group is created by the product of the single group with the rotational group in spin space, $\mathbf{DG} = \mathbf{G} \otimes \mathbf{SU_2}$ [26]. In Table 2.1 the double-group symmetry is indicated as a subscript. We notice that under the influence of spin-orbit coupling the doubly-degenerate single-group representation Λ^3 splits into $\Lambda^3_{4,5}$ and Λ^3_6; its degeneracy is lifted. SOC therefore also reduces the symmetry of the system. $\Lambda_{4,5}$ marks the two single-valued representations Λ_4 and Λ_5, degenerated by time reversal-symmetry, while Λ_6 is again two-dimensional [26]. Note that after taking into account spin-orbit coupling the spatial symmetry as well as the spin are no longer good quantum numbers. In a relativistic treatment a band does therefore no longer carry one spin character and one spatial symmetry. In contrast, it might consist of a combination of different single group representations and both spin characters. That is also the reason why in many fully-relativistic band-structure calculations (c. f. Ch. 4.3) the bands are merely indicated by numbers beginning with the bottommost valence band. Despite the occurrence of different spatial symmetry characters for one band the spatial symmetry of the non-relativistic case is retained as a superscript, since even in a relativistic treatment it mostly remains predominant within the associated band.
Another peculiarity of the relativistic treatment arises, when bands of the same double-group symmetry (but different single-group symmetry) cross each other. Since these crossings are forbidden, so called *hybridization gaps* are formed at the corresponding points of the band structure. As a consequence, in these regions the spatial symmetry of the bands gets continuously changed. Recent studies have been devoted to the investigation of such avoided crossings (e. g. [30]); for the present work they are of minor importance.
Beside the relativistic double-group representations the polarization of the incident photon beam (i. e. the orientation of the vector field $\vec{A}$) is important since the orientation of $\vec{A}$ also determines which initial states are excited [27]. In turn, the excitation of particular transitions demands the use of the corresponding polarization orientation. For the application of relativistic dipole selection rules the use of circularly polarized light in a totally symmetric setup is required [26]. The right column of Table 2.1 finally gives the relativistic dipole selection rules for the mentioned conditions. We notice that all photoelectrons are excited to Λ^1- final states, because the final state in the case of normal electron emission along a high-symmetry direction

is required to be totally symmetric with respect to all symmetry operations along the surface normal. This is only fulfilled for final states with Λ^1-spatial symmetry character [15, 31].
Finally, Borstel et al. [29, 32] showed that the use of relativistic selection rules is necessary even for bands which are not split by spin-orbit coupling, since SOC affects the whole system. In an exact treatment the application of non-relativistic selection rules therefore fails even if SOC is small. Note that the relativistic dipole selection rules of Table 2.1 in fact decide, whether a transition from an initial state into a final state takes place. The quantitative contribution of a transition to the photoemission spectrum is, however, determined by the magnitude of the momentum matrix element $\langle f\,|\vec{p}|\,i\rangle$ to which we refer below. Finally, also note that all considerations presented above are based on the assumption of inversion symmetry which holds for the bulk. For the surface inversion symmetry is broken which must additionally be taken into account.

2.2.2 Magnetic circular dichroism in valence band photoemission for the case of a (111) surface

Having introduced the double-group representations of electronic states and the relativistic dipole selection rules the dipole transition matrix elements in valence band photoemission can now be evaluated. From these, expressions for the spin-averaged intensity and the MCD asymmetry can be derived which hold for all crystal surfaces in a totally symmetric setup. Due to the complexity of the matter we can give here only a crude description. More detailed derivations can be found in [33], to which we mainly refer in the following. The results, however, will show how MCD is explicitly calculated via dipole transition matrix elements and how it is associated with the contributions of both- spin-orbit coupling and exchange interaction- in the intensity spectra and the derived asymmetry.
Assuming a Pauli-like Hamiltonian [6] which retains spin-orbit coupling leads to a Golden Rule (-like) expression for the spin density matrix of the photocurrent [34]. Its elements are given by:

$$\rho_{ss'}(E_f) = \sum_{i,s''} \left\langle f_s \middle| \vec{E}\cdot\vec{r} \middle| i_{s''} \right\rangle \left\langle i_{s''} \middle| \vec{E}\cdot\vec{r} \middle| f_{s'} \right\rangle \delta(E_f - \hbar\omega - E_{i_{s''}}). \tag{2.34}$$

The initial and final states $|i_s\rangle$ and $|f_s\rangle$ are two-component eigenfunctions of the Pauli-like Hamiltonian, with $s = \pm$. While the final states $|f_+\rangle$ and $|f_-\rangle$ both have the energy E_f, the energy of the initial state must be equal to $E_f - \hbar\omega$ in order to contribute to the spectrum (which is implemented by the δ-function). $\vec{E}\cdot\vec{r}$ is the dipole operator, whereby we assume the electric field $\vec{E}$ to be spatially constant due to dipole approximation [7]. In this sense the

[6] The Dirac equation describes the motion of an electron in an electromagnetic field, thereby adequately treating the spin of the electron. In the non-relativistic limit the Dirac equation can be approximated by the more tractable formalism of the Pauli equation. Therein only two-component spinors (instead of the four-component spinors in the Dirac equation) are the eigenfunctions of the Pauli Hamiltonian.

[7] Note that $\vec{E}\cdot\vec{r}$ can be written instead of $\vec{A}\cdot\vec{r}$, since $\vec{E} = i\omega\vec{A}$ for monochromatic electromagnetic waves in vacuum.

spin-density matrix of the photocurrent is constructed from the known dipole transition matrix elements

$$W_{ss'}(E_f) = \left\langle f_s \middle| \vec{E} \cdot \vec{r} \middle| i_{s'} \right\rangle, \qquad s, s' = \pm, \tag{2.35}$$

where the initial and final states take the form

$$|\Psi_s\rangle = \sum_n \alpha_n^s \, |R_n^s\rangle \, |g_n^s\rangle \,, \qquad s = \pm. \tag{2.36}$$

The functions $|g_n^s\rangle$ are basis functions consisting of an angular term and a Pauli spinor, and $|R_n^s\rangle$ are normalized radial functions [33]. If the final states are time-reversed LEED states (one-step formalism), the coefficients α_n^s are complex. For the dipole operator one can further write

$$\begin{aligned} \vec{E} \cdot \vec{r} \;\; &= \;\; \sqrt{\frac{4\pi}{3}} r \left[E_{\parallel} \Big(- \sin\vartheta Y_1^0 + \cos\vartheta \frac{1}{\sqrt{2}} \big(\exp(i\varphi) Y_1^{-1} - \exp(-i\varphi) Y_1^1 \big) \Big) \right. \\ &+ \;\; \left. E_{\perp} \frac{i}{\sqrt{2}} \Big(\exp(i\varphi) Y_1^{-1} + \exp(-i\varphi) Y_1^1 \Big) \right], \end{aligned} \tag{2.37}$$

where Y_l^m are spherical harmonics and φ and ϑ are the polar and azimuthal angles describing the direction of light incidence [33]. Note that for left/right-circularly polarized light one has $(E_{\parallel}, E_{\perp}) = E(\pm i, 1)/\sqrt{2}$. With Eq. (2.36) and (2.37) the dipole matrix elements $W_{ss'}$ can finally be evaluated. Expressing the spin-density matrix for the photocurrent in terms of the $W_{ss'}$ yields

$$\rho(E_f) = \begin{pmatrix} |W_{++}|^2 + |W_{+-}|^2 & W_{++}W_{-+}^* + W_{+-}W_{--}^* \\ W_{++}^* W_{-+} + W_{+-}^* W_{--} & |W_{-+}|^2 + |W_{--}|^2 \end{pmatrix}. \tag{2.38}$$

From this expression one now obtains the photoelectron intensity $I(\varphi, \vartheta)$ measured in a non-spin-resolved photoemission experiment by

$$I(\varphi, \vartheta) = Tr\big(\rho\big). \tag{2.39}$$

The (non-normalized) MCD asymmetry then follows to

$$A = I(\varphi, \vartheta, \vec{M}) - I(\varphi, \vartheta, -\vec{M}) \tag{2.40}$$

using circularly polarized light. Eq. (2.39) and (2.40) are the major results of this section. They demonstrate how the intensity and the MCD asymmetry of a valence band photoemission experiment are related to dipole transition matrix elements which are on their part directly dependent on the double-group representations of electronic states and the dipole operator.
How the intensity and the asymmetry actually depend on the transition matrix elements can best be shown by evaluating the general equations (2.39) and (2.40) for a particular crystal direction. Here we show the results for the (111)-surface in the case of circular polarization and a totally symmetric setup. Furthermore, we neglect SOC in the final states. For reasons of

clarity hybridization due to forbidden degeneracies is also not taken into account. A mixing of spatial symmetries and spin characters within one band is therefore avoided, and bands can explicitly be separated by the exchange splitting. In the following we thus use the nomenclature of the nonmagnetic double-group representation with Kramers-degeneracy lifted.
According to the relativistic dipole selection rules transitions take place between $\Lambda^3_{4,5}$- and Λ^3_6 initial and Λ^1_6 final states (c. f. Table 2.1, right column). The corresponding partial matrix elements are denoted as $M_i^{ss'}$. As an example, $M_{4,5}^{+-}$ indicates the transition from $\Lambda^3_{4,5}-$ initial states to final states with Λ^1_6+ symmetry.
For initial states with Λ^3_6-symmetry we obtain

$$I(\sigma^+) = 2\left|M_6^{+-}\right|^2 \quad , \quad I(\sigma^-) = 2\left|M_6^{-+}\right|^2. \tag{2.41}$$

Apparently, for fixed light helicity only Λ^3_6+ *or* Λ^3_6- initial states can be excited which leads to an enhanced dichroic signal [6].
For the $\Lambda^3_{4,5}$ initial states one has

$$I(\sigma^+) = \left|M_{4,5}^{-+}\right|^2 + \left|M_{4,5}^{--}\right|^2 \quad , \quad I(\sigma^-) = \left|M_{4,5}^{+-}\right|^2 + \left|M_{4,5}^{++}\right|^2. \tag{2.42}$$

Here, initial states with $\Lambda^3_{4,5}+$ *and* $\Lambda^3_{4,5}-$-symmetry are excited for both helicities. The dichroic contributions from these bands are thus expected to be much smaller than for the Λ^3_6 initial states. For the MCD asymmetry it follows

$$A = I(\uparrow\uparrow) - I(\uparrow\downarrow) \tag{2.43}$$

with

$$\begin{aligned} I(\uparrow\uparrow) &= 2\left|M_6^{+-}\right|^2 + \left|M_{4,5}^{-+}\right|^2 + \left|M_{4,5}^{--}\right|^2 \\ I(\uparrow\downarrow) &= 2\left|M_6^{-+}\right|^2 + \left|M_{4,5}^{+-}\right|^2 + \left|M_{4,5}^{++}\right|^2 \end{aligned} \tag{2.44}$$

for parallel and antiparallel alignment of the helicity- and the magnetization vector [6].
Eq. (2.43) and (2.44) give the MCD asymmetry for photoemission from a (111) surface in a totally symmetric setup. They furthermore show that the origin of magnetic circular dichroism is attributed to the two physical phenomena of spin-orbit coupling and exchange interaction: In the non-magnetic case (no exchange-splitting) we cannot distinguish between majority and minority spin states. This means $M_i^{+-} = M_i^{-+}$ and $M_i^{++} = M_i^{--}$ which leads to a vanishing asymmetry in (2.43). On the other hand the partial matrix elements $M_{4,5}$ and M_6 in Eq. (2.44) only arise from the simultaneous presence of both symmetry types $\Lambda^3_{4,5}$ and Λ^3_6 in the initial states [33] which is explicitly caused by spin-orbit coupling. For these reasons *both* phenomena are essential for the occurrence of magnetic circular dichroism in valence band photoemission. With respect to the magnitude of single contributions we have already stated that the dichroic signal arising from the $\Lambda^3_{4,5}$-symmetry bands is much smaller than the one attributed to the Λ^3_6 states. The main reason for this behavior is due to the small exchange splitting in the final states: Changing the helicity at fixed magnetization in (2.42) triggers transitions from

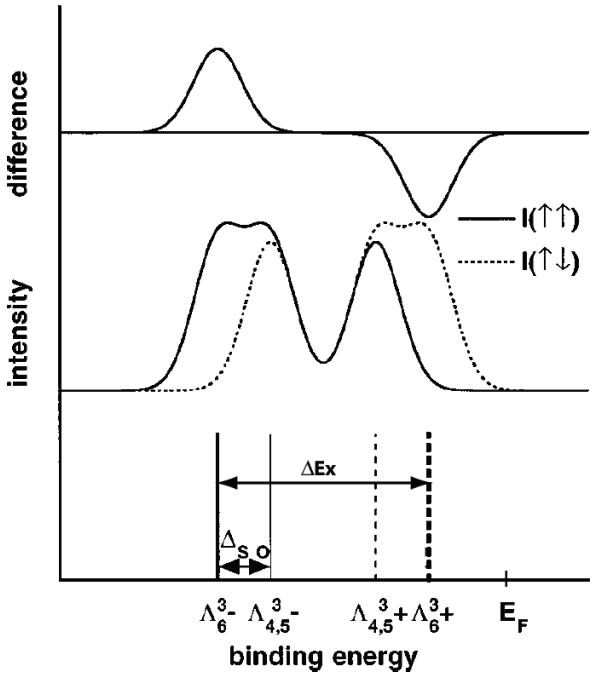

Figure 2.6: Schematic drawing for an MCD experiment on a (111) surface in a totally symmetric setup (taken from Ref. [6]). (Bottom) Contributing initial states separated by spin-orbit coupling and exchange splitting (see arrows). (Center) Intensity spectra for parallel (full curve) and antiparallel (dotted curve) alignment of the helicity- and the magnetization vector. (Top) Non-normalized MCD asymmetry deduced from the two intensity spectra of the center panel.

the same initial states into different final states. The difference in the final states is, however, marked by a vanishingly small exchange-splitting. If we completely neglect this splitting, the dichroic contribution from the $\Lambda^3_{4,5}$ states vanishes; otherwise it only contributes little. The comparably small exchange splitting in the final states is also responsible for the fact that the main features in an intensity spectrum are brought by the selection of different initial states for the two light helicities. Fig. 2.6 depicts the contributing bands and the resulting dichroic signal in an energy-resolved diagram. On the bottom side the contributing initial states Λ^3_6+, Λ^3_6-, $\Lambda^3_{4,5}+$ and $\Lambda^3_{4,5}-$ which are separated by spin-orbit coupling and exchange-splitting (see arrows) are depicted by vertical lines. The center shows intensity curves for parallel (full line) and antiparallel (dotted line) orientation of the photon helicity with respect to the magnetization direction. Note that only for reasons of illustration the intensity peaks appear with approximately equal height. However, since each transition contributes heavily dependent on the magnitude of its transition matrix element this does not reproduce the real experimental situation. The top panel finally reflects the non-normalized MCD asymmetry deduced from the two intensity spectra of the center panel. The asymmetry peaks are located at the energetic

positions of the Λ_6^3 initial states. This reflects the fact that the main dichroism is delivered by transitions involving these initial states. The analytical expressions presented above have been tested in an extensive study on the threefold-symmetry surface of fcc Co/Cu(111) with perpendicular magnetization [6]. Comparable work has also been done for the fourfold-symmetry surface of fcc Ni/Cu(001) [7]. In both cases the experiments showed that the description of MCD in the framework of the presented formalism is a valid approach.

2.3 Computational aspects

The last section has given a microscopic insight into the physical mechanisms involved in magnetic circular dichroism in valence band photoemission. Thereby it became clear that the magnetic asymmetry is, of course, not only an experimental quantity determined by measuring intensity spectra for light of different circular polarization at fixed magnetization direction. Rather, by knowing the band structure of a material as well as the dipole selection rules the dichroic intensities can explicitly be calculated. This enables a theoretical prediction of magnetic asymmetries and a direct relation to experimental results. Since the comparison of theoretical calculations and MCD measurements is a major issue of this work, the following section points out how the asymmetries are explicitly calculated in our case.

2.3.1 Band-structure calculations

All MCD calculations are established on the basis of band structure simulations for which many approaches have been developed during the last decades. A breakthrough was marked by the development of *density-functional theory* (DFT) with which an accurate band-structure calculation became possible for many cases. The method in its further elaborated form of local spin-density approximation (LSDA) is also used in this work for the simulation of a Co(111) band structure. In the following we only present the main ideas of DFT. For detailed information we refer to [35, 36].

Density functional theory determines the quantum mechanical ground state [8] of a N-electron system using the electron density of the system. The approach is based on the idea that a ground state of a many-electron system is uniquely determined by a distinct, spatially-dependent electron density $n(\vec{r})$. Furthermore, it can be shown that for an arbitrary electron density $n^*(\vec{r})$ the ground state energy is $E_\mathrm{G} \leq E[n^*(\vec{r})]$, while for $n^*(\vec{r}) = n(\vec{r})$ the energy of the ground state is obtained. This means that the electron density of the ground state minimizes the energy functional of the system. These theorems are called the *Hohenberg-Kohn theorems* and represent the starting point for all following considerations. In fact, the determination of $n(\vec{r})$ can deliver all other properties of the ground state. To obtain the electron density the Schrödinger equation for the N-electron system has to be solved. This procedure likewise reveals the major advantage of DFT upon other theories: Instead of solving

[8] Note that in DFT the nuclei are assumed to be fixed; only the electrons are treated quantum mechanically. This approach is called Born-Oppenheimer approximation.

the Schrödinger equation for N electrons simultaneously, one can generate N independent one-electron solutions ϕ_i. The corresponding one-electron Schrödinger equations are called *Kohn-Sham equations* and are given by

$$\Big(-\frac{\hbar^2}{2m}\vec{\nabla}^2 + v_{\text{eff}}(\vec{r}) - \epsilon_i \Big)\phi_i(\vec{r}) = 0, \tag{2.45}$$

where ϕ_i are the one-electron wave-functions. They are directly connected to the electron density via the relation

$$n(\vec{r}) = \sum_{i=1}^{N} \big|\phi_i(\vec{r})\big|^2. \tag{2.46}$$

The term v_{eff} in (2.45) is the effective potential that also depends on the electron density:

$$v_{\text{eff}} = v(\vec{r}) + \int \frac{n(\vec{r}\,')}{\big|\vec{r} - \vec{r}\,'\big|} d^3r' + v_{\text{xc}}(\vec{r}). \tag{2.47}$$

Here, $v(\vec{r})$ denotes the attractive potential generated by the nuclei, while the second term describes the electrostatic interaction among the electrons. The last term v_{xc} is the so-called exchange correlation potential which accounts for the correct treatment of the many-electron system and plays a decisive role in the determination of the ground state. We notice that the effective potential depends on the one-electron wave functions (via (2.46)) and therefore turns (2.45) into an implicit equation. Solutions can thus only be generated by an iterative procedure, finally yielding a self-consistent result. Additionally, we have to consider the exchange correlation potential which also depends on the electron density and which can be explicitly calculated only for a few trivial cases. Therefore, an approximation for v_{xc} has to be implemented.

Depending on the particular characteristics of these approximations one classifies different methods. The most widely-used procedure is *local density approximation* (LDA), which is also applied in our simulations. LDA assumes that $v_{\text{xc}}(\vec{r})$ is a function of the electron density $n(\vec{r})$ only at the position of $\vec{r}$ (i. e only at the position, where it is evaluated). It can be applied in many cases and especially delivers good results, if the electron density is approximately the same anywhere. This is, for example, true for the conduction electrons in a metal. For this work the LDA-approach is enlarged to local spin density approximation (LSDA), where separate calculations are carried out for the two different spin directions.

Furthermore, one distinguishes between the set of basis functions used to evaluate the Kohn-Sham equations. While atomic wave functions (muffin-tin orbitals) are used to describe electrons in the vicinity of the nucleus, plane waves deliver a good description of valence and conduction electrons. A combination of both (e. g. augmented spherical waves) provides a description of the regions very close as well as far away from the nucleus. Augmented spherical waves are also used in our calculations.

Note that despite the multiple good agreement between DFT-calculated band structures and experimental band mappings, DFT can only deliver energy values for a fictive non-interacting

sytem. Thus, the derived electronic structure is not directly related to the quasiparticle electronic structure of a real system.
Finally, note that for our calculations fully-relativistic density functional theory has been used, meaning that spin-orbit coupling and relativistic dipole selection rules have explicitly been taken into account. The calculated Co(111) band structure thus reveals hybridization gaps due to avoided crossings, where the spatial symmetry as well as the spin character changes continually within the corresponding bands. To simplify the nomenclature the bands are therefore indicated only by numbers beginning with the bottommost valence band, as mentioned above.

2.3.2 Calculation of the MCD asymmetry

MCD asymmetries are calculated via different approaches. On the one hand, dichroic signals can be simulated by evaluating the spin density matrix for the photocurrent (2.34) on the basis of a three-step or a one-step formalism. On the other hand one can use an approach which especially refers to the magneto-optical nature of magnetic circular dichroism. This point of view was briefly mentioned in Ch. 2.2 and will be discussed in detail below.
In Eq. (2.32) it was stated that MCD is often described by a difference in the absorption coefficients for left- and right-circularly polarized light. This connection will be verified in the following. Furthermore, we show that the MCD asymmetry is directly related to the so-called *conductivity tensor* σ. We start with Eq. (2.33) for the normalized MCD asymmetry,

$$A = \frac{I^{\sigma^+} - I^{\sigma^-}}{I^{\sigma^+} + I^{\sigma^-}}. \tag{2.48}$$

To estimate the intensity of the created photoelectrons $I^{\sigma^\pm}$ for the two polarizations, we assume that it is proportional to the intensity of light absorbed in the medium, i. e.

$$I^{\sigma^\pm} \propto I^{\sigma^\pm}_{\mathrm{abs}} = I_0\big(1 - \exp(-\mu^\pm d)\big), \tag{2.49}$$

where we have used Beer's law $I = I_0 \cdot \exp(-\mu d)$ for the description of light absorption [37]. Therein, I_0 is the incoming photon intensity and d corresponds to the penetration depth of light or the escape depth of the electrons; $\mu^\pm$ is the absorption coefficient for the two light helicities. Inserting of (2.49) into (2.48) leads to

$$\begin{aligned} A &= \frac{(1 - e^{-\mu^+ d}) - (1 - e^{-\mu^- d})}{(1 - e^{-\mu^+ d}) + (1 - e^{-\mu^- d})} = \frac{e^{-\mu^- d} - e^{-\mu^+ d}}{2 - e^{-\mu^+ d} - e^{-\mu^- d}} \\ &\approx \frac{1 - \mu^- d - 1 + \mu^+ d}{2 - (1 - \mu^+ d) - (1 - \mu^- d)} = \frac{\mu^+ - \mu^-}{\mu^+ + \mu^-}, \end{aligned} \tag{2.50}$$

where we have used a Taylor expansion of the exponential function. Eq. (2.50) demonstrates that the MCD asymmetry is in fact directly related to the difference in the absorption coefficients. Note that in this approximation the d-dependence vanishes, while this is avoided in real simulations, where a small dependence on d still exists.

Furthermore, the absorption coefficient for light is given by $\mu^{\pm} = -2\omega \mathrm{Im}[n^{\pm}]/c$. Here $n^{\pm}$ describes the refractive index for left-and right-circularly polarized light which according to the Fresnel theory is given by $(n^{\pm})^2 = \epsilon_{xx} \pm i\epsilon_{xy}$ (if the magnetization is parallel to a local z-axis); ϵ_{xx} and ϵ_{xy} are components of the dielectric tensor ϵ [9]. Using the expression for μ the asymmetry follows to

$$A \approx \frac{\mathrm{Im}[n^+] - \mathrm{Im}[n^-]}{\mathrm{Im}[n^+] + \mathrm{Im}[n^-]} = \frac{\mathrm{Im}[n^+ - n^-]}{\mathrm{Im}[n^+ + n^-]}. \tag{2.51}$$

With $n^{\pm} = \sqrt{\epsilon_{xx} \pm i\epsilon_{xy}} \approx \sqrt{\epsilon_{xx}} \pm i\frac{\epsilon_{xy}}{2\sqrt{\epsilon_{xx}}}$ for ϵ_{xy} being small, we can write

$$\mathrm{Im}[n^+ - n^-] \approx \mathrm{Im}\left[\frac{i\epsilon_{xy}}{\sqrt{\epsilon_{xx}}}\right] \quad \text{and} \quad \mathrm{Im}[n^+ + n^-] \approx \mathrm{Im}\left[2\sqrt{\epsilon_{xx}}\right], \tag{2.52}$$

which results in

$$A \approx \frac{\mathrm{Im}\left[\frac{i\epsilon_{xy}}{\sqrt{\epsilon_{xx}}}\right]}{\mathrm{Im}\left[2\sqrt{\epsilon_{xx}}\right]}. \tag{2.53}$$

Considering that ϵ is directly related to σ by $\epsilon_{ij} = \delta_{ij} + \frac{4i\pi}{\omega}\sigma_{ij}$ [38] the last equation can be re-written in the form

$$A \approx -\frac{4\pi}{2\omega} \frac{\mathrm{Im}\left[\frac{\sigma_{xy}}{\sqrt{1+\frac{4i\pi}{\omega}\sigma_{xx}}}\right]}{\mathrm{Im}\left[\sqrt{1+\frac{4i\pi}{\omega}\sigma_{xx}}\right]} \tag{2.54}$$

which cannot be further simplified, since the square root cannot be easily expanded for metals in the optical range [37]. Nevertheless, one realizes that the effect is approximately proportional to σ_{xy}. The magnetic asymmetry can obviously be evaluated once having calculated the optical conductivity. Furthermore, ϵ can be derived from σ which enables the determination of $\mu^{\pm}$ subsequently and of the electron intensities $I_e^{\pm}$. In the following we will shortly describe how the optical conductivity can be calculated.

Computation of the optical conductivity tensor σ

The conductivity tensor for magnetic materials depends on the crystal symmetry and the magnetization direction with respect to the crystal axis. Thereby, the magnetization leads to the appearance of the off-diagonal element σ_{xy} which is the decisive quantity for the occurrence

[9] The dielectric tensor relates the electric displacement $\vec{D}$ with the electric field $\vec{E}$ via $\vec{D} = \epsilon \cdot \vec{E}$. A similar material equation is fulfilled for the conductivity which relates the current density $\vec{j}$ to the electric field by $\vec{j} = \sigma \cdot \vec{E}$. Note that these equations are only valid for a homogeneous material [38] which is assumed for the present calculations. This is also the reason why ϵ and σ are considered to depend only on the photon frequency.

of MCD. For a cubic system with magnetization oriented along the surface normal the conductivity tensor is given by [25]

$$\sigma(\omega) = \begin{pmatrix} \sigma_{xx} & \sigma_{xy} & 0 \\ -\sigma_{xy} & \sigma_{xx} & 0 \\ 0 & 0 & \sigma_{zz} \end{pmatrix}. \tag{2.55}$$

This structure is valid for sample systems which exhibit an at least three-fold rotational axis coinciding with the magnetization direction. The most general access for the calculation of Eq. (2.55) is given by Kubo's linear-response formalism delivering a complete derivation of all tensor elements [39, 40], which is also used in this work. In Kubo's approach the conductivity is evaluated as the response function of the current density to the electric field (Ohm's law). For reasons of clarity we present here a more facile method which is also widely used and equivalent to our formalism. It is provided by firstly calculating the absorptive parts of σ only. The dispersive elements are determined afterwards by use of the so-called *Kramers-Kronig relations* (see below). In this framework calculations by Bennett and Stern [41] delivered the following results for the absorptive parts of the conductivity tensor [25]:

$$\sigma^1_{xx}(\omega) = \frac{\pi e^2}{2\hbar\omega m^2 V} \sum_{\substack{j'\vec{k}\,\text{occupied} \\ j\vec{k}\,\text{unoccupied}}} \left[\left|\Pi^+_{jj'}\right|^2 + \left|\Pi^-_{jj'}\right|^2 \right] \delta\big(\omega - \omega_{jj'}\big), \tag{2.56}$$

$$\sigma^2_{xy}(\omega) = \frac{\pi e^2}{2\hbar\omega m^2 V} \sum_{\substack{j'\vec{k}\,\text{occupied} \\ j\vec{k}\,\text{unoccupied}}} \left[\left|\Pi^+_{jj'}\right|^2 - \left|\Pi^-_{jj'}\right|^2 \right] \delta\big(\omega - \omega_{jj'}\big). \tag{2.57}$$

The superscript 1 indicates the real part, while 2 denotes the imaginary part of the particular tensor element. The major quantities in the upper equations are the matrix elements

$$\Pi^\lambda_{jj'} = \left\langle \Psi_{j\vec{k}} \middle| p_\lambda \middle| \Psi_{j'\vec{k}} \right\rangle \tag{2.58}$$

with $p_+ = p_x + ip_y$ and $p_- = p_x - ip_y$ which can be thought to come from $\vec{A}\cdot\vec{p}$ terms [10]. The wave functions $\left|\Psi_{j\vec{k}}\right\rangle$ are Bloch states described by the wave vector $\vec{k}$ and a band index j, and $E_{j,\vec{k}}$ are the corresponding energy eigenvalues, determining the absorption of a photon of energy $\hbar\omega$ by

$$\omega_{jj'} = \frac{E_{j,\vec{k}} - E_{j',\vec{k}}}{\hbar}. \tag{2.59}$$

The upper expression directly guarantees energy conservation via the δ-functions in (2.56) and (2.57). Also note that with (2.59) only $\vec{k}$-conserving transitions ($\Delta\vec{k} = 0$) are considered. This means that only direct interband transitions ($j \neq j'$) between initial and final Bloch states are taken into account. It is clear that at this point our method is strongly based on the three-step

[10] Here, the non-relativistic form of the matrix elements is used to simplify matter. In a precise treatment the momentum operator of the Dirac formalism is, of course, utilized.

model whose application for our case was already pointed out in Ch. 2.1. A comparison of the theoretical results with our experimental investigations in Ch. 4 will also demonstrate that this is an adequate approach for treating MCD in the near-threshold region of Co(111).
We finally point out that the $\vec{k}$-values in (2.56) and (2.57) are summed up over all Brillouin-zones. Due to the periodicity of the lattice this can be limited to a summation over the first zone only. Moreover, in actual calculations the summation is replaced by an integration over $\vec{k}$-space in the first BZ. This is also done within our program code. The calculated asymmetry is therefore not attributed to a single band-to-band transition but is a result of an averaging over all possible interband transitions in all $\vec{k}$-directions of the whole BZ. In order to obtain the complete conductivity tensor we use the connection between the absorptive and dispersive parts by the Kramers-Kronig-relations [42, 43] which are

$$\begin{aligned} \sigma^{(1)}_{\alpha\beta}(\omega) &= \frac{2}{\pi} P \int_0^\infty d\omega' \frac{\omega'}{\omega'^{\,2} - \omega^2}\, \sigma^{(2)}_{\alpha\beta}(\omega'), \\ \sigma^{(2)}_{\alpha\beta}(\omega) &= -\frac{2}{\pi} P \int_0^\infty d\omega' \frac{\omega}{\omega'^{\,2} - \omega^2}\, \sigma^{(1)}_{\alpha\beta}(\omega') \end{aligned} \tag{2.60}$$

where P is the principal value of the integral.
Note that σ is often used in an extended version to account for additional effects arising in the process of absorption. One of the most important effects is the finite lifetime effect: If a state is optically excited, it decays after a certain relaxation time which is also called the lifetime of the state. Its occurrence is also the reason why a transition is not infinitely sharp. The lifetime is phenomenologically taken into account by substituting $\omega \Rightarrow \omega + i\delta = \omega + i/\tau$, where τ is the lifetime. Each transition is thereby convoluted with a Lorentz function, whose half width at half maximum is given by τ^{-1}. Although the interband relaxation time depends on the energy of the excited states, the assumption of a constant lifetime yields satisfying results. Especially the comparison between experimental and theoretical MOKE studies [44] showed that the parameter range $\hbar\,\delta = 0.03 - 0.05\,\mathrm{Ry}$ is a good estimate for the lifetime values in transition metal compounds. Values of this order of magnitude will also be used in this work.

Computation of the matrix elements

The optical conductivity can be calculated not until the matrix elements in Eq. (2.58) are known. In fact they are one of the most important quantities for the calculation of the MCD asymmetry due to their strong influence on σ_{xy}. As mentioned they are evaluated between initial and final Bloch states as done in an optical excitation, being consistent with the three step model and following the relativistic dipole selection rules presented in Ch. 2.2.1. Thereby, the most delicate step displays the selection of a preferably complete set of basis functions for the construction of the Bloch waves $\Psi_n(\vec{r}) = \sum_\nu C^n_\nu\, \Phi_\nu(\vec{r})$. A possible choice has already been given in Ch. 2.2.2 (Eq. (2.36)). With an insufficient basis-set an accurate determination of the Bloch functions is not possible which particularly affects the final state wave functions. To avoid such problems in our calculation, the basis-set consisting of augmented spherical waves, is increased by adding unaugmented, free electron waves (plane waves) [38]. In this

way a better convergence is achieved.
Finally, we want to give some brief comments on the last sections. With respect to the calculation of the optical conductivity we have shown that a straightforward method is given by initially evaluating the absorptive elements (for $\delta \to 0$) from which the dispersive terms can be derived in a second step by applying the Kramers-Kronig relations. Finite-lifetime effects are then regarded by convolving both terms with a Lorentz function. In the approach actually used for this work all elements of the conductivity tensor are derived simultaneously by a direct integration in the complex plane for $\delta \neq 0$. Thereby, the Kramers-Kronig equations are not needed and the case of $\delta \to 0$ is already included in the calculations.
Furthermore, it is worth mentioning that the program code used for this work was originally developed for simulations of the magneto-optical Kerr effect (MOKE) which also arises from an interplay between the spin-orbit coupling and the exchange interaction, and which is evaluated via the presented calculation of the optical conductivity tensor on the basis of a DFT-simulated band structure. To finally apply the code to our experimental conditions we have to consider that the photon-in photon-out situation of MOKE, has to be transfered to a setting, where an incident photon excites a photoelectron into vacuum. Therefore, the conditions for the occurrence of photoemission, e. g. $h\nu \geq \Phi$, have additionally to be taken into account.

3 Experimental techniques

3.1 Sample preparation

After magnetic circular dichroism in two-photon photoemission was confirmed to appear in two Heusler alloys (see Ch. 4.1) ultrathin Co films on Pt(111) have been prepared and investigated. A combination of Co and Pt does not only offer the necessary preconditions for large MCD signals; it also promises an easier interpretation of the results due to a manageable band-structure scheme. All samples are prepared at room temperature in ultrahigh vacuum chambers (base pressure $< 3 \cdot 10^{-10}$ mbar) by electron-beam evaporation. Details of the particular preparation steps are given in the corresponding chapters (Ch. 4.2 - Ch. 4.4). Fig. 3.1 shows the substrate (W(110)) used for sample preparation in Mainz. It is placed in a molybdenum sample holder which allows an effective substrate diameter of 5 mm to be used for evaporation. The picture depicts a test sample revealing the pure tungsten surface on the left side of the substrate followed by three stripes of different Co-monolayer thicknesses (10 ML, 20 ML and 30 ML, see arrows) which are visible to the naked eye.
As already mentioned in Ch. 2.2 an optimal geometry for the appearance of MCD effects is the

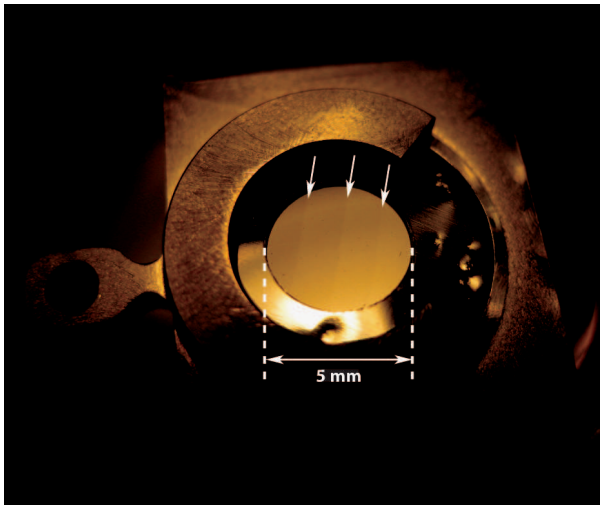

Figure 3.1: Picture of the sample system (substrate (5 mm diameter) and sample holder) used for sample preparation in Mainz. Shown is a test sample with the pure W(110) surface on the left end of the substrate followed by ultrathin Co stripes of different thicknesses (10 ML, 20 ML and 30 ML; ML: monolayer) which are indicated by arrows.

totally symmetric setup for which the sample magnetization has to be oriented perpendicular to the surface. This can be achieved for all samples using a sufficiently large external field. In this context, films with an easy magnetization axis pointing out of the sample plane extremely reduce the needed external field from values of the order of the saturation magnetization (2 T) to the coercive field of the measured sample (< 0.2 T). This has also been taken into account for the Co samples so that in each case (except for the thickness-dependent measurements in Ch. 4.2) the Co films reveal a perpendicular anisotropy with a remanent magnetization vector pointing out of the film plane. The maximum number of monolayers for out-of-plane anisotropy is marked by the so-called *spin reorientation transition* (SRT). It separates thickness regions for which the remanent magnetization is oriented out of the sample plane from those with an in-plane orientation. Since the position of the SRT is determined by the different contributions to the sample-specific magnetic anisotropy it strongly depends on the sample composition. A variation of the SRT-position is in many cases possible by annealing the prepared sample as well as by using additional capping layers. In our case a Co thickness close to the SRT revealing an increased number of monolayers is chosen. This is advantageous as it provides a bulk-like band structure and thereby assures an adequate comparison with calculated band-structure schemes, which are in our case simulated for the bulk of the material and a magnetization oriented parallel to the surface normal.
The quality of the substrate surfaces and the epitaxial films is checked by low energy electron diffraction (LEED). Selected LEED images are presented in Ch. 4.2 and 4.3 of this work. For details concerning LEED and the used evaporation techniques we refer to Ref. [45].

3.2 Magneto-optical Kerr measurements

In order to determine the magnetic features of the sample, Kerr measurements are carried out in the polar and longitudinal geometry. Magneto-optical Kerr measurements in these geometries detect a change in the polarization direction of incident linearly polarized radiation after its reflection from a magnetic sample [46]. As a magneto-optical effect it arises from the simultaneous appearance of spin-orbit coupling and exchange splitting [47, 48]. The essential quantities, the *Kerr rotation* θ_{K} and the *Kerr ellipticity* ϵ_{K}, are directly related to the optical conductivity tensor via [25]

$$\Phi_{\mathrm{K}} = \theta_{\mathrm{K}} + i\epsilon_{\mathrm{K}} \cong \frac{\sigma_{xy}}{\sigma_{xx}\sqrt{1 - \frac{4\pi i}{\omega}\sigma_{xx}}}, \tag{3.1}$$

where Φ_{K} marks the *complex Kerr angle*. For a short overview concerning this effect we refer to Ref. [45]; extensive reviews are given in Ref. [38, 49]. For this work, ex-situ as well as in-situ experimental setups are used to detect the Kerr signals θ_{K} and/or ϵ_{K}. A schematic drawing of the experiments in the polar setup where the sample magnetization is oriented out of the sample plane is sketched in Fig. 3.2. Linearly polarized laser light (670 nm in the ex-situ setup, 636 nm in the in-situ setup) is focused onto the sample under an angle of 45° with respect to the surface normal. After passing an analyzer the reflected light is finally detected by a photo

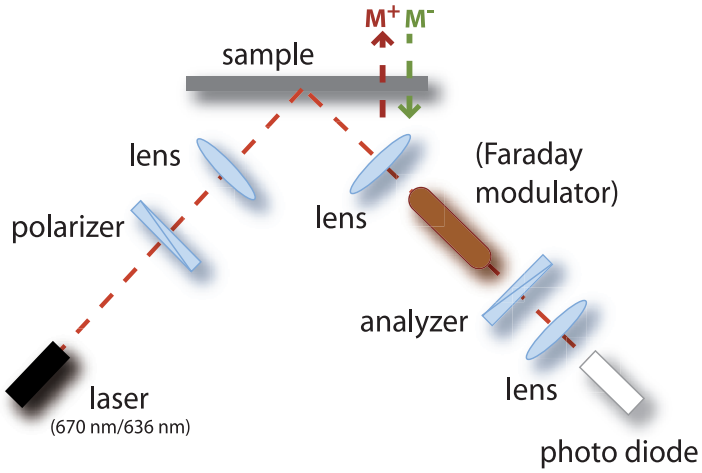

Figure 3.2: Schematic drawing of the experimental setup for measurements of the polar magneto-optical Kerr effect (PMOKE).

diode. In the longitudinal geometry an external magnetic field saturates the sample magnetization along the sample plane. By additionally using a Faraday modulator in combination with lock-in technique especially small Kerr signals can be detected [50]. This is necessary for the investigation of capped sample systems revealing smaller Kerr effects, as presented in Ch. 4.2.
As a result of the measurements the Kerr rotation angle and the Kerr ellipticity can be plotted against the external magnetic field. Depending on the intrinsic direction of the sample magnetization, hard or easy axis magnetization curves are detected. The absolute values for the Kerr signals as well as the behavior of the magnetization curves give important information about the magnetic properties of the system and the quality of the deposited film. As an easy technique, it serves as a first test whether the magnetization of the sample can be switched parallel and antiparallel to the available field.

3.3 Magnetic circular dichroism measurements

For this work magnetic circular dichroism (MCD) measurements are carried out with two different experimental setups:

(a) Capped systems (cf. Ch. 4.1 & Ch. 4.2)

The first setup (at the University of Mainz) allows solely for MCD measurements of ex-situ prepared samples; in situ sample preparation is not possible. The samples are therefore prepared in a UHV preparation chamber and afterwards transferred to the measurement chamber. Thus all samples have to be capped by an additional layer to prevent them from oxidation.

The magnetic properties can be checked by ex-situ Kerr measurements. Since Kerr as well as MCD signals are reduced by an additional capping layer (see Ch. 4.2) a lock-in measurement technique is necessary to detect the dichroic effects. Fig. 3.3 (a) schematically shows the experimental setup: Frequency-doubled and frequency-tripled radiation from a titanium sapphire femtosecond laser (hν = 4.64 eV (1PPE), hν = 3.10 eV (2PPE)) is used as excitation source. The laser pulse length for the frequency-doubled radiation which is needed for 2PPE processes is $\tau \sim 200$ fs. For the frequency-tripled laser light generating 1PPE processes it amounts to $\tau \sim 300$ fs. The repetition rate of the pulses is 80 MHz.
For a proper definition of the linear polarization vector relative to the subsequent quarter-wave plate the laser beam initially passes a polarizer. The quarter wave plate is built into a rotatable motor mount which rotates at a frequency of $\omega_{\mathrm{ref}}/2\pi = 10$ Hz and periodically modulates the polarization with a frequency of $2\omega_{\mathrm{ref}}$. Photoemission is excited by focusing the polarization modulated laser beam onto the sample which is placed under high vacuum in the gap of a commercial electromagnet generating a homogeneous magnetic field of up to 1.12 T at the sample position. The total photoelectron yield I_{e} is measured by a picoamperemeter recording the photocurrent upon laser irradiation via the sample current. A bias voltage of +100 V is applied to a cylindrical counter electrode to extract the photoemission current. For a polarization-sensitive detection of the photocurrent, the voltage output from the picoamperemeter is used as input signal of a lock-in amplifier. This enables a phase-selective measurement of the $2\omega_{\mathrm{ref}}$-intensity modulation. The rotation frequency of the quarter wave plate thereby serves as external reference frequency for the lock-in amplifier. By optimizing the phase adjustment of the lock-in amplifier, the photocurrent modulation that is caused by the polarization modulation of the light is recorded at a low signal-to-noise ratio. Fig. 3.3 (b) gives a detailed view of the two basic experimental possibilities to measure the MCD effect in a totally symmetric setup: On the one hand, MCD can be identified by a difference in the photoemission current $I_{\mathrm{e}}^{+} - I_{\mathrm{e}}^{-}$ under change of the magnetization direction $\vec{M}^{+} \rightarrow \vec{M}^{-}$ at fixed photon helicity. The sample magnetization $\vec{M}$ is thereby switched between parallel and antiparallel alignment with respect to the helicity vector $\vec{\Lambda}_{\sigma}$ of the circularly polarized laser light under normal incidence to the surface (left side of Fig. 3.3 (b)). On the other hand, for the totally symmetric geometry MCD can equivalently be measured with fixed magnetization orientation and a change in photon helicity $\vec{\Lambda}_{\sigma^{+}} \rightarrow \vec{\Lambda}_{\sigma^{-}}$ (right side of Fig. 3.3 (b)). In both approaches the sample is magnetically saturated in the out-of-plane direction. Note that in the setup of Fig. 3.3 (a) the polarization does not only switch between the two circular polarizations σ^{+} and σ^{-} but is changed periodically with the frequency $2\omega_{\mathrm{ref}}$ for one magnetization direction. In the ideal case, this yields a constant lock-in voltage output and reflects the MCD asymmetry for one magnetization orientation. Changing the magnetization direction inverts the lock-in output signal and yields the corresponding MCD asymmetry. The difference between both output signals for the two magnetization directions at periodically changing light polarization finally gives the total MCD asymmetry. For details concerning the laser system and the lock-in technique we refer to Ref. [45].

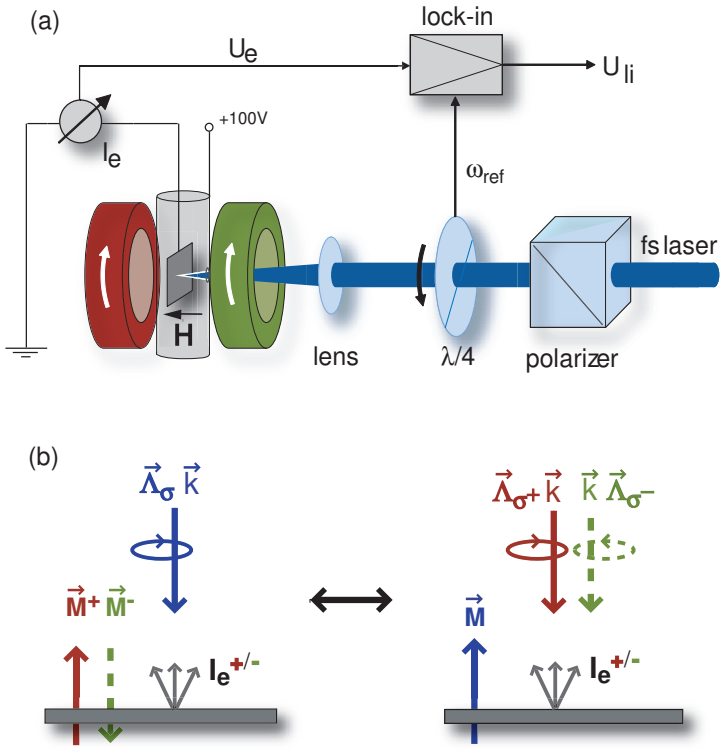

Figure 3.3: Schematic view of the MCD experiment. (a) TiSa femtosecond laser light is used for a polarization-sensitive detection of the photoemission current from perpendicularly magnetized samples via lock-in technique. (b) Detailed view of the two experimental possibilities to measure the MCD effect based on recording the photoemission current I_e upon irradiation with circularly polarized femtosecond laser light. Magnetic circular dichroism can be identified from a difference $I_e^+ - I_e^-$ in the photoemission yield under change of either the magnetization $\vec{M}^+ \rightarrow \vec{M}^-$ at fixed photon helicity (left figure) or the photon helicity $\vec{\Lambda}_{\sigma^+} \rightarrow \vec{\Lambda}_{\sigma^-}$ at fixed magnetization orientation (right figure). In both cases the sample is magnetically saturated in the out-of-plane direction and the helicity vector is oriented normal to the sample surface (totally symmetric setup).

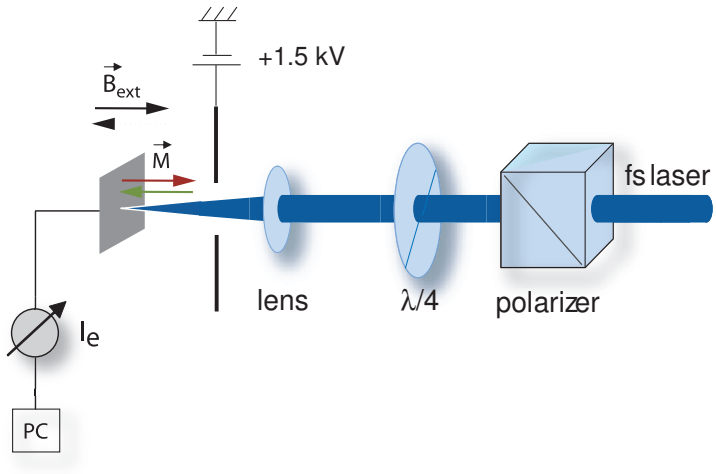

Figure 3.4: Schematic drawing of the experimental setup for MCD measurements in near-threshold photoemission.

(b) Uncapped systems (cf. Ch. 4.3 & Ch. 4.4)

In the second setup (which was used during a two months stay at the Institute for Molecular Science in the group of Prof. Yokoyama in Okazaki, Japan) sample preparation, PMOKE- and MCD-measurements are carried out in the same UHV-chamber. Therefore, an additional capping layer is not necessary. Fig. 3.4 shows the setup for the MCD measurements in near-threshold photoemission. For the excitation of the photoelectrons a broadband ultrashort pulse laser ($\tau < 100$ fs for the fundamental, 80 MHz repetition rate) is used. 1PPE processes are triggered by using frequency-quadrupled radiation in the energy range $h\nu = 5.06$ - 5.84 eV. For 2PPE, frequency-doubled laser light ($h\nu = 2.46$ - 2.92 eV) is utilized. By means of apertures and a lens, the laser beam is directed into the vacuum chamber where the sample is placed between the pole shoes of an electromagnet, generating a maximum magnetic field of $\mu_0 H = 0.3$ T. Circular polarization is produced by a combination of a linear polarizer and a quarter wave plate for the corresponding wavelengths. The sample current is finally measured by placing an anode plate (1478 V - 1970 V) in front of the sample collecting all photoemitted electrons. Since the dichroic signals are large enough, the use of lock-in technique is not necessary. During all measurements (except for the angle-dependent experiments) the magnetization vector is oriented along the surface normal and parallel to the helicity vector of the incoming laser light. In this setup, MCD is identified by a difference in the photoemission current under change of the magnetization direction at fixed photon helicity.
Finally, note that in all measurements the total photoelectron yield has been detected. The kinetic energy or the spin of the excited electrons are therefore not analyzed separately. All PMOKE- and MCD-measurements are carried out at room temperature.

4 Results and Discussion

4.1 Near-threshold MCD in Two Photon Photoemission

4.1.1 Motivation

Nowadays magnetic dichroic effects have attracted much interest and developed into various experimental methods. In contrast to synchrotron-based X-ray magnetic circular and linear dichroism (XMCD and XMLD) which benefits from large asymmetry values of more than 30 % [2, 3, 4], only little work has been performed on magnetic dichroism in near-threshold photoemission using laboratory light sources. In 2000 Marx et al. demonstrated magnetic linear dichroism (MLD) in one-photon-photoemission electron microscopy by using a mercury arc lamp ($h\nu < 5$ eV) [8]. In these measurements an asymmetry of 0.37 % was detected for a 100 nm polycrystalline Fe film. Remarkable MCD asymmetries of $\geq 10\,\%$ directly at the threshold were found for 1PPE by Nakagawa and Yokoyama in 2006 by investigating a perpendicularly magnetized Ni film on Cu(001) with visible and ultraviolet laser light ($h\nu$ between 1.9 eV and 3.9 eV) [9]. These experiments adduced evidence that enlarged MCD signals can be found in 1PPE and raised the question whether MCD asymmetries in near-threshold photoemission could also be found in the multiphoton photoemission regime. The major issue of this section is to demonstrate that MCD also arises in two-photon photoemission (2PPE). The experimental findings are thereby compared to theoretical calculations of the magnetic dichroic response.

4.1.2 Results

Investigated Samples - Heusler alloys

For the detection of MCD in 2PPE processes two Heusler alloys are investigated [51].
Heusler alloys are intermetallic compounds with the stoichiometric composition X_2YZ ordered in an $L2_1$-type structure, many of which are ferromagnetic [52]. A Heusler alloy consists of two different transition metals X and Y and a nonmagnetic metal or nonmetallic element Z. The Y and Z atoms occupy two fcc sublattices with the origins $(0, 0, 0)$ and $(1/2, 1/2, 1/2)$, respectively. The X atoms are located at $(1/4, 1/4, 1/4)$. The investigation of these alloys is interesting from different point of views. Since calculations predicted a 100 % spin polarization directly at the Fermi level for many compositions [53, 54] these species seem to be promising candidates for applications in the field of spintronics [55, 56]. Based on first-principle calculations, it has recently been shown that some Heusler alloys also reveal characteristics of topological insulators [57].
In this work the two full Heusler alloys Ni_2MnGa and Co_2FeSi are investigated. While

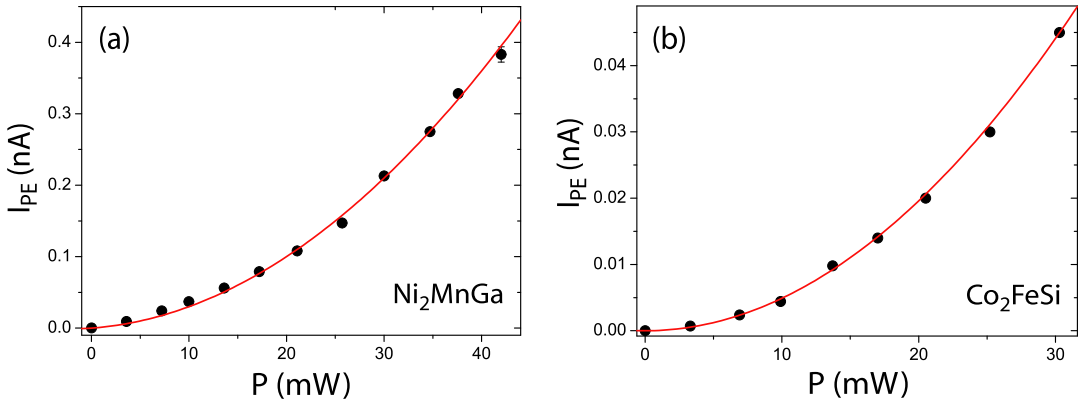

Figure 4.1: (a), (b) Two-photon photoemission as recognized from a quadratic increase of the photoemission current I_e with the laser power P for Ni_2MnGa and Co_2FeSi upon irradiation of the samples with frequency-doubled laser light ($2h\nu = 6.2$ eV).

Co_2FeSi as a halfmetallic ferromagnet is interesting for spintronic applications, Ni_2MnGa is a non-halfmetallic shape memory alloy which is especially important for the development of actuators. The Ni_2MnGa and the Co_2FeSi films with a thickness of 85 nm and 68 nm, respectively, are epitaxially grown on a Al_2O_3(11-20) substrate by dc-sputtering (samples are prepared in the group of Prof. Dr. G. Jakob, University of Mainz). Afterwards both samples are capped by ~ 5 nm Al. For details concerning sample preparation and characterization we refer to Ref. [58] and [59].

Measurements

To firstly ensure that 2PPE is the underlying photoemission process for all MCD measurements the photoemission current I_e is recorded in dependence of the laser power P for both samples at a photon energy of $2h\nu = 6.2$ eV. Fig. 4.1 (a) and (b) depict the expected quadratic behavior. For Co_2FeSi the dependence is almost perfectly quadratic; for Ni_2MnGa it is still reasonably good.
Furthermore, for both samples the work function is determined by means of ultraviolet photoelectron spectroscopy (UPS) to $\Phi = (3.7 \pm 0.2)$ eV for Ni_2MnGa and to $\Phi = (3.3 \pm 0.2)$ eV for Co_2FeSi, respectively. Both arguments, $h\nu < \Phi$ and $I_e \propto P^2$, in conjunction lead to the conclusion that 2PPE is indeed the underlying process for the measured MCD asymmetries.
Since the Heusler alloys are capped, lock-in technique is used for all MCD measurements; the samples are therefore investigated with the experimental setup shown in Fig. 3.3. For a sharp focusing of the incident laser beam which is indispensable for the generation of 2PPE processes the sample is additionally placed in the focal point of a fused silica lens ($f = 15$ mm). However, Eq. (2.33) cannot be directly used to calculate the MCD asymmetry since the photoemission current is converted by the lock-in amplifier to a dc voltage output. For this reason

the photoemission current $I_{\mathrm{e}}^{\pm}$ is translated to a voltage output $U_{\mathrm{e}}^{\pm}$ of the picoamperemeter (i. e. $I_{\mathrm{e}}^{\pm}$ = 1 nA translates to $U_{\mathrm{e}}^{\pm}$ = 1V) which serves as input signal for the lock-in amplifier (c. f. Fig. 3.3). In order to avoid artifacts, e. g. due to sample current drifts, the lock-in output voltage $U_{\mathrm{li}}^{\pm}$ is finally referred to the input signal from the picoamperemeter yielding the ratios $R_{\mathrm{e}}^{\pm} = \frac{U_{\mathrm{li}}^{\pm}}{U_{\mathrm{e}}^{\pm}}$ for both magnetization directions $\vec{M}^{+}$ and $\vec{M}^{-}$, respectively. These ratios already reflect the MCD asymmetry for the respective magnetization direction. The averaged MCD asymmetry for both magnetization directions is given by

$$A = \frac{\bar{R}_{\mathrm{e}}^{+} - \bar{R}_{\mathrm{e}}^{-}}{2}, \tag{4.1}$$

where $\bar{R}_{\mathrm{e}}^{\pm}$ are the averaged values for the corresponding magnetization segments M^{+} and M^{-}. Since the fluctuations in the sample current are small and no periodic current signals are measured (c. f. Fig. 4.2 (d)) it suffices to assume $\bar{U}_{\mathrm{e}} \approx \bar{U}_{\mathrm{e}}^{+} \approx \bar{U}_{\mathrm{e}}^{-}$ in Eq. (4.1) yielding

$$A \approx \frac{\bar{U}_{\mathrm{li}}^{+} - \bar{U}_{\mathrm{li}}^{-}}{2\bar{U}_{\mathrm{e}}}. \tag{4.2}$$

Fig. 4.2 (a) shows an ideal detection sequence of R_{e}. Plotted is R_{e} in dependence of the data points for alternating magnetization direction (i. e. after a certain amount of data is taken the magnetization direction is changed). The photon helicity is, of course, changed periodically with a frequency of $2\omega_{\mathrm{ref}}$ during the whole measurement. MCD is thereby confirmed by an alternating inversion of the signal following an alternating change of the magnetization direction. The blue arrows indicate a simultaneous inversion of both the magnetization direction and the sign of the lock-in output voltage (i. e. a 180° phase shift at the amplifier) which should result in a steadiness of the signal. Fig. 4.2 (b) and (c) depict measurement sequences for the two Heusler alloys at a photon energy of $2h\nu$ = 6.2 eV and a laser power of 25 mW. The signals are not completely symmetric to the base line and do not stay entirely constant when the magnetization and the lock-in output signal are inverted. This behavior might be attributed to a slight false position of the quarter wave plate in the motor holding or to irregularities in the wave plate itself which both cannot be completely avoided. A possibly false position of the quarter wave plate in the motor mount could result in an intensity change of the laser beam oscillating with the same frequency as the measurement signal. Throughout the measurement sequence, the magnetic field is set to a value of $\mu_0 H = \pm 1.05$ T. Using Eq. (4.2) the MCD asymmetry for the Ni_2MnGa sample is determined to $A = (3.5 \pm 0.5) \cdot 10^{-3}$ while for Co_2FeSi it is given by $A = (2.1 \pm 1.0) \cdot 10^{-3}$. Fig. 4.2 (d) depicts the photoemission current $I_e^{\pm}$ averaged over each measurement sequence for both samples. Clearly, no regular alternation is seen as observed in Fig. 4.2 (b) and (c). This demonstrates that an MCD signal cannot be measured without improving the signal-to-noise ratio with lock-in technique. By comparing the photoemission yields shown in Fig. 4.2 (d) and Fig. 4.1 (a) and (b) it should be noted that the size of the laser focus could slightly vary between different measurement series, resulting in a more significant change in the photoemission yield because of the quadratic power dependence.

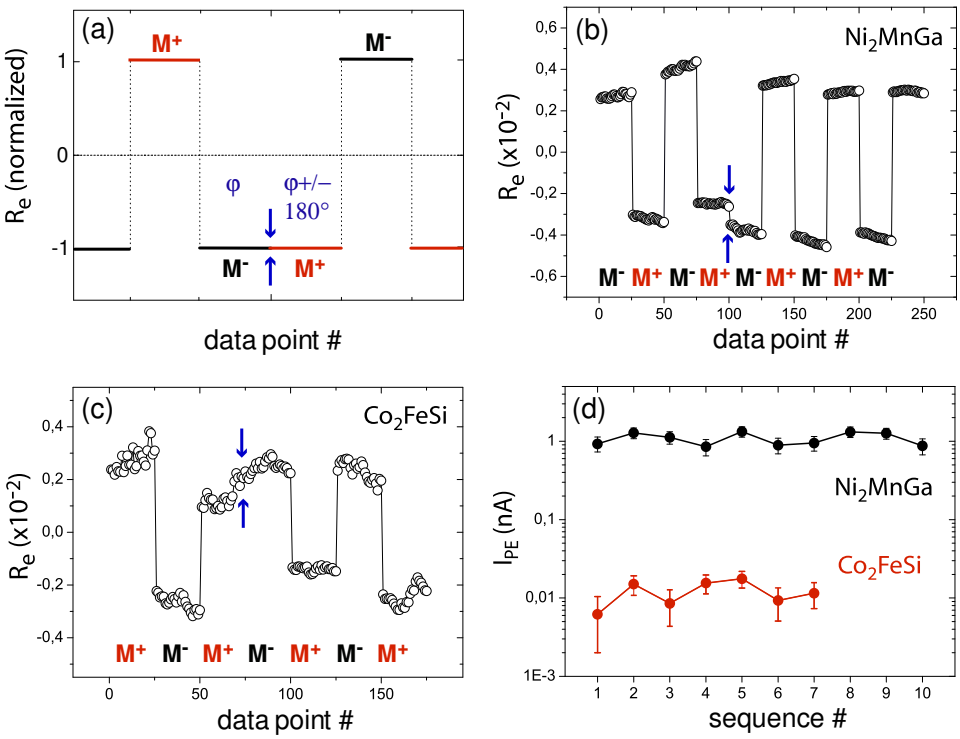

Figure 4.2: (a) Schematic detection sequence of the ratio R_e including alternating magnetization reversals and inversion of both the magnetization direction and the lock-in output voltage ($\varphi \rightarrow \varphi \pm 180°$, arrows). (b) and (c) MCD measurement sequences for the two Heusler alloys Ni_2MnGa and Co_2FeSi at a photon energy of $2h\nu = 6.2$ eV and a laser power of 25 mW. (d) Corresponding averaged photoemission current I_e measured for the magnetization reversal sequences of both samples.

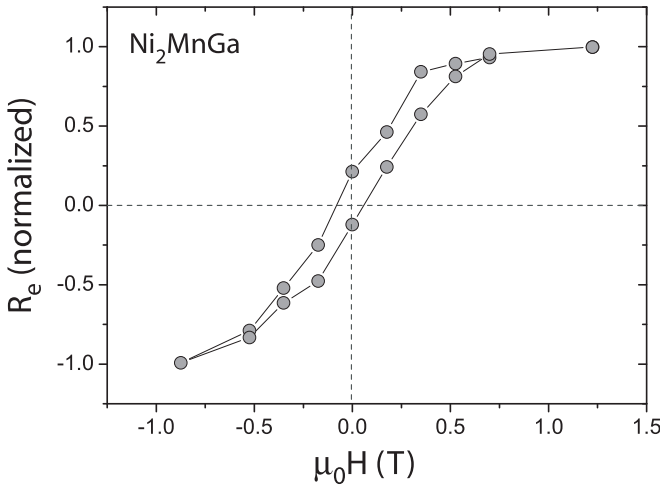

Figure 4.3: Hysteresis loop for Ni_2MnGa with non-vanishing coercive field obtained from the MCD asymmetry in two-photon photoemission.

For further demonstration of the magnetic dichroism, the magnetization curve of Ni_2MnGa obtained from the 2PPE magnetic circular dichroism is shown in Fig. 4.3. In order to improve the signal-to-noise ratio, the data are averaged over 200 cycles for each given magnetic field $\mu_0 H$. The resulting magnetization loop is normalized to one. The record of the full magnetization cycle starts at a maximum magnetic field of $\mu_0 H = 1.25$ T. Fig. 4.3 displays the hysteresis loop from which a coercive field of $+\mu_0 H_c = 0.06$ T (-$\mu_0 H_c = 0.08$ T) is extracted. The saturation field is determined to $\mu_0 H_s = 0.52$ T. The non-vanishing magnetic remanence indicates that the easy axis of the Ni_2MnGa film lies not completely within the film plane.

4.1.3 Discussion

To investigate the origin of the observed 2PPE MCD asymmetry *ab initio* calculations of the magnetic dichroic response are performed. For photon-in photon-out magnetic dichroic experiments such as the magneto-optical Kerr effect, the appropriate theoretical description is provided by linear-response theory in single-particle formulation in combination with relativistic energy-band theory. Energy-band theory is needed to determine the allowed interband transitions and to calculate their transition matrix elements which define the optical conductivity tensor. Linear response theory is used to finally calculate the optical conductivity from which the dichroic response is obtained. In this approach, all allowed interband transitions connecting initial and final band states in the whole Brillouin zone are considered and the dichroic signal is obtained by averaging over all contributions in all k-directions. Ch. 2.3 explains the theoretical foundations of this method. Moreover, it demonstrates how the MCD effect can be simulated by transferring the scenario to our photon-in/electron-out setup. In this modified approach, we look for interband transitions in all crystallographic directions

obeying the Einstein equation for photoemission ($2h\nu > \Phi$) and the relativistic dipole selection rules and calculate the asymmetry for all contributing interband transitions. Therefore, our co-workers (Prof. Oppeneer and Dr. Tarafder, University of Uppsala, Sweden) use an appropriately modified version of the code for the calculation of the conductivity tensor σ and the dielectric tensor ϵ as reported in Ref. [44], respectively. As no *ab initio* theory for 2PPE MCD is available as yet, we now briefly discuss two models.
In the first one, the non-equilibrium electron population that is caused by the first laser pulse (see Ref. [60]) is *ab initio* calculated. Subsequently, the dielectric tensor for the second laser pulse is computed, using the non-equilibrium band occupations created by the first pulse. Proper transition selection rules are taken into account for the second excitation and to a good approximation for the first one [60]. In this model, there is no "remembrance" of the initial state for the second $h\nu$ excitation.
In the second model, we assume instantaneous, coherent absorption of two photons, and consider only those transitions which are possible within such an instantaneous process, starting with one $h\nu$ excitation to a virtual state below the vacuum level E_V and with the immediate second $h\nu$ excitation to a state above E_V. In this approach, initial and final states of the $2h\nu$ excitation are coupled by appropriate transition matrix elements.
The calculations of the magnetic dichroic response reveal that the MCD attained from the first model is more than 1 order of magnitude smaller than that of the second one. This motivates to the assumption that the dominating contribution stems from excitations that occur through the practically instantaneous absorption of two photons in accordance with the second model. Fig. 4.4 (a) depicts computed 2PPE MCD spectra of Ni_2MnGa and Co_2FeSi as a function of the photon energy $2h\nu$ at fixed work function Φ [61]. Thereby, the asymmetry values have been calculated following Eq. (2.54). The experimental data points are also shown. For the *ab initio* calculations of both Heusler alloys the $L2_1$ structure with lattice parameters of 5.83 and 5.65 nm, respectively, is used. The calculations of the 2PPE MCD spectra are performed for two different escape depths, 5 and 20 nm, and two different lifetime parameters, $\tau^{-1} = 0.68$ and 0.95 eV. The values for the escape depth span the experimentally determined probing depth of threshold photoemission microscopy [62]. Gratifyingly, we find the dependence of the 2PPE MCD asymmetry on the escape depth d to be very weak. We point out that for Ni_2MnGa a work function of 3.5 eV is used. The experimentally determined value of 3.7 eV only shifts the spectrum slightly towards higher photon energies. The agreement between theory and experiment can nonetheless be considered as reasonably good. This exemplifies that the intrinsic origin of the observed 2PPE MCD is caused by the spin and orbitally polarized electronic structure of the ferromagnetic material. The presence of both spin splitting and orbital magnetic splitting, due to exchange interaction and spin-orbit interaction, respectively is required to provide a nonzero magnetic dichroic signal using photons as probe [38]. The same obviously holds here for photoelectrons as probe. The finding that the experimental MCD asymmetry is smaller than the theoretical prediction could be attributed to the Al-capping layer, which is not considered in the calculations. It absorbs part of the photoelectrons and contributes to the photoemission signal with Al-photoelectrons carrying no MCD information. This will reduce the measured MCD asymmetry as discussed in Ch. 4.2. Finally, we note

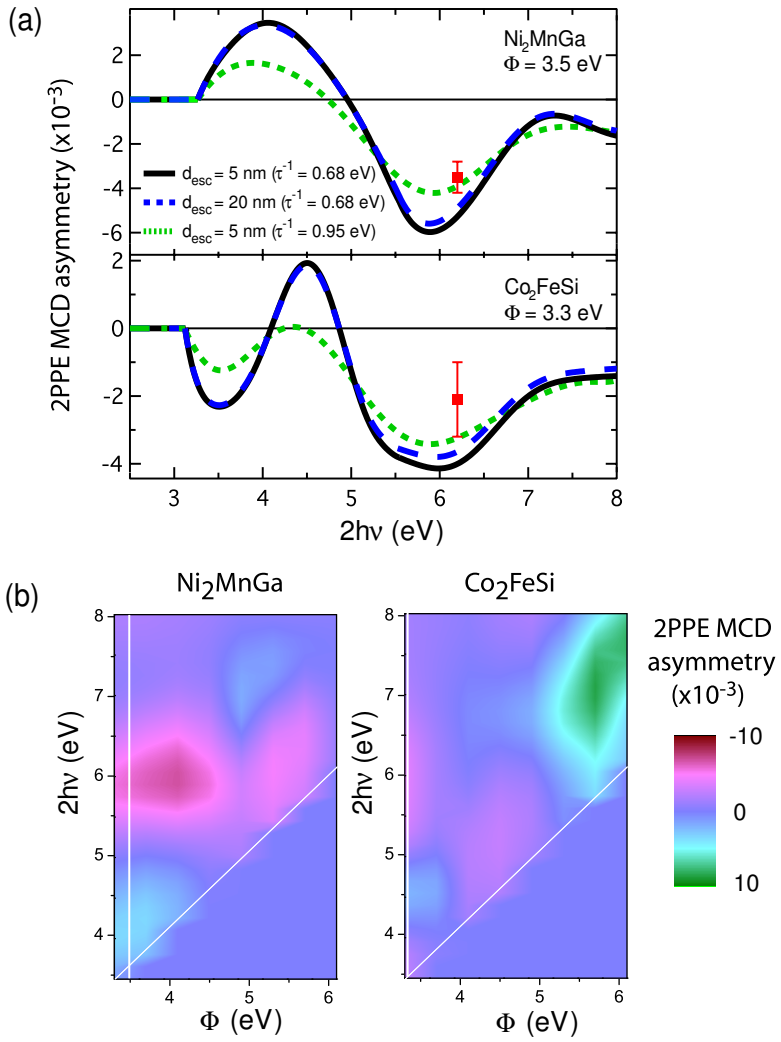

Figure 4.4: (a) Calculated 2PPE MCD asymmetry spectra for Ni_2MnGa and Co_2FeSi in dependence of the photon energy [61]. The spectra are calculated for two different escape depths and lifetime parameters; the experimental data points are shown as squares. (b) Two-dimensional representation of the *ab initio* predicted 2PPE MCD for Ni_2MnGa and Co_2FeSi as a function of $2h\nu$ and the work function Φ. The diagonal white lines indicate the boundary $2h\nu - \Phi = 0$ below which the MCD signal vanishes; the vertical white lines indicate MCD spectra shown with dotted lines in (a).

that the calculations predict an interesting difference in the MCD asymmetry of Ni_2MnGa and Co_2FeSi for 2hν between 3 and 5 eV: in contrast to Ni_2MnGa, the MCD asymmetry of Co_2FeSi exhibits a change of sign despite of their structural similarity. Fig. 4.4 (b) depicts a two-dimensional representation of the 2PPE MCD asymmetry in dependence of 2hν and Φ for both samples. Beneath the diagonal white lines photoemission is not possible. The vertical white lines reflect the MCD spectra shown as dotted curves in Fig. 4.4 (a). In agreement with (a), the 2PPE response differs for both samples. As an example, for Ni_2MnGa asymmetries around -8 $\%$ are predicted at (2hν,Φ) $\approx$ (6 eV,4 eV) while the MCD asymmetry for Co_2FeSi is expected to be much smaller ($\sim$ -2 $\%$) at the same parameters. Another important result is that the simulations for both samples predict the MCD signal to depend on 2hν and Φ separately.

4.1.4 Summary and conclusions

Magnetic circular dichroism in two-photon photoemission has been demonstrated for two ferromagnetic Heusler alloys ($A_{2\mathrm{PPE}} = (3.5 \pm 0.5) \cdot 10^{-3}$ for Ni_2MnGa and $A_{2\mathrm{PPE}} = (2.1 \pm 1.0) \cdot 10^{-3}$ for Co_2FeSi). The used theoretical explanation on basis of relativistic energy-band theory in combination with linear-response theory is in reasonable agreement with the measurement. Transferring this photon-in/photon-out approach as commonly used for the magneto-optical Kerr effect to our photon-in/electron-out setup therefore seems to be an adequate method to calculate MCD asymmetries. In this sense, it also demonstrates that the origin of the 2PPE MCD is born out of modifications of the energy bands caused by exchange and spin-orbit interactions. This means that the simultaneous occurrence of both effects, exchange splitting and spin-orbit coupling, give rise to magnetic circular dichroism.
Unlike the results shown in Ch. 4.3, here the 2PPE process is modeled as an instantaneous, coherent two step process. In Ch. 4.3 we will see that for a Co/Pt system the picture of a sequence of two independent processes might be more adequate for the description of 2PPE.
Energy-dependent measurements could furthermore depict the behavior of MCD asymmetries in dependence of the photon energy. This would enable a much stronger comparison between experimental and theoretical results than given in Fig. 4.4 (a). For energy-dependent measurements it might be helpful to use sample systems with a more manageable band structure compared to those of the Heusler alloys to possibly identify measured asymmetries with only few band to band transitions. Since the MCD signal is predicted to depend independently on the photon energy and the sample work function it would be worthwhile to compare energy-dependent measurements with those at low work-function values.
Finally, with respect to applications, i.e. in photoemission electron microscopy, ferromagnetic thin films exhibiting larger asymmetries exceeding the low-percentage range are needed. Fig. 4.4 foreshadows that beside the choice of a suitable material also the parameters of photon energy and sample work function strongly decide about the magnitude of MCD asymmetries.

4.2 Near-threshold MCD at the spin-reorientation transition of ultrathin epitaxial Pt/Co/Pt(111)/W(110) films

4.2.1 Motivation

First measurements in the regime of near-threshold photoemission revealed magnetic circular dichroism to exist in one as well as in two-photon photoemission processes. Thereby, dichroic signals have been measured in the range of the detection limit, where asymmetry values did not exceed the low-percentage range [8, 61, 62]. Only recently, much larger values have been reported [9, 63, 64, 65, 66]: a study on a perpendicularly magnetized 12 ML Ni film on Cu(001) revealed MCD asymmetries larger than 10 % in threshold photoemission, where the photon energy just exceeds the sample work function [9]. This is remarkable since MCD in the visible-light region suffers from the absence of discrete atomic levels with a high spin-orbit coupling as it is the case in XMCD measurements. Besides Ni(001), there is still only little knowledge about thin-film systems revealing large MCD asymmetries in near-threshold photoemission. Also general properties of the asymmetry in one- or multi-photon photoemission processes have up to now scarcely been investigated. For example, there is only little information about the behavior of asymmetries in dependence of the magnetic anisotropy, the sample thickness or capping layers.
Concerning the sample thickness Nakagawa and Yokoyama observed a drastic change of the MCD asymmetry as a function of the thickness of a wedged Ni film grown on Cu(001) [9] in near-threshold photoemission.The in-plane magnetized film thicknesses up to the spin-reorientation transition (SRT) at 8 ML showed asymmetry values in a longitudinal setup that are one order of magnitude smaller than the ones for the out-of-plane magnetized regions, starting from 8 ML in a polar setup. As magnetic circular dichroism belongs to the magneto-optical phenomena [9, 67] this behavior corresponds to similar differences between the longitudinal and polar Kerr effect, crossing the SRT with increasing sample thickness. The measurements on Ni, however, raise the question whether the MCD asymmetry of a completely saturated sample increases continuously from the ultrathin end of the wedge up to higher thicknesses, indicating that surface effects do not play a dominant role. Otherwise a saturation of the MCD asymmetry at a few ML of the magnetic film should be observed. Another question is whether the MCD asymmetry is influenced by the orientation of the magnetization easy axis.
In this section we present magneto-optical Kerr (MOKE)- and near-threshold MCD measurements on a Pt-capped, wedged Co sample grown on Pt(111)/W(110) to investigate the influence of magnetic anisotropy and sample thickness in one-photon and two-photon photoemission. Since both the exchange splitting and the spin-orbit coupling are preconditions for the appearance of magneto-optical effects the combination of ferromagnetic Co and Pt with a high nuclear charge Z is promising for enhanced MCD asymmetries [68]. The measured MCD signals are compared with measured polar Kerr ellipticities in the framework of the Jones formalism. In addition, a comparison with calculated Kerr signals is provided by simulations of medium boundary and medium propagation matrices. As MCD and MOKE are based on the

same microscopic mechanisms the relation between both effects is thus investigated.

4.2.2 Sample preparation

At first a Pt buffer layer is prepared on a W(110) single crystal. Since the lattice mismatch between both elements (a_{W} = 0.316 nm, a_{Pt} = 0.392 nm) is only 1.1 %, this is an adequate alternative to a Pt single crystal [1]. The initial growth of Pt on W(110) has been studied by Bauer et al. [69]. The given ratios of the lattice constants lead to the Kurdjumov-Sachs growth mode showing two slightly rotated domains (for details see Ref. [70]). For both domains the (111)-axis is oriented perpendicular to the surface. For the following experiment the azimuthal angle plays no role.
Before deposition of Co and Pt, the W(110) crystal is cleaned by repeated cycles of flashing (P_{heating} = 200 W, 1-2 s) and annealing ($P_{\mathrm{heating}} \sim$ 40 W, 30 min, $\sim$ 1200°C) in oxygen atmosphere (p = $4{\cdot}10^{-8}$ mbar). A 20 monolayers (ML) Pt(111) buffer is evaporated afterwards on the substrate ($U_{\mathrm{HV}} \cdot I_{\mathrm{emission}}$ = 44 W, evaporation rate 256 s/ML) at a pressure of $7{\cdot}10^{-9}$ mbar. After annealing (12 min, 800°C) the Co wedge is deposited at a pressure of $4{\cdot}10^{-10}$ mbar ($U_{\mathrm{HV}} \cdot I_{\mathrm{emission}}$ = 13 W, evaporation rate 32 s/ML) by withdrawing a shutter located between the Co evaporator and the sample. The thickness along the wedge is regulated by a quartz thickness monitor. A wedge of 0-16 ML with a monolayer width of 200 μm is produced. Since the formation of a Co/Pt alloy at the interface should result in increased magneto-optical signals [71, 72] the sample is subsequently annealed for 11 minutes at a temperature of 410 °C. MCD measurements are performed with the experimental setup shown in Fig. 3.3. Therefore, the structure is completed with a 15 ML thick Pt capping (the evaporation parameters are identical to the ones for the Pt buffer layer) deposited at room temperature to prevent the Co film from oxidation. The quality of the substrate surface and the epitaxial films is controlled by low energy electron diffraction (LEED). Fig. 4.5 (a) - (c) depicts a set of LEED images for different preparation steps; a sketch of the prepared sample system is shown in Fig. 4.5 (d). Fig. 4.5 (a) depicts the first Brillouin zone (BZ) of the bcc W(110)-crystal at an electron energy of 73.3 eV. Small and bright spots reflect a clean, high-quality substrate surface. In Fig. 4.5 (b) the first BZ of the annealed fcc Pt-buffer is shown at an electron energy of 74.1 eV. The typical sixfold structure can be clearly seen. The layer is annealed directly after evaporation to improve the film structure; due to local defects and surface roughness the Pt spots appear slightly broadened and less sharp compared to the W(110)-substrate. Fig. 4.5 (c) shows the first BZ of the non-annealed fcc Co-wedge at 76.5 eV. Since the lattice constant of Co (a_{Co}=0.355 nm) is smaller than the one of Pt and the LEED technique displays the reciprocal space the distance between neighboring spots is slightly increased. The azimuthal orientation of Co and Pt is obviously identical.

[1] The lattice mismatch is derived from the nearest neighbour distance between the atoms in the corresponding lattice by $l_{\mathrm{mis}} = \frac{d_{\mathrm{NN,(substrate)}} - \mathrm{d_{NN}(film)}}{d_{\mathrm{NN}}(\mathrm{substrate})}$.

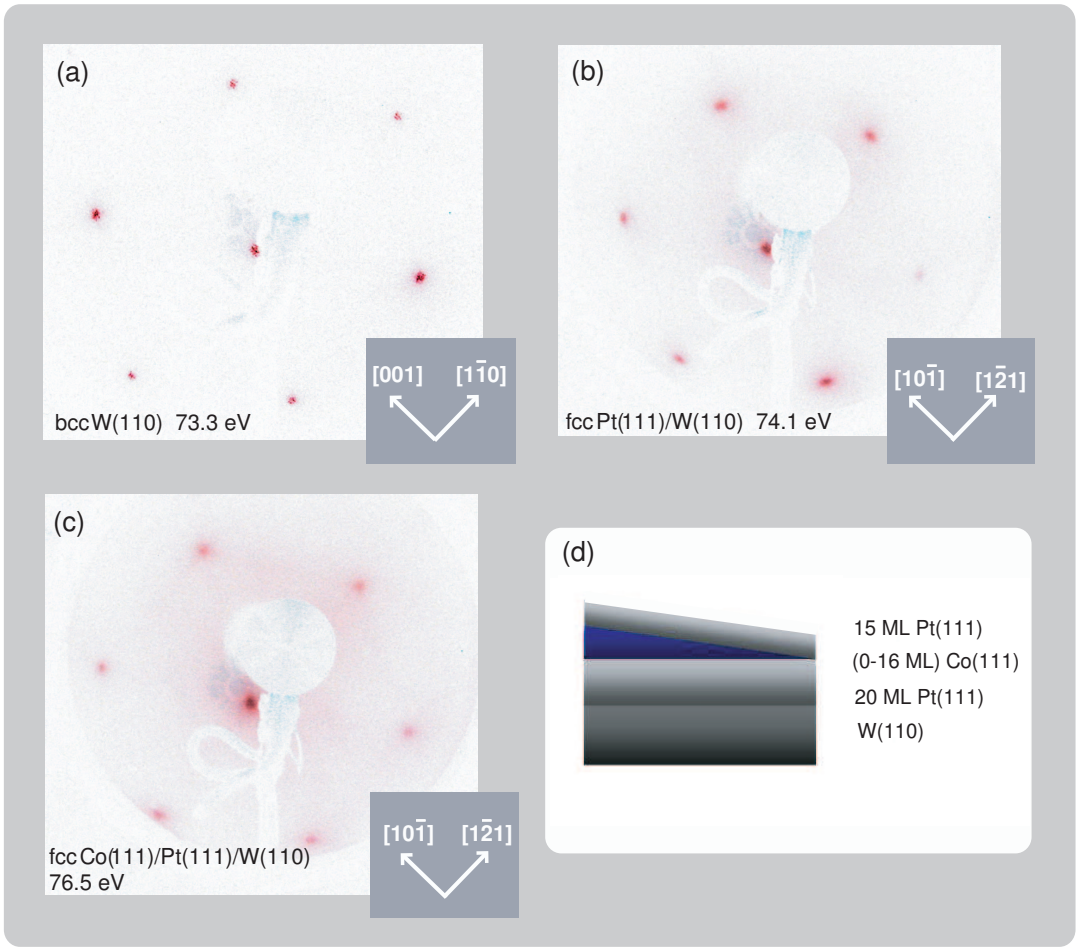

Figure 4.5: Set of LEED patterns. (a) bcc W(110) (single crystal) at a scattering energy of 73.3 eV. (b) 20 ML Pt(111)/W(110) at 74.1 eV (annealed after deposition of Pt). (c) fcc Co(111) wedge/20 ML of fcc Pt(111)/W(110) at 76.5 eV. (d) sketch of the prepared sample system.

4.2.3 Results

Kerr measurements

In order to determine the magnetic features of the wedged sample, Kerr measurements are carried out outside the vacuum in the polar and the longitudinal setup. Polar Kerr measurements are performed almost under normal incidence ($\sim 5°$), while in the longitudinal setup s-polarized light with an incidence angle of $\sim 45°$ is used. Thickness-dependent Kerr measurements in the polar geometry are carried out with an external magnetic field of $\mu_0 H$ = 255 mT; in the longitudinal geometry a field of 178 mT is used. The focused 670 nm laser beam allows for a lateral resolution corresponding to 1 ML thickness increase on the Co wedge. The complex Kerr angle,

$$\phi_{\mathrm{K}} \equiv \theta_{\mathrm{K}} + i\epsilon_{\mathrm{K}} \tag{4.3}$$

consists of the Kerr rotation angle θ_{K} and the Kerr ellipticity ϵ_{K}. Referring to Ref. [73, 74, 75], an approximated formula for the thickness dependence of ϕ_{K} for a capped magnetic film of thickness t on a substrate S is given by:

$$\phi_{\mathrm{K}} \approx \frac{i\sigma_{xy}}{\sigma_{xx}^{S}} \frac{4\pi t}{\lambda}. \tag{4.4}$$

σ_{xx}^{S} is the diagonal element of the optical conductivity tensor of the substrate, σ_{xy} is the off-diagonal element of the optical conductivity tensor of the investigated magnetic film and λ is the vacuum wavelength. This expression holds in the case of the polar Kerr effect and is valid for $t << \lambda$. Eq. (4.4) also applies to our sample system considering the negligible influence of the W(110) substrate due to the thick Pt buffer layer. Consequently, one would expect a linear increase of both the Kerr rotation angle and the Kerr ellipticity with increasing thickness of the Co wedge. The measured values of the polar (dots) and longitudinal Kerr rotation (squares) are shown in Fig. 4.6 (a). The polar Kerr rotation angle θ_{K} shows a steady increase up to 6.5 ML. At 5.5 ML the easy magnetization direction starts to change from an out-of-plane to an in-plane orientation due to the increasing shape anisotropy (c. f. also Fig. 4.7). At 6.5-7 ML a maximum Kerr rotation of 16.05 m$^\circ$ is reached followed by a continuous decrease, since the external field does not suffice to saturate the sample magnetization in the out-of-plane direction. At the ultrathin end of the wedge the polar Kerr rotation curve exhibits a steep slope followed by a weaker increase for Co thicknesses exceeding 4 ML. Following Ref. [76] these linear sections with different slopes might be attributed to a structural transition from fcc(111) to hcp(0001) Co with increasing sample thickness. In Ref. [76] the crystalline transformation was detected almost in the same thickness region, where fcc(111) Co was observed at thicknesses of $d < 5$ ML and passed into hcp(0001) Co for thicknesses $d > 6$ ML. Concerning the critical thickness of the spin-reorientation transition a broad range of values from 4.4 ML [77] to 12 ML [78] is reported in the literature; a theoretical investigation predicts a transition at 4 ML [79]. To explain this discrepancy between the experimental and theoretical results it was demonstrated [80] that the substrate roughness affects the critical thickness of the SRT attributing an early reorientation transition to a rough substrate. In our case the Co wedge is

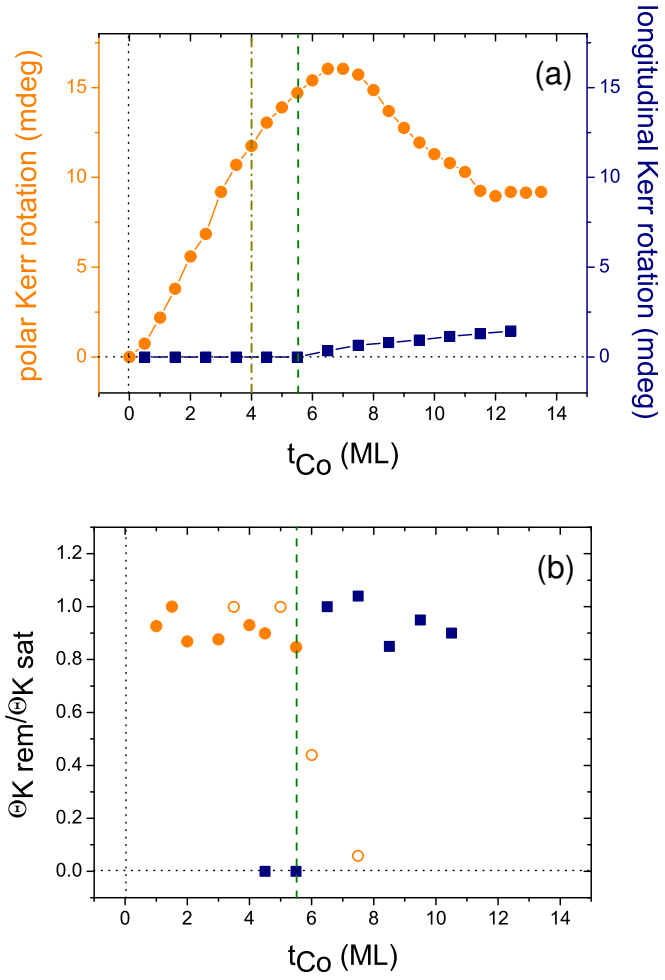

Figure 4.6: (a) Polar (dots) and longitudinal Kerr rotation angle (squares) in dependence of the Co thickness measured at external fields of 255 mT (polar setup) or 178 mT (longitudinal setup). The onset of the assumed structural transition from fcc(111) Co to hcp(0001) Co according to Ref. [76] is marked with a dashed-dotted line, the spin-reorientation transition is marked with a dashed line. The error bars are in the order of the symbol size. (b) Squareness $\frac{\theta_{\mathrm{K,rem}}}{\theta_{\mathrm{K,sat}}}$ in dependence of the Co thickness for the polar (dots) and longitudinal Kerr setup (squares). The open circles correspond to data from Fig. 4.7 measured with higher accuracy.

evaporated on a 20 ML Pt buffer, which might be rougher than a Pt single crystal surface. This could be a reason for the SRT occurring at a relatively low Co thickness of 5.5 ML.
In earlier reports a non-vanishing Kerr rotation extrapolated to zero ML Co thickness was observed and related to a polarization of Pt by neighboring Co atoms [81]. Our results in Fig. 4.6 (a), however, show that the polar Kerr rotation increases linearly with the thickness

at the ultrathin end of the wedge. There is no positive offset leading to a non-zero extrapolated Kerr rotation in agreement with Ref. [78]. Considering that interface contributions may depend sensitively on the interface morphology [82] the extrapolated offset cannot be taken as a measure for the Pt polarization, which is certainly present. In accordance with the polar Kerr measurement the longitudinal Kerr rotation (squares) is equal to zero up to 5.5 ML Co thickness, where it starts to increase almost linearly with the sample thickness. Apparently, the longitudinal Kerr effect also reveals a linear thickness dependence as stated in Eq. (4.4) for the polar case. While in the polar setup easy axis curves are observed until a thickness of 5.5 ML, the in-plane magnetization loops show a square behavior starting from 6.5 ML. This means that the SRT takes place between 5.5 ML and 6.5 ML [83] (c. f. also Fig. 4.7).
To confirm the position of the SRT not only by the saturation values of the Kerr rotation, the squareness $\frac{\theta_{\mathrm{K,rem}}}{\theta_{\mathrm{K,sat}}}$ is plotted in dependence of the sample thickness (see Fig. 4.6 (b)). $\theta_{\mathrm{K,rem}}$ is the remanent value, while $\theta_{\mathrm{K,sat}}$ describes the saturation value of the Kerr rotation θ_{K}. According to the observation of an easy axis magnetization curve the squareness in the polar case (dots) is ~ 1 until the beginning of the SRT is reached at 5.5 ML. Subsequently, it drops rapidly, since the intrinsic magnetization direction changes to an in-plane configuration. For the in-plane geometry the squareness (squares) is also ~ 1 in the region above 5.5 ML and 0 beyond it.
Fig. 4.7 depicts a set of hysteresis loops for selected Co layer thicknesses measured at a maximum applied field of $\pm$ 51 mT clearly demonstrating the transition from an easy axis magnetization curve at 3.5 ML to an in-plane configuration of the magnetization vector at 7.5 ML in the polar Kerr setup.

MCD measurements in near-threshold photoemission

MCD measurements in near-threshold photoemission are carried out in one-photon photoemission (frequency-tripled laser light, hν = 4.64 eV) as well as in two-photon photoemission (frequency-doubled laser light, hν = 3.10 eV). To enable 2PPE processes the sample is additionally placed in the focal point of a lens (f = 15 mm). At the same time this allows a monolayer-thickness sensitive detection of the MCD asymmetry. To ensure that in the case of 4.64 eV the excitation process is governed by one-photon photoemission, the linear dependence of the photoelectron current on the laser power is checked, simultaneously revealing that the value for the sample work function is $<$ 4.64 eV. In the case of 3.1 eV a quadratic behavior is measured indicating 2PPE processes (c. f. also Ch. 4.1). By means of UPS the sample work function is determined to $\Phi = (4.6 \pm 0.2)$ eV.
MCD measurements are performed with the experimental setup shown in Fig. 3.3. Fig. 4.8 gives an example of a measurement sequence of the 2PPE MCD signal for the Co wedge. MCD is confirmed by periodic changes of the MCD signal following periodic changes in the orientation of the magnetization $\vec{M}^{+}$ and $\vec{M}^{-}$ parallel or antiparallel to the laser beam. In this sense Fig. 4.8 verifies magnetic circular dichroism. The steadiness of the signal at a simultaneous change of the magnetization direction and the sign of the lock-in output voltage (blue arrow) approves the good performance of the lock-in amplifier. MCD asymmetries are

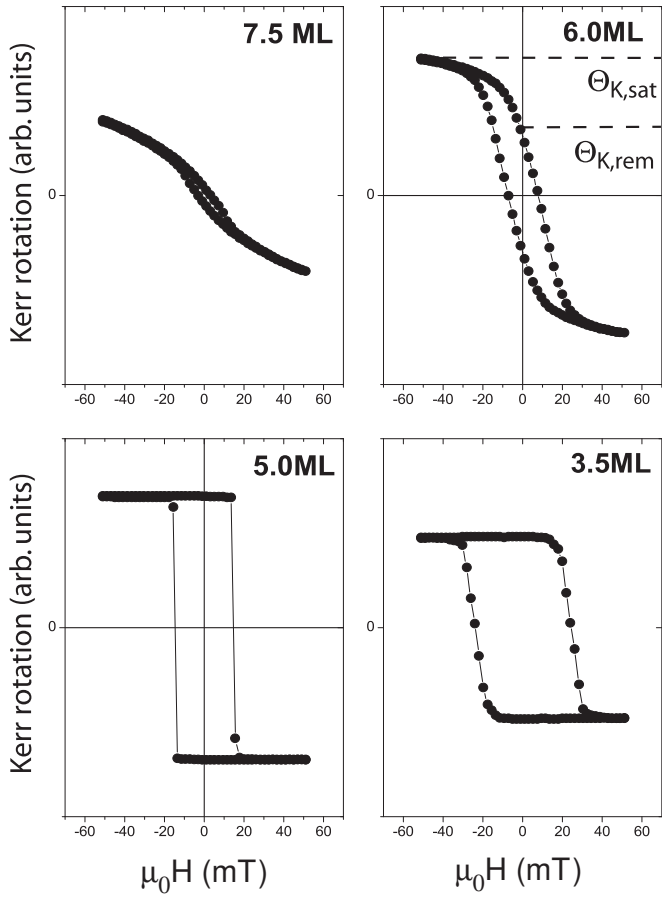

Figure 4.7: Hysteresis loops for selected Co layer thicknesses measured at a maximum applied field of ± 51 mT in the polar Kerr setup. $\theta_{\mathrm{K,sat}}$ and $\theta_{\mathrm{K,rem}}$ are indicated exemplarily for one curve.

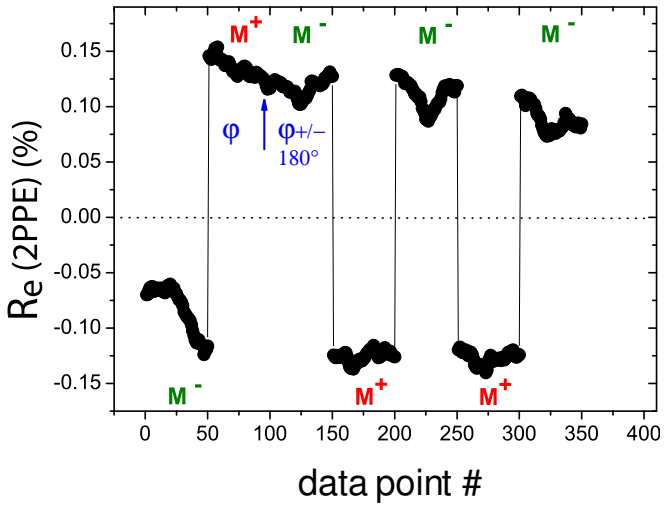

Figure 4.8: Measurement sequence for verification of MCD in near-threshold photoemission based on periodic changes of the MCD signal upon periodic reversals of the magnetization direction $\vec{M}^{\pm}$. The arrow marks a simultaneous inversion of the magnetization direction and the phase setting at the lock-in amplifier ($\varphi \rightarrow \varphi \pm 180°$) resulting in a constant MCD signal.

calculated according to Eq. (4.2) in Ch. 4.1.
During 2PPE measurements with 3.1 eV photon energy the average laser power is 44 mW. To ensure that the thickness region with an out-of-plane magnetization is saturated on the one hand and to guarantee that the 2PPE laser spot is stable in position during the reversal of the external field on the other hand, the magnetic field is set to an intermediate value of 222 mT.
Fig. 4.9 (a) depicts a thickness-dependent 2PPE MCD measurement in near-threshold photoemission, revealing a linear increase of the asymmetry with increasing Co thickness. At 6.5 ML a value of 0.14 % is recorded. As demonstrated with the Kerr data, the magnetization easy axis at 6.5 ML has changed from the out-of-plane to an in-plane direction. Obviously, an influence of the magnetization easy axis on the magnitude of the asymmetry cannot be detected as the signal increases continuously. The linear increase of the asymmetry indicates that surface effects do not play a crucial role. Otherwise a saturation of the asymmetry within the first monolayers of the wedge would have be expected. Therefore, the asymmetry must be dominated by the Co bulk properties.
Results for the 1PPE MCD measurement in near-threshold photoemission are shown in Fig. 4.9 (b). The asymmetry is measured with an external magnetic field of 0.74 T. For the 1PPE measurement we would use a larger field than in the case of 2PPE because the photoemission intensity for 1PPE is much less sensitive to small sample displacements. At 4.64 eV the laser power is set to 1.4 mW. The asymmetry also increases monotonously with increasing Co thickness. However, the behavior of the asymmetry is not only influenced by the film thickness. In contrast to the 2PPE measurements one-photon photoemission exhibits three distinct regions

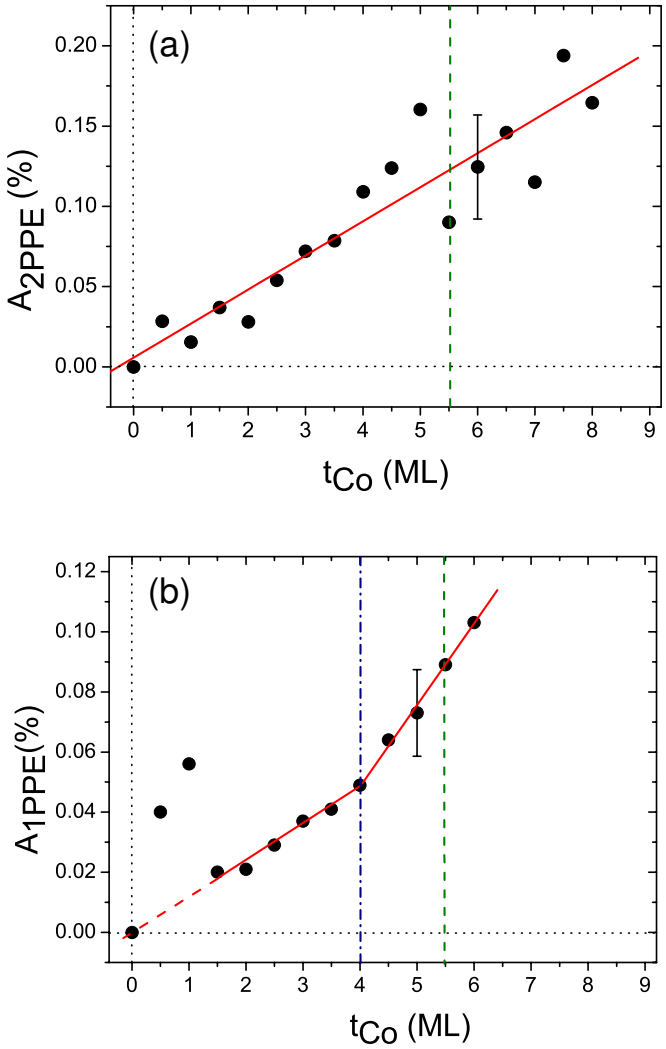

Figure 4.9: (a) 2PPE MCD asymmetry in near-threshold photoemission in dependence of the Co thickness measured at an external field of 222 mT. (b) Same for 1PPE at an external field of 0.74 T. The onset of the assumed structural transition between fcc(111) Co and hcp(0001) Co is marked with a dashed-dotted line, the SRT is marked with a dashed line. The photon energies used for 2PPE and 1PPE are 3.1 eV and 4.64 eV, respectively. All MCD measurements are carried out in the polar geometry. Error bars are derived for a chosen monolayer thickness.

of near-threshold MCD: at low Co coverages up to ∼1.5 ML an enhanced dichroic signal is observed which is followed by a linear increase up to ∼ 4 ML. Here, a discontinuity occurs beyond which a steeper linear increase of the MCD signal is measured. At 6 ML the asymmetry reaches 0.1 %. It is interesting to note that the strong signal increase at lowest Co coverages is seen exclusively in 1PPE but not in 2PPE. At these low coverages nanomagnetism due to Co island growth is prevailing and could influence the magneto-optical properties and lead to a much stronger wavelength dependence. Furthermore, the 2D band structure of a monolayer Co on Pt could be favorable for a high MCD effect. The 2D band structure of a monolayer shows no dispersion along the surface normal and at the Γ-point atomic-like behavior prevails. Both could favor a high MCD. However, further measurements are needed to validate these assumptions.
The transition between the linear regions with different slopes occurs at ∼ 4 ML and might be attributed to the structural change from fcc(111) to hcp(0001) Co already discussed in the context of the Kerr measurements (see Fig. 4.6(a)). Since this structural change does not show up in the 2PPE measurements, 1PPE seems to be more sensitive to band structure changes conditional upon changes in the crystal structure.

4.2.4 Discussion

As mentioned above, magnetic circular dichroism belongs to the magneto-optical phenomena. In Ch. 4.1 we have already used linear response theory in combination with energy band calculations to theoretically describe MCD in strong analogy to the magneto-optical Kerr effect. Now the question might rise whether an easier and handy theoretical approach to MCD asymmetries without the use of highly elaborated mathematical codes can be given by a direct connection to the magneto-optical Kerr quantities. Using the Jones formalism [2] a relation between the MCD asymmetry A_{MCD} and the Kerr ellipticity ϵ_{K} can be found,

$$A_{\mathrm{MCD}} \cong 2\epsilon_{\mathrm{K}} \left(\frac{R}{1-R} \right), \tag{4.5}$$

where R is the reflectivity of the investigated sample at the given wavelength. In the following we recapitulate the derivation of Eq. (4.5), which has originally been given in Ref. [67]. Assuming circularly polarized, normally incident laser light the influence of a magnetic sample

[2] The Jones matrix formalism describes the influence of an optical component on a electromagnetic plane wave. The electric field of the monochromatic wave is thereby expressed by the so-called Jones vector. The optical components, e. g. polarizers, quarter wave plates, reflecting surfaces, are described by matrices. The influence of an optical component on the incoming polarized radiation is finally obtained by matrix multiplication [84] yielding

$$\vec{E}' = T\vec{E} \quad \text{or} \quad \begin{pmatrix} E'_p \\ E'_s \end{pmatrix} = \begin{pmatrix} T_{pp} & T_{ps} \\ T_{sp} & T_{ss} \end{pmatrix} \begin{pmatrix} E_p \\ E_s \end{pmatrix},$$

where $\vec{E}$ and $\vec{E}'$ are the Jones vectors of the electric field before and after passing the optical component, respectively. T is the Jones matrix for the optical component. For further information concerning this formalism we refer to Ref. [84].

causing a polarization change in the reflected beam due to the magneto-optical Kerr effect is described by the corresponding reflection matrix. The reflection matrix for the polar magneto-optical Kerr effect is derived within the Jones matrix formalism [84] and changes the electric field vector $\vec{E}_{\sigma^\pm} = (E_x, E_y) = (1, \pm i)\,\hat{e}$ to

$$\begin{pmatrix} E'_x \\ E'_y \end{pmatrix} = \begin{pmatrix} 1 & \phi_\mathrm{K} \\ \phi_\mathrm{K} & -1 \end{pmatrix} \begin{pmatrix} E_x \\ E_y \end{pmatrix}, \tag{4.6}$$

where ϕ_K is the complex Kerr angle. Then the asymmetry for the reflected light is given by:

$$A_\mathrm{K} = \frac{\left|\vec{E}'_{\sigma^+}\right|^2 - \left|\vec{E}'_{\sigma^-}\right|^2}{\left|\vec{E}'_{\sigma^+}\right|^2 + \left|\vec{E}'_{\sigma^-}\right|^2} = \frac{-2\epsilon_\mathrm{K}}{1 + \left|\phi_\mathrm{K}\right|^2} \approx -2\epsilon_\mathrm{K} \tag{4.7}$$

for $\left|\phi_\mathrm{K}\right|^2 << 1$. This expression for the asymmetry in reflection involving the reflected light intensity I_R can be directly related to the asymmetry in absorption involving the absorbed light intensity $I_\mathrm{A} = I_0 - I_\mathrm{R}$ by writing A_K in terms of the absorbed intensity I_A:

$$A_\mathrm{K} \cong \frac{I_{\mathrm{R},\sigma^+} - I_{\mathrm{R},\sigma^-}}{2I_\mathrm{R}} = -\frac{I_{\mathrm{A},\sigma^+} - I_{\mathrm{A},\sigma^-}}{2I_\mathrm{R}}, \tag{4.8}$$

assuming $I_{\mathrm{R},\sigma^+} \approx I_{\mathrm{R},\sigma^-} \approx I_\mathrm{R}$.
With the asymmetry in absorption defined as

$$A_\mathrm{A} := \frac{I_{\mathrm{A},\sigma^+} - I_{\mathrm{A},\sigma^-}}{2I_\mathrm{A}}. \tag{4.9}$$

where we have also assumed $I_{\mathrm{A},\sigma^+} \approx I_{\mathrm{A},\sigma^-} \approx I_\mathrm{A}$, we find

$$A_\mathrm{A} \cong -A_\mathrm{K}\frac{I_\mathrm{R}}{I_\mathrm{A}}. \tag{4.10}$$

To a first approximation, we assume that the absorbed intensity I_A is proportional to the total photoemission yield I_PE, $I_\mathrm{A} \propto I_\mathrm{PE}$. In this case, the proportionality factor cancels in Eq. (4.9) resulting in $A_\mathrm{PE} = A_\mathrm{A}$. Expressing the reflected and absorbed intensity in terms of the reflectivity R, $I_\mathrm{R} = RI_0$, and $I_\mathrm{A} = (1-R)I_0$, the MCD asymmetry in photoemission is then given by:

$$A_\mathrm{MCD} = A_\mathrm{PE} \cong -A_\mathrm{K}\left(\frac{R}{1-R}\right) = 2\epsilon_\mathrm{K}\left(\frac{R}{1-R}\right). \tag{4.11}$$

In order to check if this is a possible description the 2PPE near-threshold MCD asymmetry is compared to the Kerr ellipticity measured at 3.1 eV. By means of an additional quarter wave plate monolayer-thickness sensitive measurements of the Kerr ellipticity are performed at an external field of 255 mT. Fig. 4.10 depicts the near-threshold MCD asymmetry (full squares) and the Kerr ellipticity measurement (full dots). In order to allow for a direct comparison, all ellipticity values are already converted according to Eq. (4.5). Considering that by varying the

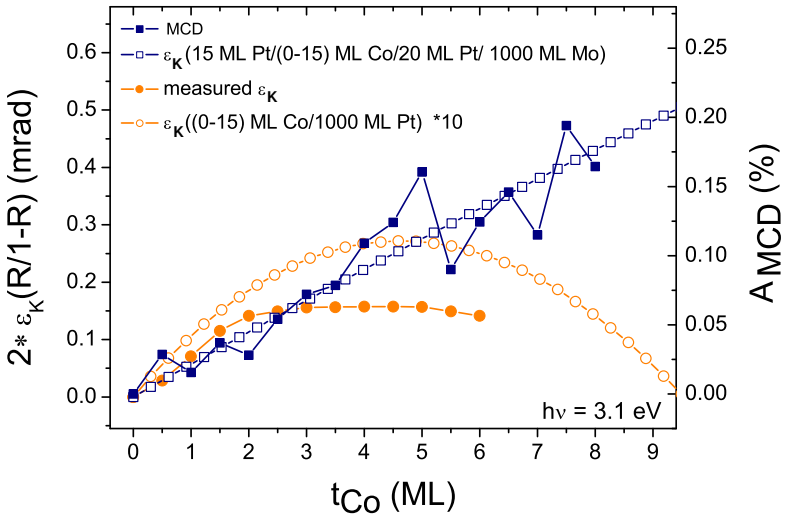

Figure 4.10: Comparison of the 2PPE near-threshold MCD asymmetry (full squares) with the polar Kerr ellipticity measured with 3.1 eV photon energy at an external field of 255 mT (full dots) and calculated polar Kerr ellipticities for different sample systems. (open squares) 15 ML Pt/(0-15) ML Co/20 ML Pt/1000 ML Mo. (open circles) (0-15) ML Co/1000 ML Pt. The calculations are carried out for 3.1 eV. To compare the Kerr ellipticities to the near-threshold MCD asymmetry the ellipticity values are converted according to Eq. (4.5). In the case of the Pt substrate the values are additionally multiplied by a factor of 10.

Co thickness from (0-3.2) nm the reflectivity R is changed by less than 1 %[3] and keeping in mind that there is only a thickness-independent influence of the Pt capping layer, a value of $R = 0.75$ is used for a 15 ML Pt/(0-16) ML Co wedge on Pt at hν = 3.1 eV [85].
The polar Kerr ellipticity does not show the same behavior as the near-threshold MCD asymmetry: Up to a thickness of ~ 2 ML the ellipticity steadily increases, for larger Co thicknesses, however, it saturates while the asymmetry further increases. Moreover, the near-threshold MCD signal is about one order of magnitude larger than deduced from Eq. (4.5). This can be attributed to a selection in energy and k-values in near-threshold photoemission leading to higher asymmetries. On the one hand for near-threshold MCD only states in the vicinity of the Fermi level are involved, while all states from E_F to $E_\mathrm{F} - h\nu$ can participate in the excitation process in MOKE. This directly leads to an averaging over many transitions resulting in reduced Kerr signals. On the other hand, in normal electron emission close to threshold only a narrow cone of k-vectors inside the material can contribute to the electron yield. The majority of the electrons is excited outside this narrow cone and stays inside of the material due to total reflection at the surface. All these electrons contribute to photoabsorption but not to the electron yield. Moreover, we note that the observed discrepancy in the quantitative values might also be partly related to the fact that a two-step process in photoemission is compared to a one-step excitation within Kerr measurements. In the following chapters we will see, however, that 2PPE generally delivers larger MCD signals than the corresponding 1PPE excitation processes. Nevertheless, this cannot justify a quantitative disagreement of one order of magnitude and an obviously different qualitative behavior. In Ch. 4.3 we will furthermore demonstrate that other excitation processes existing beyond the conventional photoemission theory of normal electron emission might also play a significant role for enlarged MCD effects.
In addition, due to the saturation effect of the measured Kerr ellipticity the latter does not seem to satisfy Eq. (4.4), predicting a linear increase with thickness. However, thickness dependent calculations for different sample systems and photon energies reveal that ϵ_K as well as θ_K generally show a continuous increase with increasing sample thickness [86]. Deviations from this behavior only occur for those photon energies where the Kerr signal is close to zero or even exhibits a zero-crossing. The appropriate calculations are carried out by a program code [87] based on calculations of so-called medium boundary and medium propagation matrices which allow for a complete description of the magneto-optical coefficients for a multi-layered film and which can also be applied to ultrathin film systems. For further information concerning this approach we refer to Ref. [88].
Fig. 4.10 also depicts the thickness dependence of the calculated Kerr ellipticity for a 15 ML

[3] The variation of the Co thickness from 0-16 ML does not have a considerable influence on the reflection coefficient. This can be shown by using Eq. (9) from Ref. [85]. We use the equation describing a 4-layer system to calculate the reflection coefficients for different thicknesses of a Co wedge evaporated on Pt and capped by an additional Pt-layer (i. e. layer 1: vacuum; layer 2: Pt-capping; layer 3: Co wedge; layer 4: Pt-buffer). Due to the large Pt buffer layer the W(110) substrate additionally used in the measurements can be neglected. For different Co thicknesses, namely 0.2 nm, 1.2 nm, 2.2 nm and 3.2 nm, the reflection coefficients vary by less than 1 %; an average value of $R = 0.75$ has therefore been assumed.

Pt/(0-15) ML Co/20 ML Pt/1000 ML Mo sample (open squares). Since the data for tungsten cannot be incorporated in the program code, Mo is chosen to reasonably model the present sample system. Similar to the near-threshold MCD asymmetry the calculated ellipticity steadily increases with the sample thickness and does not show any deviations from a linear behavior. It should be noted that the polar Kerr ellipticity of this sample system is not close to zero at photon energies around 3.1 eV. For comparison, ϵ_{K} of a (0-15) ML Co/1000 ML Pt sample is also calculated, and the corresponding ellipticity values are multiplied by a factor of 10 (open circles). This curve does not show the same characteristics; on the contrary it resembles the shape of the measured ellipticity curve. The Co/Pt sample system exhibits a Kerr ellipticity close to zero between about 2.8 and 3.4 eV, which might be the reason for the differing behavior. Disregarding the different magnitudes of the quantities, the calculated behavior corresponds to the measured Kerr ellipticity. We conclude that deviations of the Kerr ellipticity from the linear thickness dependence are connected to photon energy ranges where the polar Kerr ellipticity is close to zero or even exhibits a zero-crossing. For the present sample system the measured Kerr ellipticity deviates from a linear behavior indicating that ϵ_{K} might be close to zero in the vicinity of 3.1 eV. The measured values can be compared best to the calculated Kerr ellipticities for a (0-15) ML Co/1000 ML Pt wedge. If ϵ_{K} is not close to zero around 3.1 eV it is expected to depend linearly on the sample thickness. This is the case for the Mo substrate. Since for the same sample system and photon energy the behavior as well as the magnitude of ϵ_{K} in dependence of the sample thickness strongly deviate from the near-threshold MCD asymmetry, we further conclude that Eq. (4.5) cannot adequately describe the relation between the Kerr ellipticity and the near-threshold MCD asymmetry. Obviously, it does not suffice to apply the Jones formalism to threshold photoemission under the assumption that the absorbed light intensity is proportional to the total photoemission yield. On the contrary, the influence of the Einstein equation of photoemission which determines the involved initial states by considering the photon energy as well as the sample work function might cause a strong selection of particular interband transitions. Possible k-selecting mechanisms are also not considered in the present approach. An adequate treatment of MCD in near-threshold photoemission might only be possible by a detailed analysis of the corresponding band-structure scheme under the condition of energy and momentum conservation which directly leads us back to the theoretical approach already tested for the two Heusler alloys in Ch. 4.1.

Finally, we have to consider the influence of the Pt cap layer. Fig. 4.11 depicts the calculated Kerr rotation (open squares) and Kerr ellipticity (full circles) at 3.1 eV for a 5.5 ML Co/20 ML Pt/1000 ML Mo sample in dependence of the Pt capping layer thickness. These simulations are also carried out on the basis of the matrix calculations presented in Ref. [88]. With increasing thickness of the capping layer the Kerr rotation decreases rapidly due to the increasing absorption of the incident light by the nonmagnetic overlayer until the ferromagnetic signal fades out at a capping thickness of about 30 nm. Assuming an exponential decrease with increasing thickness of the capping layer we determine an information depth ($1/e$-decrease) of ~ 9 nm. With a 4 nm Pt capping the Kerr rotation has already decreased to 70 % of the initial value, and it can be assumed that this leads to a reduction of the MCD asymmetry, as well: measurements of Marx et al. [62] have demonstrated that a cap layer (in that case Ag)

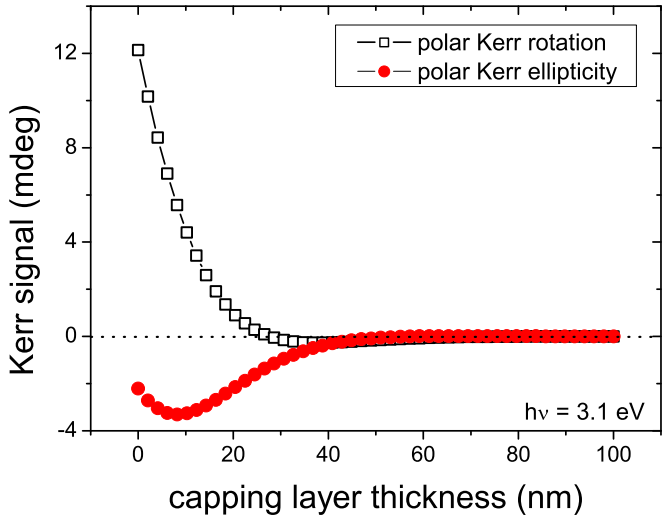

Figure 4.11: Calculated polar Kerr rotation (open squares) and polar Kerr ellipticity (full circles) in dependence of the capping layer thickness for a 5.5 ML Co/ 20 ML Pt/1000 ML Mo sample system. The calculation are carried out for 3.1 eV.

substantially reduces the MLD asymmetry measured for a Ag/Fe/W system. While for Kerr measurements an information depth of 21.5 nm was found, a value of 16.2 nm was derived for photoemission measurements. Due to the limited mean free path of the detected electrons MCD experiments are more surface-sensitive than Kerr measurements. Therefore, the MCD asymmetry will decrease more rapidly with increasing capping layer thickness, i. e. in our case the information depth of the MCD will be smaller than 9 nm. On the other hand, our experiments show no saturation of the near-threshold MCD with increasing Co thickness up to 8 ML (1.6 nm). This means that the information depth of the near-threshold MCD effect is larger than 1.6 nm. The reduction of the MCD asymmetry due to a cap layer arises for different reasons: Photoemission from the Pt capping will lead to a background signal that shows no MCD (except for a possible small polarization of Pt at the interface). The Pt contribution to the total signal will thus diminish the observed asymmetries. Furthermore, considerable transport losses of the Co photoelectrons occur in the cap layer that may depend on the Pt band structure. The losses do not depend on the photon helicity, so they will not diminish the MCD asymmetry but the intensity which, in turn, impairs the detection of MCD asymmetries. Overall, the transport losses of the Co photoelectrons and the additional intensity by the Pt photoelectrons cause a decrease of the MCD asymmetry.
In contrast to the Kerr rotation, the absolute value of the Kerr ellipticity increases with the capping thickness until a maximum around 8 nm, followed by a rapid decrease (Fig 4.11). At 30 nm Pt capping the Kerr ellipticity is also nearly zero. This is interesting, since the Kerr ellipticity is also expected to decrease with increasing capping layer thickness. The reason for this behavior might be found in the exact calculation of the medium boundary and medium

propagation matrices based on the optical Fresnel equations.

4.2.5 Summary and conclusions

Near-threshold photoemission in 1PPE and 2PPE has been investigated for a Pt-capped Co wedge on Pt(111)/W(110). At 5 ML (SRT at 5.5 ML) asymmetry values of 0.07 % for 1PPE and 0.11 % for 2PPE are measured. These values are of the same order of magnitude as those of the capped Heusler alloys (cf. Ch. 4.1) but a factor of 100 smaller than values detected for a Ni(001) system [9]. On the one hand, such large magnetic asymmetries might be attributed to unique features of Ni(001). On the other hand, the observations might also lead to the assumption that a capping layer does not only diminish the magneto-optical quantities as calculated above but might also reduce the MCD asymmetry. Further measurements at uncapped sample systems should clearly judge the influence of an additional capping layer.
For 2PPE as well as for 1PPE the asymmetry increases continuously with the film thickness. While in the case of 2PPE a linear dependence of the wedge thickness is found, the behavior for 1PPE is more subtle. Two linear sections with different slopes are detected and attributed to different prevailing Co crystal structures. These results allow some conclusions to be drawn: the basic mechanism leading to near-threshold MCD must be connected to Co bulk properties, surface effects do not play a crucial role. This also means that most electronic excitations might be traced back to transitions in the Co bulk band structure. Especially for an uncapped Co system it would be helpful to compare measured asymmetry values to theoretical results for interband transitions. Due to the linear dependence of the asymmetry on the sample thickness, the SRT does not visibly influence the asymmetries in both cases. An influence of the magnetization easy axis on the asymmetry for a perpendicularly magnetized film has therefore not been detected.
Furthermore, the comparison of the thickness dependence of the near-threshold MCD asymmetry in 2PPE to measured and calculated Kerr ellipticities on the basis of Eq. (4.5) shows that a description of MCD on the basis of the Jones formalism is not adequate. Apparently, simulations on the basis of linear response theory in combination with relativististic energy band calculations as presented in Ch. 4.1 seem to be a more promising approach to a theoretical description of near-threshold magnetic circular dichroism. Due to the measured bulk-sensitivity it would in particular be of interest to look for transitions involving Bloch-states as initial and final band states.
Finally, the experiments reveal the information depth of the magnetic dichroic signals to lie between 1.6 and 9 nm.

4.3 Energy- and angle-dependent near-threshold MCD from an ultrathin Co/Pt(111) film

4.3.1 Motivation

The investigations on the capped Heusler alloys (Ch. 4.1) and the capped Co wedge (Ch. 4.2) lead to the assumption that a capping layer reduces the MCD signals and that it might be advantageous to investigate ultrathin film systems without capping. Also the question remains whether Ni/Cu(001) is the only sample system revealing enlarged magnetic asymmetries or if other systems might deliver comparable asymmetry values. In order to gain insights into these issues an uncapped ultrathin Co film evaporated on a Pt(111) single crystal has been investigated and the obtained results are presented in the following.
For Ni/Cu(001) it was furthermore demonstrated that the MCD asymmetry is very threshold-sensitive: It is enhanced directly at the photoemission threshold and drops to 65 % (50 %) of the threshold value for 1PPE (2PPE) at a photon energy 0.2 eV larger than the sample work function [9]. This behavior raises the question whether other systems also show a similar energy dependence of the MCD asymmetry. Otherwise, the magnitude and the behavior of the observed asymmetries [9, 63, 65] might be connected to special band structure features for the case of Ni/Cu(001), in particular the existence of a spin-orbit split band close to the Fermi level E_{F} at the high symmetry point X [26].
Moreover, the dependence on the incidence angle of the photon beam has up to now been investigated for the Ni case only. Here, the sample showed an enhanced 2PPE asymmetry at grazing incidence, for 1PPE the asymmetry stays almost constant over a wide range of incidence angles (0°-60°) [65]. To understand its origin, however, more systematics is needed. Especially for applications with PEEM it is of interest to examine under which conditions enlarged MCD asymmetries in near-threshold photoemission arise for grazing incidence.
Finally, the asymmetry behavior for single- and multi-photon-photoemission processes is a very interesting issue since it would give important information about the properties of magnetic circular dichroism for different excitation mechanisms in threshold photoemission. Studying 1PPE would deliver gainful insights into the outright excitation of electrons from initial to final states. From MCD measurements in 2PPE we can expect new information about the two excitation steps and the intermediate state involved in the process.
In order to address the mentioned issues, energy- and angle-dependent 1PPE and 2PPE MCD-measurements are performed at a Co/Pt(111) system in near-threshold photoemission. Since simulations on the basis of spin-resolved band-structure calculations in combination with linear response theory seem to be promising for a quantitative analysis of the magnetic dichroic signals (c. f. Ch. 4.1) we use this formalism to explain the MCD asymmetries for Co/Pt(111) in near-threshold photoemission.

4.3.2 Sample preparation

Before deposition the Pt(111) single crystal is cleaned by Ar-ion sputtering (120 min, $p \sim 4 \cdot 10^{-6}$ mbar) and subsequent annealing (30 min, 670 °C) at a pressure of $p \sim 4 \cdot 10^{-9}$ mbar. In order to prepare a sample simultaneously revealing bulk-like properties (i. e. $t \geq 3$ ML) and an easy axis perpendicular to the sample surface a Co thickness of 4.5 ML is chosen. Bulk-like properties are desirable to interpret the results in terms of a Co bulk band structure. A perpendicular easy axis reflects a dominating contribution of the magneto-crystalline anisotropy which is promising for large MCD signals. The deposition is carried out with a rate of 1 ML/4.5 min. The quality of the substrate surface and the epitaxial Co film is controlled by LEED. Fig. 4.12 depicts LEED images of the clean Pt(111) single crystal at an electron energy of 129.9 eV (a) and the 4.5 ML thick Co film at 129.7 eV (b). The sixfold symmetry of the single crystal and the epitaxial Co film can be clearly seen. The reflections with highest intensity in (b) correspond to the Co lattice (right arrow), while the neighboring inner reflections (left arrow) originate from the Pt substrate. Also visible is a modulation of the Co lattice reflections induced by the underlying substrate. This superstructure represents a Moiré pattern arising from regular dislocations [89, 90]. Fig. 4.12(c) depicts a sketch of the prepared sample system.

4.3.3 Results

Since an uncapped sample system is investigated all measurements are performed with the experimental setup shown in Fig. 3.4. The use of lock-in technique is not necessary and the asymmetries can be directly calculated from the recorded photocurrent.
After preparation the sample is investigated by in-situ polar magneto-optical Kerr measurements for which linearly polarized 636 nm laser light is used (c. f. also Fig. 3.2). Fig. 4.13 (a) depicts a Kerr measurement. The observed easy axis curve in the polar geometry (remanence equals saturation, coercive field 580 Oe) shows that the sample magnetization is oriented along the surface normal. The Kerr rotation in saturation amounts to 22.6 m°. Compared to the value for the Pt-capped system (Ch. 4.2) the Kerr rotation angle is almost twice as large indicating that the capping layer reduces the Kerr rotation.
MCD measurements in near-threshold photoemission are carried out by using a broadband ultrashort TiSa pulse laser with photon energies in the range of hν = (5.06 - 5.84) eV for 1PPE and hν = (2.46 - 2.92) eV for 2PPE (c. f. Ch. 3). To generate 2PPE processes an additional lens (f = 15 mm) is used again and a possible admixture of one-photon photoemission processes is cut off by using an optical filter. Fig. 4.13 (b) shows a typical 1PPE MCD measurement in the vicinity of the threshold. It represents an average over 30 hysteresis loops. Each hysteresis loop consists of 160 current readings. For 2PPE measurements 240 current readings per hysteresis loop are taken. Since all hysteresis loops reveal easy axis magnetization curves, the asymmetry for 1PPE as well as for 2PPE is evaluated as follows:

$$A_{\mathrm{MCD}} = \frac{\overline{I_{\mathrm{S}}}^{\mathrm{M}+} - \overline{I_{\mathrm{S}}}^{\mathrm{M}-}}{\overline{I_{\mathrm{S}}}^{\mathrm{M}+} + \overline{I_{\mathrm{S}}}^{\mathrm{M}-}} , \tag{4.12}$$

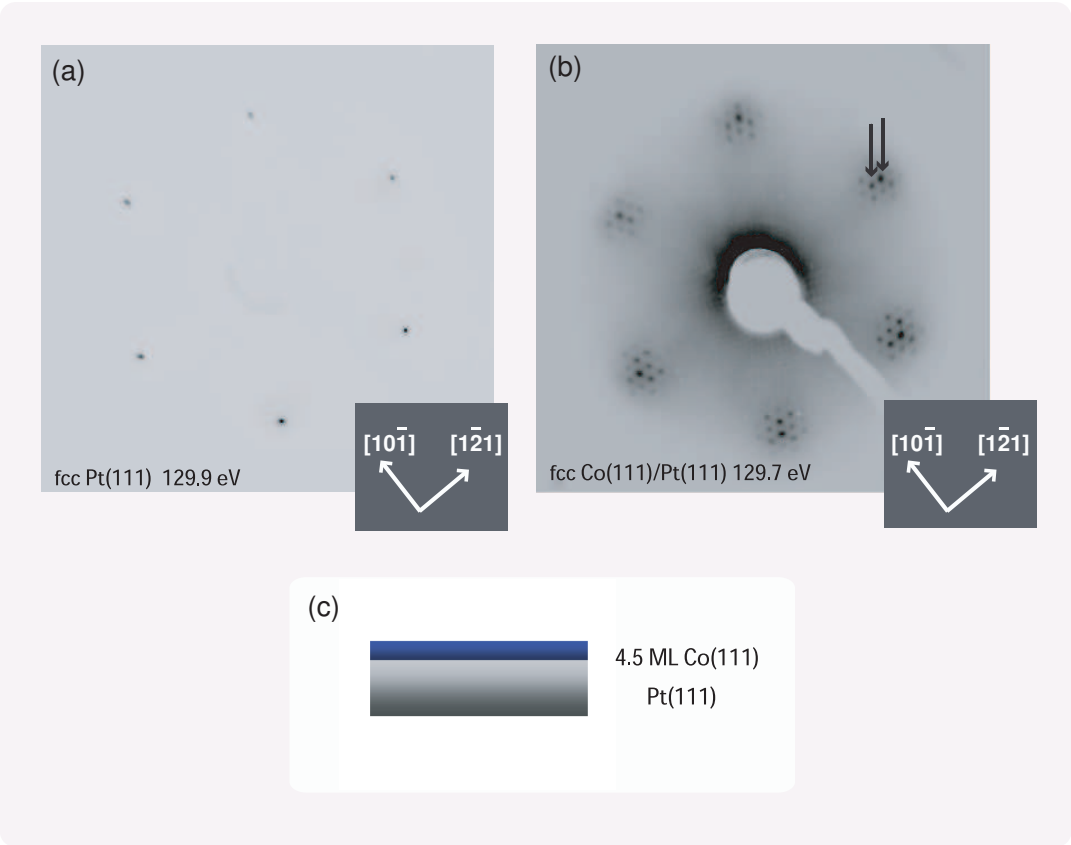

Figure 4.12: (a) LEED pattern of the Pt(111) single crystal after cleaning at 129.9 eV. (b) LEED pattern of the 4.5 ML Co/Pt(111) film at 129.7 eV. (c) sketch of the prepared sample system.

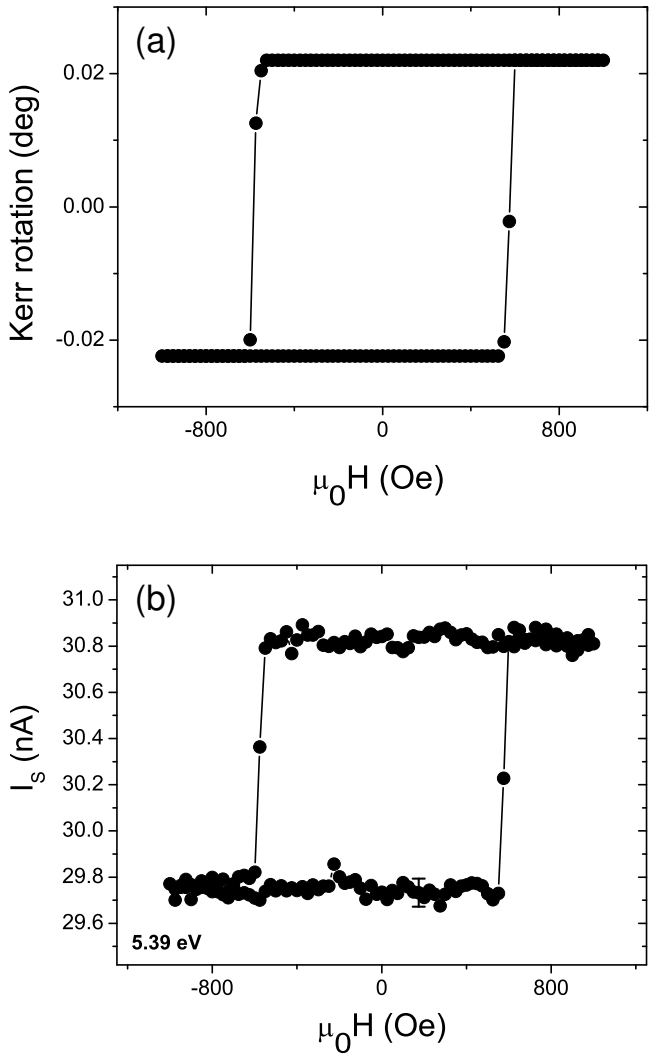

Figure 4.13: (a) Polar Kerr measurement. The error bars are of the order of the symbol size. (b) Drift corrected 1PPE MCD measurement in the vicinity of the threshold showing the sample current at a photon energy of 5.39 eV. The figure represents an average over 30 hysteresis loops, each hysteresis loop consisting of 160 current readings. A typical error bar is shown on the bottom branch.

where $\overline{I_{\mathrm{S}}}^{\mathrm{M}^+}$ ($\overline{I_{\mathrm{S}}}^{\mathrm{M}^-}$) are the averaged values of the sample currents for positive (negative) sample magnetization direction measured for a fixed photon helicity. This means that for the uncapped sample systems all investigations are carried out corresponding to the detailed experimental view shown in Fig. 3.3 (b) for fixed helicity. In each measurement we ensure that a reversal of the photon helicity leads to a reversal of the asymmetry.
In order to determine the sample work function the dependence of the electron yield on the

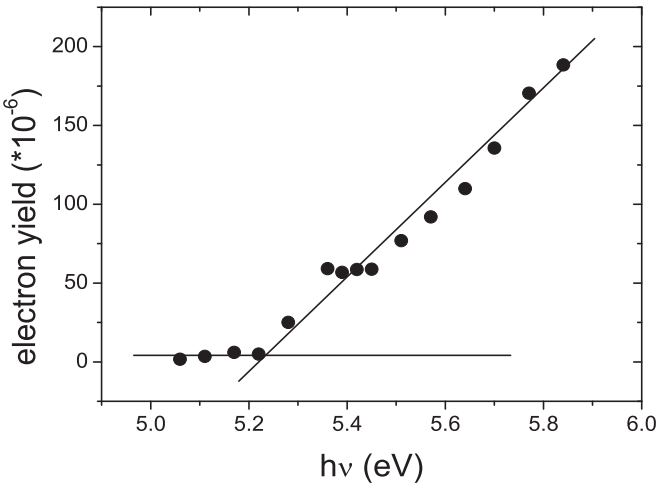

Figure 4.14: Dependence of the electron yield on the photon energy for the determination of the sample work function.

photon energy is measured in the range of hν = (5.06 - 5.84) eV. This dependence is plotted in Fig. 4.14. The electron yield is defined as: $N = \frac{I_S \cdot h\nu}{P \cdot \mathrm{e}}$, where N is the number of electrons, I_S is the sample current, hν is the photon energy, P is the power of the laser beam and e is the elementary charge. For an energy difference $\leq$ 1 eV between the photon energy and the sample work function a linear relation between the electron yield and the photon energy is found. For photon energies smaller than the sample work function the electron yield approaches almost zero. A linear fit determines the work function to $\Phi = (5.23 \pm 0.1)$ eV in the case of 1PPE. The determination of the work function prior to the 2PPE measurement leads to $\Phi = (4.98 \pm 0.1)$ eV. The reason for this slightly changed value might be a contamination from residual gas adsorption.

Photon-energy dependent MCD measurements in near-threshold photoemission

Fig. 4.15 depicts the energy dependence of the MCD asymmetry for 1PPE (a) and 2PPE (b). The dashed lines mark the positions of the photoemission thresholds determined from the work function measurements. In 1PPE as well as in 2PPE the asymmetries are maximum at threshold and drop slightly with increasing photon energy. The relative loss of asymmetry per energy interval is nearly the same for both measurements. However, the absolute asymmetry values differ strongly: in the case of 2PPE a threshold value of $11.7\,\%$ is detected while for 1PPE only a value of $1.9\,\%$ is reached. Furthermore, in both cases asymmetry values are observable below the photoemission threshold. Partial band occupation above the Fermi level at 300 K and the spectral width of the laser give reasons for this. The apparent weak oscillation

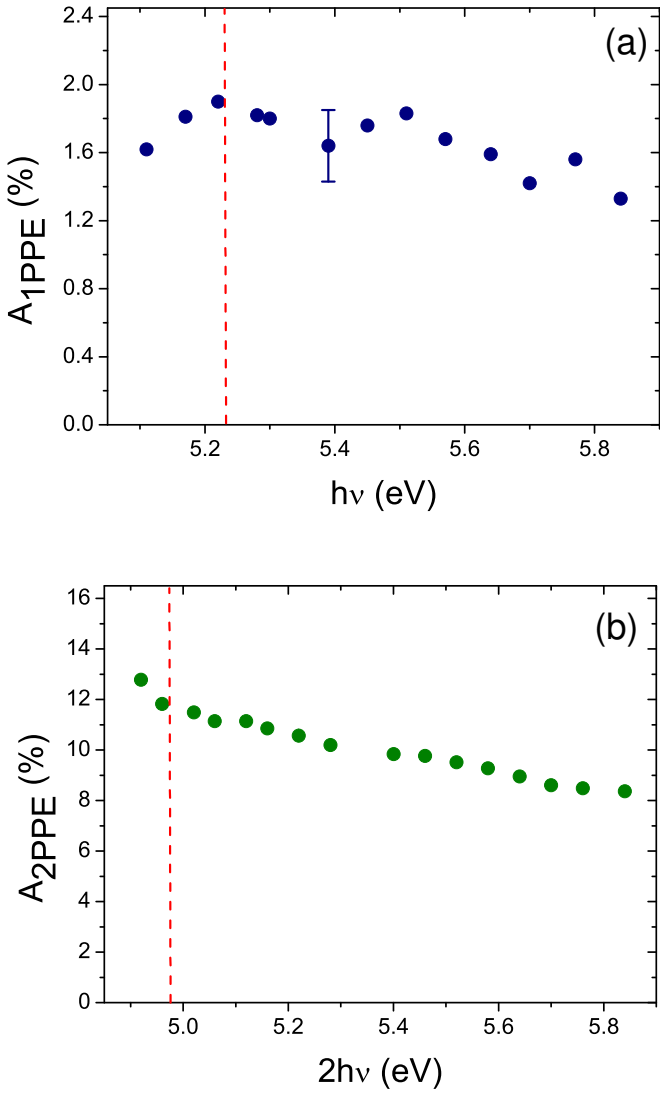

Figure 4.15: (a) Photon energy-dependence of the 1PPE MCD asymmetry for 4.5 ML Co/Pt(111). (b) Same for the 2PPE MCD asymmetry. The dashed lines mark the photoemission thresholds determined from work function measurements. All measurements are carried out with the magnetization vector oriented perpendicular to the sample surface and parallel/antiparallel to the helicity vector of the incoming laser light. For 1PPE a characteristic error bar is derived that is mainly due to statistical fluctuations of the measured data. For 2PPE the error bars are in the order of the symbol size because of the larger absolute asymmetry values.

in (a) might be attributed to instabilities in the generation of the laser light (fourth harmonic) as well as slight differences in the efficiency of the broad band quarter wave plate for different wavelengths. The energy dependence and the different absolute asymmetry values in 1PPE and 2PPE will be discussed later.

MCD measurements in near-threshold photoemission in dependence of the sample rotation angle

For 1PPE at hν = 5.22 eV as well as for 2PPE at hν = 2.46 eV MCD measurements are carried out for a varying rotation angle of the sample with respect to the helicity vector $\vec{\Lambda}_\sigma$ of the incoming photon beam and the direction of the applied magnetic field $\vec{H}$. Fig. 4.16 (a) depicts the experimental situation outside of the sample: during the angle-dependent measurements $\vec{\Lambda}_\sigma$ and $\vec{H}$ stay parallel ($\vec{\Lambda}_\sigma \,||\, \vec{H}$). At an angle of incidence of $\vartheta = 0°$ the vectors $\vec{\Lambda}_\sigma$, $\vec{H}$ and $\vec{M}$ are therefore aligned parallel to each other and perpendicular to the sample plane. By rotating the sample by an angle of ϑ the external field $\vec{H}$ causes the sample magnetization to deviate from the perpendicular orientation. Applying a sufficiently large external field would result in a parallel orientation of $\vec{M}$ and $\vec{H}$. This is not the case for finite external fields. $\vec{M}$ is thus oriented under an angle of θ with respect to $\vec{H}$ and under α concerning $\vec{n}_\vartheta$, respectively. Fig. 4.16 (b) depicts the experimental situation inside the material. Due to Snell's law the incoming photon beam is refracted; the direction of the helicity vector is therefore changed and forms the internal polar angle of incidence ϑ' with the surface normal. The angle between the magnetization direction and the helicity vector inside the material is consequently given by $(\alpha - \vartheta')$.

Fig. 4.17 shows the dependence of the 1PPE and 2PPE asymmetry on the sample rotation angle in near-threshold photoemission. While for 1PPE the asymmetry stays almost constant, A decreases with increasing rotation angle (i. e. with increasing angle of light incidence) in the case of 2PPE. Large angles of light incidence normally result in a polarization loss for incoming circularly polarized photons in the sample material. This behavior is well reproduced by the angle-dependent measurements in the case of 2PPE, but not for the case of 1PPE. Additionally, the polarization change also depends on the wavelength of the incoming photons and is therefore different for different photon energies. At first glance, this could be an explanation for the different 1PPE and 2PPE angle-dependence.

To investigate this issue we simulate the polarization loss inside the material in a MCD experiment for the two wavelengths used for 1PPE and 2PPE. In doing so, we have to calculate the modification of the electric field inside the solid due to the optical response of the material. The internal electric field is approximated by a classical radiation field described by the Fresnel equations (Fresnel-field approximation). Following Ref. [92] where the authors assume normal electron emission from a cubic (001) surface with perpendicular magnetization magnetic dichroism appears if the term $Im\left[\cos\vartheta' E'_{||} E'^{\,*}_{\perp}\right]$ is non-zero. $E'_\perp = \frac{2\cos\vartheta E_\perp}{\cos\vartheta + \sqrt{\epsilon' - \sin^2\vartheta}}$ and $E'_{||} = \frac{2n'\cos\vartheta E_{||}}{\epsilon'\cos\vartheta + \sqrt{\epsilon' - \sin^2\vartheta}}$ are given by Fresnel's formulas and denote the amplitudes of the electric field components parallel and perpendicular to the plane of incidence inside the ma-

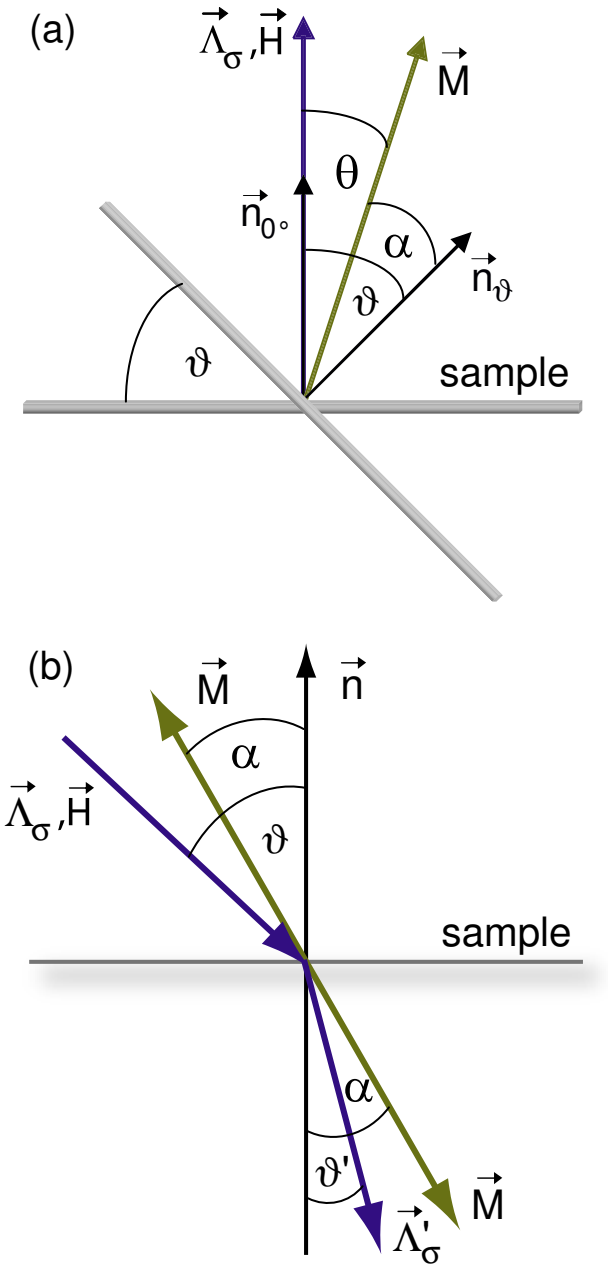

Figure 4.16: Illustration of the experimental situation according to measurements in dependence of the sample rotation angle. (a) Situation outside of the material: Rotating the sample by an angle ϑ results in a sample magnetization $\vec{M}$ oriented under α with respect to the surface normal $\vec{n}_\vartheta$ and under θ with respect to the photon helicity $\vec{\Lambda}_\sigma$ and the external magnetic field $\vec{H}$. The direction of $\vec{\Lambda}_\sigma$ and $\vec{H}$ is kept fixed during the measurements, only the sample is rotated. (b) Situation inside the material: The refracted photon beam is oriented under ϑ' with respect to the surface normal $\vec{n}$ and under $\alpha - \vartheta'$ with respect to the magnetization vector.

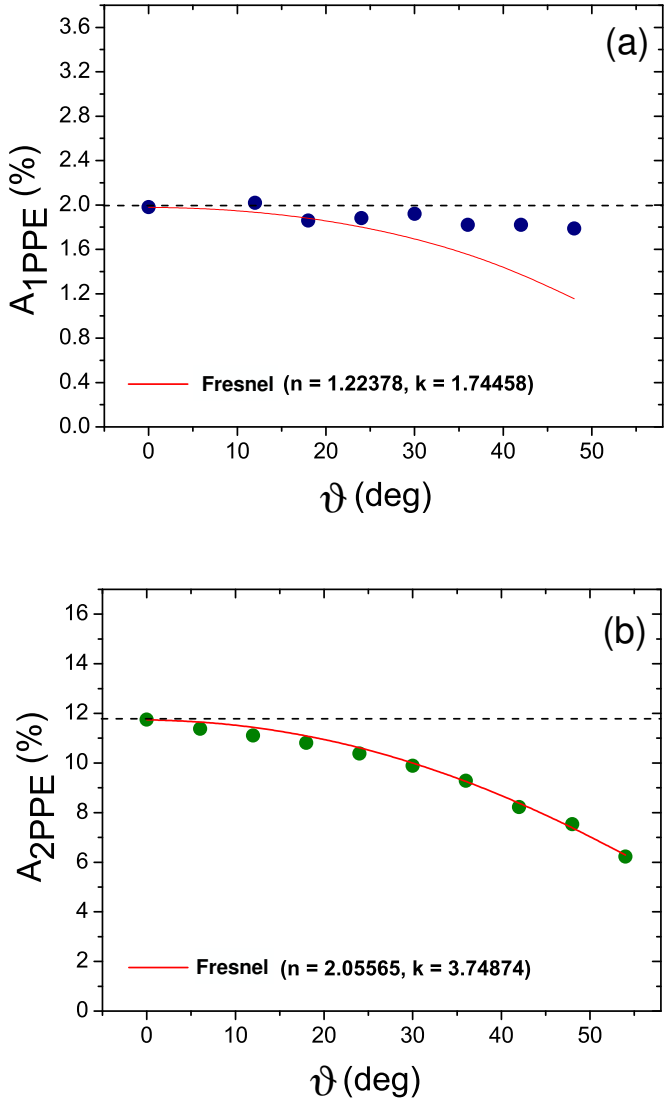

Figure 4.17: (a) Dependence of the 1PPE MCD asymmetry on the sample rotation angle measured at a photon energy of 5.22 eV for 4.5 ML Co/Pt(111). (b) Same for 2PPE MCD asymmetry measured at a photon energy of 2.46 eV. The full curves denote the calculations for the relevant MCD-generating term $Im[\cos(\alpha - \vartheta')E'_{||}E'^{*}_{\perp}]$ in a Fresnel-field approximation for 250 nm (4.96 eV, 1PPE) and 505 nm (2.46 eV, 2PPE) in Co bulk material.

terial; ϑ and ϑ' denote the external and internal polar angles of incidence, n' is the refractive index in the material (see also Ref. [92]). To simplify matters the optical response is in this case described by a dielectric constant ϵ' instead of a dielectric tensor; magneto-optical effects are thus neglected [4]. This reflects the fact that the polarization change due to the complex refraction index is much larger than magneto-optical effects which can be re-installed as a small perturbation in a second step. The term $\cos\vartheta'$ accounts for the fact that the MCD asymmetry is proportional to the scalar product of the helicity vector $\vec{\Lambda}'_\sigma$ of the photon beam in the material and the magnetization vector $\vec{M}$ as long as $\vec{M}$ is oriented parallel to the surface normal. The complete expression $Im\left[\cos\vartheta' E'_{||} {E'_\perp}^*\right]$ furthermore contains the modified electric fields and thus carries the entire information about the loss of circular polarization of the incoming radiation in the material. However, the above expressions only hold for $\vec{M} \,||\, \vec{n}$ which is not provided in our experimental setup for angles $\vartheta \neq 0$. For an adequate analysis we therefore have to account for the deviant orientation of the magnetization with respect to the surface normal. This is done by calculating the angle α in Fig. 4.16. Obviously, this also implies a deviant orientation of $\vec{M}$ with respect to $\vec{\Lambda}'_\sigma$ and thus demands the substitution $\cos(\vartheta') \rightarrow \cos(\alpha - \vartheta')$ in $Im\left[\cos\vartheta' E'_{||} {E'_\perp}^*\right]$.

The angle α can be computed by analyzing the free enthalpy $g(\alpha,\vartheta) = f(\alpha,\vartheta) - \vec{J_S}\cdot\vec{H}$ of the system which is formed by the system's free energy $f(\alpha,\vartheta)$ [5] and the Zeeman energy $\vec{J_\mathrm{S}}\cdot\vec{H}$ caused by the external magnetic field. In detail, the free enthalpy is given by [83]

$$\begin{aligned} g(\alpha,\vartheta) &= \frac{J_\mathrm{S}^2}{2\cdot\mu_0}\cdot\cos^2\alpha + K_1\cdot\sin^2\alpha \\ &\quad + K_\mathrm{me}\cdot\sin^2\alpha + \frac{K_\mathrm{S}}{t}\cdot\cos^2\alpha \\ &\quad - |\vec{J_\mathrm{S}}||\vec{H}|\cdot\cos(\vartheta-\alpha). \end{aligned} \tag{4.13}$$

The first term reflects the shape anisotropy; K_1 is the magneto-crystalline anisotropy constant, K_me the anisotropy constant due to magneto-elastic strain and K_S indicates the surface anisotropy constant including both interfaces. The higher order anisotropy term K_2 is neglected. $|\vec{J_S}| = 1.8\,\mathrm{T}$ is the magnetization in saturation, $|\vec{H}| = \frac{0.1}{\mu_0}\,\mathrm{T}$ is the applied external field, $t = 0.9\,\mathrm{nm}$ is the Co layer thickness, and $\mu_0 = 4\pi\cdot 10^{-7}\,\mathrm{Vs/Am}$ is the vacuum permeability. Minimizing $g(\alpha,\vartheta)$ with respect to α yields the equilibrium orientation of the magnetization vector in the external magnetic field, i. e. it directly yields α:

$$\begin{aligned} \frac{\partial g(\alpha,\theta)}{\partial\alpha} &= -2\left[L + \frac{K_\mathrm{S}}{t}\right]\cdot\cos\alpha\sin\alpha \\ &\quad - |\vec{J_S}||\vec{H}|\cdot\sin(\vartheta-\alpha) = 0, \end{aligned} \tag{4.14}$$

with $L = \frac{J_\mathrm{S}^2}{2\cdot\mu_0} - K_1 - K_\mathrm{me}$ representing the volume energy anisotropy constant. For L a value of $9.2\cdot 10^5\ \mathrm{Jm^{-3}}$ is taken from Ref. [91]. The surface anisotropy constant is calculated

[4] It is also assumed that the expressions will only slightly change for surfaces other than (001).

[5] The dependence of the system's free energy on the direction of its intrinsic magnetization (without an external magnetic field) is also called the magnetic anisotropy of the system.

by using a critical thickness for the spin-reorientation transition of $t_c = 1.1$ nm, which has previously been detected at a Co wedge on Pt(111). This gives $K_S = -1.01 \cdot 10^{-3}$ Jm^{-2}. The MCD-related term $Im\big[\cos(\alpha - \vartheta')E'_{||}E'^{*}_{\perp}\big]$ is finally calculated for one circular polarization $(E_{||}, E_{\perp}) = (1, i)/\sqrt{2}$ (the other one merely amounts to a change of sign) and by using the refractive indices for both wavelengths (250 nm for 1PPE, 505 nm for 2PPE) for Co bulk material taken from Ref. [93]. Note that for 1PPE a slightly different wavelength compared to the experiment (237.5 nm) is used since refractive indices for lower wavelengths are not available. To allow for comparison with the experiment the calculated values are additionally normalized at $\vartheta = 0°$. For 2PPE the theory confirms the measurement surprisingly well. In contrast the calculation for 1PPE cannot describe the measured constant behavior. Since the calculated polarization loss is, however, almost the same for 1PPE and 2PPE the measured data cannot be explained by the influence of different refractive indices due to different photon energies. A possible reason for this is the fact that the present theory only holds for bulk materials. However, for 1PPE the existence of a second interface to the substrate might be of greater importance compared to 2PPE because the real parts of the refractive indices of Co and Pt are different in the case of 1PPE while they are almost equal for 2PPE. In this context a theoretical model for ultrathin multi-layered structures as presented by Zak et al. [88] might be more adequate to capture the modification of circularly polarized light for a multi-layered film due to the optical response of the system. Furthermore, the electro-magnetic continuum model does not consider the local orbital anisotropy of the contributing electron states. This orbital anisotropy depends on the magnetization direction defining the quantization axis and on the helicity vector $\vec{\Lambda}_\sigma$. As the contributing states are different for 1PPE and 2PPE, it is no surprise that the angular dependence is different.

4.3.4 Discussion

As outlined above 1PPE as well as 2PPE MCD measurements reveal enlarged asymmetries compared to measurements for the capped system. In the case of the Pt capped Co wedge the sample exhibits asymmetry values of 0.06 % (1PPE) and 0.10 % (2PPE) at 4.5 ML Co thickness and fixed photon energies of 4.64 eV (1PPE) and 3.1 eV (2PPE). Due to a sample work function of Φ = 4.6 eV 1PPE (2PPE) experiments have been carried out 0.04 eV (1.6 eV) above threshold. In the case of the uncapped system asymmetries of 1.82 % (1PPE) at the same difference between photon energy and sample work function and 8.37 % (2PPE) at a maximum difference of 0.86 eV are measured. In both cases the asymmetry values are more than one order of magnitude larger than for the capped system. This observation validates the assumption that dichroic signals are reduced by a capping layer. Possible reasons for this decrease have already been given in Ch. 4.2.
Furthermore, we find that for the capped as well as for the uncapped system the 2PPE asymmetry is larger than the asymmetry in one-photon photoemission. However, the relative loss of asymmetry per energy interval is nearly the same in both cases as shown in Fig. 4.15. In the following we will use relativistic band-structure calculations to quantitatively analyze the origin and the behavior of the asymmetries for both excitation mechanisms. For 2PPE processes

the analysis of band transitions is thereby more complicated, since the electrons are excited via a two-step process. The intermediate state can be virtual or real and the selection rules might only apply treating 2PPE as a series of two one-step excitation processes. Moreover, the parity is changed in a one-step process while it does not change in the case of 2PPE.
The relativistic band-structure calculations are performed on the basis of the local spin-density approximation (LSDA) (c. f. Ch. 2.3.1). Fig. 4.18 shows the calculated energy bands of fcc Co using a lattice constant of $a = 0.35457$ nm for the low-index crystallographic directions. The dashed horizontal line indicates the vacuum level for 1PPE. The value for 2PPE lies 0.25 eV below. Vertical arrows denote possible transitions for 1PPE (dashed) and 2PPE (full arrows). According to energy conservation only bands located in a narrow region up to 0.61 eV (0.86 eV) below E_{F} can contribute to the 1PPE (2PPE) signal at the maximum available photon energies. The region for 2PPE has been hatched in Fig. 4.18, right-hand side. The bands are labeled only by numbers since spin and symmetry character of bands change along the crystallographic directions in a fully relativistic calculation. This is due to the fact that the spin as well as the spatial symmetry of the individual bands are no longer good quantum numbers in the presence of spin-orbit coupling, and bandmixing due to hybridization has to be taken into account. On the basis of Fig. 4.18 we now discuss two possible excitation scenarios A and B.

Excitation scenario A

Due to the negligible momentum transfer from the incoming photon to the electron in the considered photon energy range, in conventional photoemission theory the parallel electron momentum is conserved ($\Delta k_{||} = 0$). The electron momentum before and after the photoexcitation is therefore practically the same, and the electron can only undergo direct, vertical transitions in the band-structure scheme. In the special case of threshold photoemission only photoexcitations in the direction of normal electron emission are discussed since there is no excess energy left to excite states with non-zero parallel momentum ($h\nu - \Phi = 0$, $k_{||} = 0$). At the threshold these direct transitions are connected to a prompt emission of the electron in the direction of the surface normal. In our case the electron is excited perpendicular to the fcc (111)-surface which means that transitions can only take place in the normal emission direction Γ-L of the reciprocal lattice. This is captured by model A. Note that normal emission is strictly fulfilled only directly at the threshold, in the regime close to the threshold the escape cone effect limits possible transitions to small $k_{||}$ values (e. g. $k_{||_{\max}} = 0.23\,\text{Å}^{-1}$ at 0.2 eV excess energy).
Within model A bands 11 and 12 are good candidates for initial states. Although the calculated bands 11 and 12 in Fig. 4.18 are located slightly above the Fermi level, epitaxial strain and/or a possible doping effect of the Pt substrate could shift the actual bands closer to the Fermi level so that they might be occupied at finite temperatures. This assumption is supported by experimental data demonstrating photoemission directly from the Fermi edge in the Γ-L direction of fcc Co [94]. Bandmapping measurements on Co/Cu(111) furthermore reveal one of these bands to be located even 150 meV below E_{F} [6]. In agreement with former

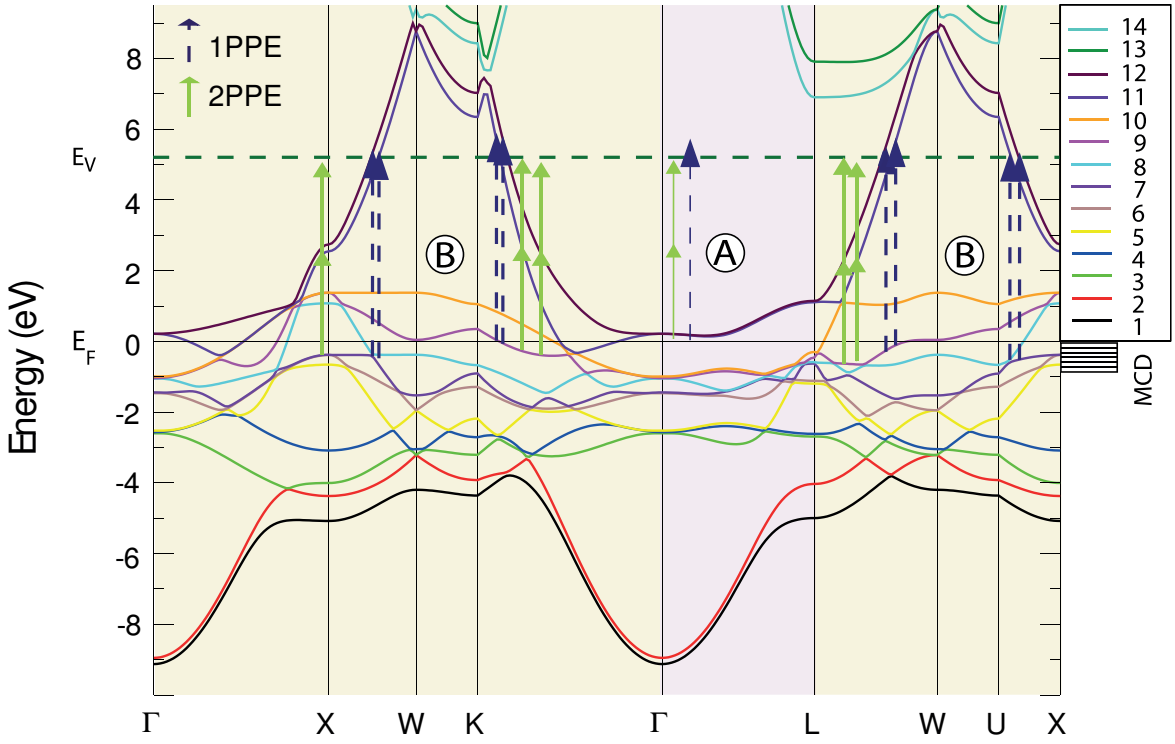

Figure 4.18: Band structure of fcc Co with a lattice constant of $a = 0.35457\,\mathrm{nm}$ [95]. The thin dashed (continuous) arrows denote possible 1PPE (2PPE) transitions in the Γ-L direction (model A), while the bold dashed and continuous arrows show the possible 1PPE and 2PPE excitations in all other crystallographic directions (model B) neglecting lifetime-broadening effects. The hatched region on the right-hand side denotes the energy range of initial bands contributing to the 2PPE signal. The dashed horizontal line indicates the position of the vacuum level E_V for the 1PPE measurements. Bands are labeled from bottom to top.

band-structure calculations [6, 30] the bands 11 and 12 are minority-spin bands in the Γ-L direction and carry d-character. Note that the band-character changes to sp-type along the L-W and U-X directions, and due to a spin-orbit induced avoided band-crossing band 11 adopts majority-spin character. Moreover, the bands 11 and 12 exhibit large densities of states in the vicinity of the Γ-point. However, no final state band exists in the energy range closely above the vacuum level (dashed horizontal line). Hence, 1PPE electrons are excited to evanescent states, being quasi-free continuum states that are strongly damped inside the material (transition marked with thin dashed arrow). In the case of 2PPE the transition along Γ-L can only proceed through a virtual intermediate state to an evanescent final state (thin full arrow). Both the virtual state and the final state carry minority character due to the prohibition of intersystem crossing. The fact that the relative loss of asymmetry per energy interval is similarly small for 1PPE and 2PPE points out that the possible intermediate states in 2PPE might be very similar to each other, thus influencing the energy dependence of the asymmetry in the same way. Therefore, one might be inclined to think of a 'broad band' of virtual intermediate states with similar properties.
In conclusion, model A relies on the assumption that only transitions in the Γ-L direction are involved in near-threshold photoemission from the (111)-face. It thus represents the conventional model of photoemission. However, in this approach electrons can only be excited to evanescent final and virtual intermediate states in the investigated photon energy range. In this context, 1PPE spectroscopy measurements on Co/Cu(111) [6] indeed reveal the loss of a prominent direct band-to-band transition peak when reducing the photon energy below 6 eV, but they do not unambiguously attribute the remaining photoemission intensity to direct transitions into evanescent states. Concerning 2PPE measurements, model A furthermore lacks an explanation of the enhanced absolute asymmetries compared to 1PPE as there are no real band-to-band transitions accounting for the difference of 1PPE and 2PPE MCD. Since the initial band already carries minority character a spin filter effect of the intermediate state can also be excluded. Here, the fact that 2PPE is a parity-conserving process could be of importance. But apart from this, the enhanced 2PPE asymmetries must be traced back to particular characteristics of the virtual intermediate state and the two-step excitation which cannot be further determined up to now. Finally, the most relevant argument against model A is presented in Ch. 4.2. There we show that the near-threshold MCD asymmetry for a Pt-capped Co sample is bulk-sensitive, i. e. the asymmetry increases with the film thickness up to 8 monolayers. This finding is highly incompatible with an evanescent final state that is located close to the surface and strongly damped inside the material. Due to these serious discrepancies we search for a possible explanation of the experimental results beyond the conventional approach. The bulk sensitivity of the MCD asymmetry indicates that for 1PPE as well as for 2PPE real states stemming from the Co bulk band structure must be involved in the excitation process. Accordingly, for 1PPE the final state is expected to be real, for 2PPE at least one of the participating states - the intermediate or the final state - should be real. It is thus nearby to consider directions different from Γ-L where interband transitions into real final (intermediate) state bands occur. This leads to scenario B.

Excitation scenario B

Considering other directions than Γ-L we follow a model which is normally used for photon-in/photon-out experiments such as the magneto-optical Kerr effect and which has proven to be a powerful approach for many different systems [38, 49]. Therein, all possible interband transitions in the whole Brillouin zone are considered and the dichroic signal is obtained by averaging over all k-directions. This means that not only the high-symmetry directions depicted in Fig. 4.18 are considered, but transitions in all crystallographic directions are taken into account. The theoretical foundations of this model are presented in Ch. 2.3. As already successfully carried out for the two Heusler alloys (c. f. Ch. 4.1) we transfer this photon-in/photon-out scenario to our photon-in/electron-out setup with an important modification: In a photoemission process the energy condition (Einstein equation) containing the work function of the material has to be considered, i. e. in near-threshold photoemission only a narrow region of initial states below E_F contributes to the observed photoyield. Energy conservation thus restricts the maximum available binding energy of the initial bands in our case to $E_{\mathrm{B}_\mathrm{max}}$ = 0.61 eV (0.86 eV) at the maximum available photon energies for 1PPE (2PPE) [6]. In scenario B we thus look for allowed interband transitions in all crystallographic directions with initial bands in the hatched binding energy interval in Fig. 4.18 (for 1PPE the hatched interval is slightly smaller). Such transitions are marked for 1PPE (thick dashed arrows) and for 2PPE (thick full arrows). For the 1PPE case we find interband transitions along Γ-K, U-X and along X-W and L-W. Here, transitions from the initial bands 7 and 8 are possible in X-W and U-X, while for transitions in Γ-K and L-W band 9 may serve as initial state. All excitations lead to the final bands 11 and 12. As already mentioned, Fig. 4.18 only displays the projections of the band structure in low-index directions. In the full 3D k-space there are many more such transitions in arbitrary k-directions. For 2PPE we look for transitions to real intermediate states, for which bands 11 and 12 come into consideration. Notably, we find 2PPE transitions of this kind close to the X-point and in the Γ-K and L-W directions. For Γ-K band 9 can be the appropriate initial state, for L-W electrons can be excited from bands 8 and 9. Most interesting might be the Γ-X direction since the transition takes place in the vicinity of the high-symmetry X-point. Bands 6 and 7 carrying high density of states close to X might serve as initial states. Also the intermediate state bands 11 and 12 exhibit high density of states at X. In all cases the final state for 2PPE is again an evanescent state [7]. The 1PPE and 2PPE processes are restricted to the mentioned transitions as long as lifetime-broadening of the intermediate and final states is neglected. By additionally considering this effect, excitations from other initial bands not mentioned above also become possible depending on the magnitude of the lifetime-broadening.

In analogy to model A the electron in model B undergoes direct vertical transitions in the band-structure scheme, too, as almost no photon momentum is transferred to the electron. However,

[6] In contrast a much larger area of initial states given by the photon energy contributes to magneto-optical Kerr measurements.

[7] Of course, transitions via a virtual intermediate state to a real final state might also be possible for the 2PPE case. However, calculations of the dichroic response point out that this is less probable (see page 82).

in contrast to model A the photoexcitation does not take place in the direction of normal electron emission, and additional momentum is needed to enable emission into vacuum. Possible assisting mechanisms will be discussed below.

MCD calculations in the framework of model B

To check the validity of model B we have performed *ab initio* calculations of the MCD asymmetry [95]. As discussed in Ch. 2.3 the appropriate theoretical formalism for deriving magnetic dichroic spectra is relativistic energy-band theory combined with linear-response theory to treat the magneto-optical response of the material. Here, we adopt this formalism to evaluate the electron intensities $I_{\mathrm{e}}^{\pm}$ from the computed optical conductivity tensor, $\boldsymbol{\sigma}$, and from these the MCD asymmetry using Eq. (4.12) for the case of reversed photon helicity. For a detailed description of the calculation we refer to Ch. 2.3.
For 1PPE and 2PPE excitation processes, specific conditions additionally have to be considered and included in the calculations of the $\boldsymbol{\sigma}(\omega)$ tensor as discussed below. Note as well that in the *ab initio* approach only transitions to real bands are accounted for; excitations to evanescent or virtual states are not regarded. In the light of the above discussion, this implies that the excitation process for 1PPE can be fully described, while for 2PPE only the first excitation step into a real intermediate state can be treated.
The 1PPE process is comparably easy to model. The escape of created photoelectrons requires their band-energy to be equal or larger than the work function. Hence, in the linear-response expression for σ_{ij} the sum over occupied initial states and unoccupied final states (see e. g. Ref.[44]) consists of only those final states with energies above the work function ($\epsilon_{\mathrm{final}} \geq \Phi$). Also, as mentioned before the maximum photon energy used in the experiment restricts the possible initial states ($\epsilon_{\mathrm{init.}} \geq -(h\nu_{\mathrm{max}} - \Phi)$).
2PPE MCD is not yet well understood and its modeling requires further assumptions. Two possibilities are discussed in Ch. 4.1. Thereby, the approach in which two photons are coherently and simultaneously absorbed is preferred to a model, where the 2PPE process consists of two unconnected 1PPE excitation steps. Here we also test the first way of computing 2PPE MCD for fcc Co assuming a real final state. According to the band structure the intermediate state is then virtual. This gives asymmetry values of the same order of magnitude as the 1PPE MCD, but it does not reproduce the measured values of about 10 %. This strongly suggests the involvement of an evanescent instead of a real final state. Therefore, we have only focussed on excitations into real intermediate states which are modeled by the *ab initio* calculations assuming similar conditions as above for 1PPE, but for $\Phi_{\mathrm{2PPE}}/2$ and corresponding photon energies.
We start our discussion of the calculated results with first considering the 1PPE process. Fig. 4.19 shows a spin-resolved calculation of the imaginary and real parts of the conductivities σ_{xy} and σ_{xx} for the 1PPE excitation as a function of photon energy. The black dashed curve gives the conductivity spectra due to majority-spin excitations, the red full curve those due to minority-spin transitions. A work function of 4.9 eV is used while a typical lifetime-broadening of 0.4 eV of the final state is assumed which is equivalent to a softening of the

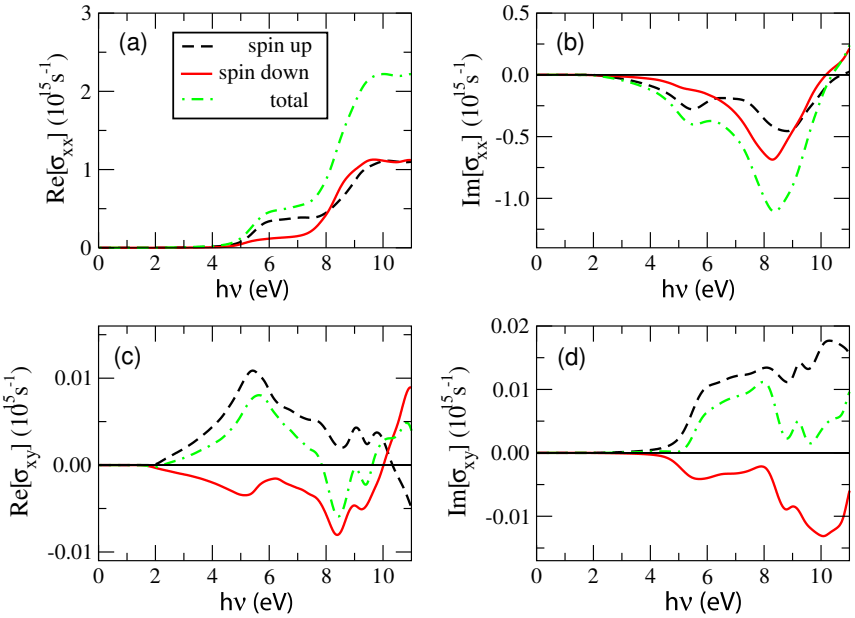

Figure 4.19: Calculated spin-resolved 1PPE optical conductivity spectra. Shown are the imaginary (b,d) and real parts (a,c) of σ_{xx} and σ_{xy} for 1PPE as functions of the photon energy. A work function of 4.9 eV and a lifetime broadening of 0.4 eV are assumed.

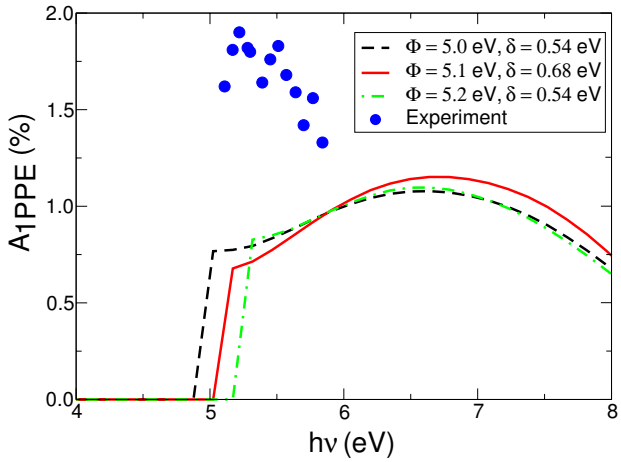

Figure 4.20: 1PPE MCD spectra of fcc Co computed for different work functions Φ and lifetime broadenings δ. The points represent the measured data.

energy condition for the maximum accessible binding energy. As a result, the absorptive parts of the spectra $\left(Re[\sigma_{xx}]\right.$ and $\left.Im[\sigma_{xy}]\right)$ increase steeply around the work-function value. The tail at energies $\leq \Phi$ is due to lifetime broadening effects. The dispersive parts of the spectra $\left(Im[\sigma_{xx}]\right.$ and $\left.Re[\sigma_{xy}]\right)$ can of course extend farther to lower energies. According to Eq. (2.54) the calculations reveal a strong asymmetry in the majority-spin and minority-spin contributions, particularly in the energy range of interest, $5-6\,$eV. In Fig. 4.20 we show several computed 1PPE MCD spectra calculated by averaging over all possible interband transitions in the whole BZ. The calculated MCD varies around $1\,\%$ which is about a factor of 2 smaller than the experimental values (dots). Towards the threshold the computed asymmetry falls off, whereas the experimental counterpart shows a slight increase. The behavior near the threshold in the calculations is related to how the conditions on the initial and final band energies are enforced. This means that depending on the choice of the experimental parameters (work function, maximum binding energy, lifetime broadening), which are not exactly known, the calculated energy dependence can change towards a better agreement with the measured trend of the MCD asymmetry. For Fig. 4.20 we have used reasonable values for the lifetime-broadening that showed good results for MOKE. One probable reason for the drop of the experimental values with increasing photon energy is that there is an increasing underlying background signal of secondary electrons that does not show an MCD. The reasonable correspondence in the magnitude of the calculated and measured (1PPE) MCD signal prompts that the basic mechanism for the 1PPE is the influence of spin-exchange and spin-orbit interactions on the single-particle energy bands. Both interactions are quite well captured by relativistic band-structure theory.

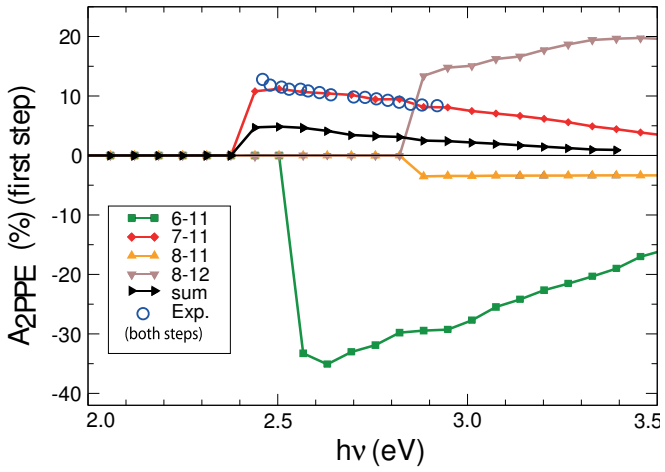

Figure 4.21: Simulation of the MCD for the first excitation step in a 2PPE process. Shown are the calculated MCD spectra of fcc Co due to several pertinent band transitions. A work function of 2.49 eV and a lifetime broadening of 0.4 eV are assumed. The resulting MCD of all bands is reduced to 5 % at hν = 2.5 eV. Values below 2.4 eV have been set to zero because of numerical errors due to small emission intensities.

As mentioned above, for 2PPE excitations in the vicinity of the X-point are of special interest. In the following we compute the first step of the 2PPE excitation process investigating the real interband transitions in the photon energy range of $h\nu = \Phi_{2PPE}/2 = 2.49$ eV up to $h\nu_{max} = 2.92$ eV. High MCD asymmetries result from the transitions of bands 6 and 7 to band 11 and 8 to 12 near X. In Fig. 4.21 we show the computed MCD of the corresponding excitation channels calculated through k-integration over the whole Brillouin zone. Thereby, most of the computed MCD values for individual interband transitions are much larger than the total 1PPE MCD (lying triangles) calculated by summing over all bands. Especially the transitions $6 \rightarrow 11$, $7 \rightarrow 11$, and $8 \rightarrow 12$ give maximal MCD values of -33 %, 10 %, and 14 %, respectively. The onset of the $8 \rightarrow 12$ (and also $8 \rightarrow 11$) transition is, however, just at 2.9 eV, i. e., at the end of the experimentally probed range. Therefore, these transitions contribute little to the experimental signal. Furthermore, the MCD spectrum is dominated by the $7 \rightarrow 11$ transition (diamonds): Although $6 \rightarrow 11$ gives also a remarkable MCD signal when computed for the single band-to-band transition (squares), its contribution is heavily reduced when summed up with other transitions [96]. Another argument for the dominant influence of the $7 \rightarrow 11$ transition is the fact that the calculated total MCD signal as well as the experimental data (open circles) exhibit the same energy dependence as computed for $7 \rightarrow 11$. The experimental data even almost coincide in their energy dependence with the simulated ones for $7 \rightarrow 11$. Due to contributions from all other allowed band-to-band transitions to σ_{xx} the total asymmetry is, however, reduced to values (5 % at hν = 2.5 eV) which are about a factor of 2 smaller than the experimental 2PPE MCD values. This is not astonishing considering that only the first

excitation step has been calculated.
The calculation validates that specific band-to-band transitions (in the vicinity of high-symmetry points) are very likely the source of the large 2PPE MCD. Through the rather narrow accessible energy range of 2.49 to 2.92 eV, mainly the $7 \rightarrow 11$ transition channel dictates the first step of the 2PPE excitation. Assuming that the MCD would not be reduced in the second excitation step to an evanescent final state, the resulting 2PPE MCD would be at least of the order of $5\,\%$ and, hence, larger than the 1PPE MCD. Since only the asymmetry for the first excitation process is derived the question whether the first step of a 2PPE excitation is the major asymmetry creating process remains unanswered. Further measurements should thus investigate the role of both excitation steps.
In summary, the model applied in scenario B yields agreement within a factor of 2 with the measured MCD asymmetries in the case of 1PPE. Even the partial calculation of 2PPE reveals asymmetry values in the same order of magnitude with the same energy dependence as measured in the experiment. Also the factor of 6 between the 2PPE and 1PPE asymmetries is well reproduced by theory. We thus propose the explanation that indeed interband transitions in other directions than Γ-L are responsible for the large MCD measured at Co films on Pt(111). In view of the encouraging agreement, we continue this non-conventional model and search for a mechanism that allows a (probably small) fraction of electrons with $k_{||} \neq 0$ to surmount the surface barrier. When irradiating the Co film with near-threshold photons, we induce direct interband transitions in different k-directions. Near-threshold excitation therefore creates many *hot* electrons in band states in various k-directions inside the material. The energy of these excited electrons is sufficient to overcome the surface barrier (all arrows in Fig. 4.18 end at or above E_{V}). However, their k-vectors point in various directions away from the surface normal. Therefore, additional momentum has to be transferred to the electron which can be realized by scattering processes. In electron-electron scattering the total energy is shared between the two interacting electrons. However, any energy loss of the photoexcited electron ends up in a state below E_{V} so that the electron cannot escape from the surface. Electron-phonon and electron-magnon scattering are thus left as the final possibilities. Since phonons/magnons carry large momenta but small energies a quasi-elastic scattering with a low-frequency phonon or magnon can transfer enough momentum to the electron to escape into vacuum: After the direct (vertical) interband transition in crystallographic directions different from Γ-L the excited electron travels towards the surface of the material. On its way it interacts with a phonon or a magnon, which scatters the electron back into the Γ-L-direction from where it is emitted into vacuum. Note that in electron-magnon scattering the spin of the electron is reversed, whereas for electron-phonon scattering this is mostly not the case. Since the present measurement technique is not sensitive to the spin of the escaping electron the two processes cannot be distinguished. In normal photoemission experiments these weak contributions are masked by the strong direct interband transitions. However, in our case no direct interband transitions in Γ-L are possible so that the phonon-or magnon-assisted photoemission processes become significant in the near-threshold photoyield and, hence, for the MCD. The interpretation of MCD asymmetries in the light of direct interband transitions in other directions than Γ-L in conjunction with phonon-or magnon-mediated emission processes leads to

further conclusions to which we will refer in the following.
The calculations in Fig. 4.21 indicate that the existence of a real intermediate state in the 2PPE transition is of great importance for enhanced MCD asymmetries to occur. In model A the intermediate state can only be virtual, and we have no further information except that its mere existence should somehow cause a strongly enhanced 2PPE asymmetry. The resonant interband transition in model B, however, allows for qualitative conclusions: The excitation to a real intermediate state is not only favorable since the dipole matrix element between two real states is large, and the process will proceed very effectively. Also the enhanced lifetimes of real states cause a large mean free path of the electrons. This explains the large probing depth (bulk-sensitivity) and directly increases the possibility for an electron-phonon interaction. The importance of a real intermediate state is quantitatively reflected by the same energy dependence found in the calculations and the measurements and the absolute experimental and theoretical asymmetry values which are in the same order of magnitude. Thereby, we have to keep in mind that only the first excitation step has been calculated in the 2PPE case.
Besides, the difference between the measured asymmetries and the calculated values which occurs for 1PPE as well as for 2PPE could be due to a selection mechanism in the phonon-scattering process. In theory all k-directions are averaged equally. In the experiment scattering with lower momentum transfer is more probable than phonon-scattering with higher momentum transfer. This would be advantageous for k-vectors with higher projection onto the surface normal compared to those with low projection.
Furthermore, the calculations have shed new light onto the question why for the fcc Co-film the 2PPE asymmetries are six times larger than the 1PPE asymmetries, which is different from the case of Ni (100) [65]. For 1PPE the electron-phonon interaction must take place after the outright excitation of the electron into a real final state. For 2PPE the scattering process could happen either after the excitation to the real intermediate state or after the whole two step process. The first possibility would cause an increase in the electron-phonon scattering probability due to the enhanced lifetime of a real intermediate state. In this sense, time-resolved measurements would be interesting and helpful to investigate whether scattering already appears after the first excitation or whether the electron is firstly excited via the two step process to the final state before it interacts with a phonon. However, those experiments would require pulse widths in the few-fs range [11]. Measurements on flat and rough sample surfaces might answer the question whether phonon/magnon scattering processes mainly appear in the surface region where scattering most likely happens at stepped edges and point defects and is suppressed at almost perfectly ordered surfaces. In this context, photoemission measurements on Ag(111) related the *extra* emission intensity on the lower binding energy side of a direct transition peak to indirect transitions induced by the surface [19]. This is an explicit hint for phonon- or magnon-mediated photoemission. Phonon/magnon scattering in the bulk could be investigated by temperature-dependent measurements.
We finish this section with two final remarks: The analysis of the band-structure scheme allows some general conclusions considering the properties of the participating bands. For the employed band structure of fcc Co and the given photon energy range, the most relevant 2PPE transitions showing high MCD asymmetries can be found around the X-point. Though not

only the low index crystallographic directions contribute to the signal and k is integrated over the whole Brillouin zone, this observation suggests that transitions in the vicinity of high symmetry points in k-space might be favorable for large dichroic signals. Furthermore, the slope of the bands involved in the emission process might play a crucial role: Flat band regions like those of the initial bands 6 and 7 and the real intermediate bands 11 and 12 exhibit large densities of states and thus give rise to high partial intensities.
Finally, it is worth mentioning that the previous discussion has only been focused on fcc Co. A study on thin Co films on Pt(111) revealed that evaporating Co at room temperature results in an fcc-growth mode with enhanced stacking faults; the hcp-phase is produced only by evaporation at 120 K [97]. However, since Weller et al. detected a structural transition from fcc to hcp Co beginning at a thickness of 5 ML [76] which is close to our investigated film thickness of 4.5 ML we cannot completely exclude the presence of an hcp Co phase in our sample system. Therefore, we will also briefly discuss the band structure of hcp Co, which has recently been calculated by Grechnev et al. [98] using local density approximation (LDA) plus dynamical mean field theory (DMFT). In this approach hybridization effects have been neglected and the band structure is separated due to minority and majority spin states. For hcp Co the direction of normal electron emission is Γ-A.
In the minority channel electrons in Γ-A-direction are excited to evanescent final states for 1PPE and virtual intermediate/evanescent final states in the case of 2PPE; no direct band-to-band transitions are possible in the normal emission direction which is comparable to the situation with fcc Co. In contrast, for the majority channel direct transitions from real initial to real final states passing a virtual intermediate state in the case of 2PPE might be possible depending on the character of the initial and final states and the lifetime-broadening of the excited states. Neglecting lifetime-broadening the band-structure scheme suggests that a transition might only be open for the highest available photon energies of our experimentally probed range. Furthermore, the electrons can be excited only directly from the Fermi level E_{F} at the Γ-point. In addition, no real intermediate state is available for the case of 2PPE. These defined preconditions for the appearance of MCD in the Γ-A direction are incompatible with our 1PPE and 2PPE measurements only revealing a slight dependence on the photon-energy and yielding a much larger asymmetry for the 2PPE case. Of course, the influence of lifetime-broadening might play a crucial role and future MCD calculations on hcp Co should investigate whether lifetime-broadening softens the conditions for a direct interband transition in Γ-A and enables excitations following the picture of conventional photoemission. This would be an interesting alternative to the excitation mechanisms discussed above. However, without a massive influence of lifetime-broadening effects there is generally no indication that enlarged MCD asymmetries can be related to photoemission from the Γ-A direction of hcp Co. In this sense, the rather improbable case of an hcp Co structure would also have to be discussed in the framework of model B.

4.3.5 Summary and conclusions

Energy- and angle-dependent magnetic circular dichroism measurements for one- and two-photon photoemission have been carried out at a 4.5 ML Co film on Pt(111). The fourth and second harmonic of a fs-laser thereby served as photon source yielding hν = (5.06 - 5.84) eV and hν = (2.49 - 2.92) eV for 1PPE and 2PPE, respectively.
Photon-energy dependent measurements reveal maximum asymmetries directly at the photoemission threshold (1.9 $\%$ for 1PPE and 11.7 $\%$ for 2PPE) that weakly decrease with increasing photon energy. This proves that enhanced asymmetry values are directly connected with the absence of a capping layer and shows that enlarged dichroic signals are also possible for systems other than Ni/Cu(001).
A fully relativistic band structure calculation for fcc Co provides the basis for an interpretation of the magnetic asymmetries. In the direction of normal electron emission (i. e. Γ-L) electrons can only be excited to evanescent final states (passing a virtual intermediate state in the case of 2PPE). This is incompatible with the measured bulk-sensitivity of the MCD asymmetry (c. f. Ch.4.2). Therefore, the conventional model of direct interband transitions cannot be applied to near-threshold photoemission from fcc Co(111). Instead, we have treated the problem analogously to MOKE theory with the additional restriction in energy due to the existence of the sample work function in the photoemission process leading to a narrow energy interval of initial states. In this model all possible interband transitions in crystallographic directions different from Γ-L are considered, and the dichroic response is evaluated by averaging over all participating transitions in the whole BZ.
In the case of 1PPE the calculations are in reasonable agreement with the measured MCD responses which emphasizes that the origin of the (1PPE)-magneto-dichroic effect is the combined influence of the exchange splitting and spin-orbit interaction on single particle energy bands. For 2PPE, only the first excitation step could be simulated due to the lack of a real final state. Nevertheless, the simulations revealed agreement within a factor of two. The enlarged 2PPE asymmetry is attributed to the existence of real intermediate states, and its origin is traced back to specific transitions between defined initial and real intermediate states carrying enlarged single band-to-band asymmetries.
As the relevant transitions occur in crystallographic directions other than Γ-L additional momentum has to be supplied by a secondary process. We propose electron-phonon and/or electron-magnon scattering processes as assisting mechanisms. Future time-resolved measurements might answer the question whether the factor of 6 between the 1PPE and 2PPE asymmetries is possibly due to different electron-phonon- or magnon scattering probabilities for the two processes or whether it must be attributed to properties of the real intermediate state. Temperature-dependent experiments as well as measurements on flat and rough surfaces might yield information about the probabilities and the detailed mechanisms of phonon- or magnon-mediated processes in the bulk and in the surface region.
Measurements in dependence of the light incidence angle reveal a constant asymmetry in the case of 1PPE that might be explained by the presence of a second (Co/Pt) interface. For 2PPE the asymmetry decreases with increasing angle of incidence (53 $\%$ between $\vartheta = 0^\circ$ and

$\vartheta = 54°$). This behavior is attributed to a loss of circular polarization in bulk material with increasing angle of incidence and can be quantitatively modeled using the Fresnel formalism. In this case the second interface has no effect due to the equal refraction indices of Co and Pt. The measurements also demonstrate that large angles of incidence as used in standard photoemission electron microscopy setups are still sufficient to exploit huge dichroic effects as magnetic contrast mechanism.

In conclusion the measurements on Co films on Pt(111) demonstrate that a sizeable MCD occur even in cases where no special band structure features (e. g. a spin-orbit split band close to E_{F} in the case of Ni(001)) are present and even band-to-band transitions in conventional normal electron emission (Γ-L direction) are not possible. Unlike the case of Ni(001) [65], the asymmetry is almost energy-independent (i. e. not threshold-sensitive) and still large for photon energies 0.5 eV above the threshold with strongly enhanced electron intensities, so that a fine-tuning of the photon energy is not needed. Although explicitly demonstrated at the example of fcc Co(111), the present results give evidence that sizeable asymmetry values can be expected for many more materials. Finally, note that the large intensities connected with the absence of a rapid drop of asymmetry above threshold, are important for exploiting MCD as contrast mechanism in time-resolved imaging experiments (e. g. stroboscopic PEEM)

For detecting large asymmetry values in future experiments it would be advantageous to firstly inspect the band structure of suitable materials considering the available photon energy range, the work function and the crystallographic direction. With the knowledge of the present work, resonant transitions to real intermediate bands (in the case of 2PPE) or real final bands (in the case of 1PPE) would be promising candidates for large asymmetry signals. The transitions need not necessarily occur along the direction of observation, since phonon-or magnon scattering can provide the necessary momentum transfer in near-threshold yield experiments. The transitions should preferably be located in the vicinity of high symmetry points in k-space with participating bands carrying high density of states and predominantly one spin character. These criteria should allow for a direct tailoring of MCD asymmetries in near-threshold photoemission in future experiments.

4.4 Magnetic circular dichroism in near-threshold photoemission from an ultrathin Co/Pt(111) film at low work functions

4.4.1 Motivation

The conventional interpretation of photoemission spectra in the framework of direct interband transitions in the direction of normal electron emission cannot be applied in every case. This was for example shown by photoemission experiments on Ag(111) where an *extra* intensity occurs on the low binding energy shoulder of a direct band-to-band transition peak which was attributed to indirect transitions induced by the surface [19]. Our MCD measurements demonstrate that the conventional model of photoemission does not apply to the case of Co(111) in near-threshold photoemission. Instead, the MCD asymmetry is traced back to direct interband transitions in k-directions deviating from the direction of observation (Γ-L). The additional momentum needed for the electron to surmount the surface barrier after the photoexcitation is assumed to be provided by electron/phonon or electron/magnon scattering processes.
Calculations on the basis of this model predict asymmetries which are in reasonable agreement with the experimental results. For 2PPE, however, only the first excitation step could be simulated (assuming a sequential excitation scenario) so that the question remains whether both excitation steps contribute equally to the asymmetry or whether one of the steps is the major asymmetry-generating process. In order to gain further insight into this issue, we avoid the second excitation step of the 2PPE process investigated in Ch. 4.3 by lowering the work function slightly below the energy hν of the single photon used for the 2PPE transition. In this way we obtain a 1PPE process being equivalent to the first excitation step of the 2PPE process. This enables the comparison between the MCD of a one-step process and the MCD of the corresponding two-step process so that we gain immediate information about the influence of the first excitation step.
On the other hand the calculations as well as the experiments presented in Ch. 4.3 point out that the existence of a real intermediate state is important for obtaining large 2PPE-MCD asymmetries. In order to prove this idea, the 2PPE photon energy is adjusted in a way that excitations into real intermediate states are triggered at low work-function values. This enables measurements of the 2PPE MCD asymmetries which originate from different interband transitions than discussed in Ch. 4.3 and therefore reveals the influence of a real intermediate state independent of the energy range probed in the band-structure scheme.

4.4.2 Results

The preparation of the sample system is identical to the one presented in Ch. 4.3. Also LEED and polar MOKE are carried out in analogy to the description given in the previous chapter. The experimental setups used for the polar Kerr- and MCD-measurements are shown in Fig. 3.2 and Fig. 3.4, respectively. For 1PPE cw-laser light with a photon energy of hν = 3.06 eV (1.5 mW) is used. For 2PPE we utilize the first harmonic of a broadband ultrashort pulse laser ($\tau < 100$ fs, 80 MHz repetition rate) with photon energies in the range of

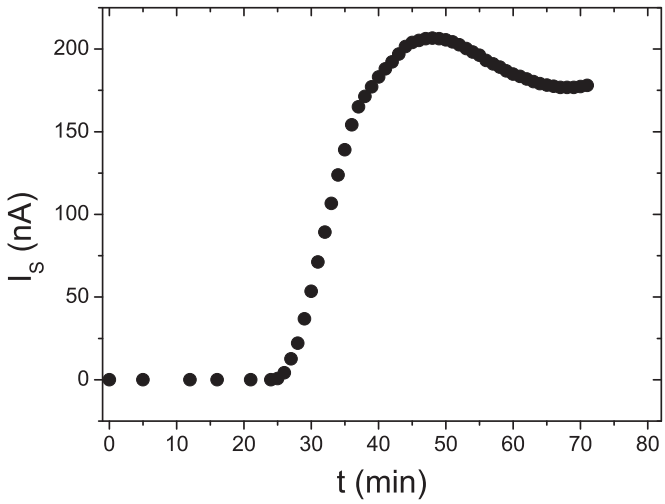

Figure 4.22: Dependence of the sample current on the Cs adsorption time for a 4.5 ML Co film on Pt(111) measured at hν = 3.06 eV.

hν = (1.53-1.66) eV. For the 2PPE process we additionally use a lens (f = 15 mm) with its focal point at the sample surface and an optical filter to cut off possible admixture of one-photon photoemission.
In order to lower the work function from $\sim$ 5.0 eV for clean Co/Pt(111), Cs is deposited onto the sample surface. Fig. 4.22 shows the dependence of the sample current at hν = 3.06 eV on the Cs exposure time. After 25 min the work function has decreased to the threshold value of 3.06 eV and emission sets in. The current signal increases and reaches a maximum value after 48 min of Cs dosage. This maximum corresponds to a work function minimum of 1.63 eV at 0.65 ML cesium coverage. These values are taken from measurements on Cs/W(110) [99], and in the following we assume that with respect to the sample work function both systems Cs/W(110) and Cs/Co(111) behave very similar. Further dosage leads to a rise of the work function visible in the drop of sample current. After 71 min of evaporation the Cs dosage is stopped. Referring to Ref. [99] a fully cesiated W(110) sample yields a work function in saturation of $\sim$ 2.11 eV. Prior to the MCD measurements the approximate value of the work function is checked by measuring the sample current with a photon energy of 1.95 eV. No current signal is measured which means that the work function is larger than 1.95 eV in agreement with Ref. [99].

1PPE measurements

To investigate the influence of the first excitation step in the 2PPE measurement presented in Ch. 4.3 which yields an asymmetry value of 8.37 % at a photon energy of 2hν = 2 $\times$ 2.92 eV = 5.84 eV and a sample work function Φ = 4.98 eV (c. f. Fig. 4.15 (b)), we try to map the first excitation step as a real 1PPE process. Therefore, the sample work function is reduced to a value

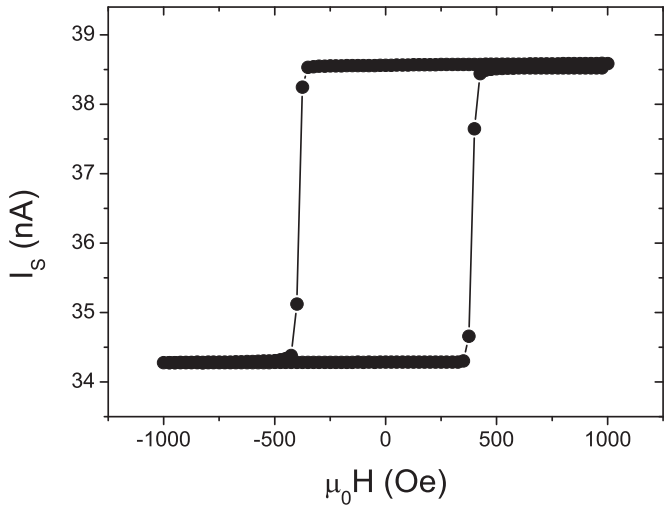

Figure 4.23: 1PPE MCD measurement (directly after Cs deposition) showing the sample current versus the external magnetic field at a photon energy of $h\nu = 3.06$ eV. The figure represents an average over 30 hysteresis loops; the error bars are of the order of the symbol size.

of $\Phi \sim \Phi_{2\mathrm{PPE}}/2 = 2.49$ eV by means of Cs adsorption, and an appropriate photon energy of $h\nu = 3.06$ eV (which is close to the value of 2.92 eV) is used.
Fig. 4.23 depicts a 1PPE MCD measurement directly after cesium adsorption for which 30 hysteresis loops are averaged. Each loop consists of 160 current readings. Since the magnetization easy axis and the external field are oriented normal to the sample plane (easy axis magnetization curves) the MCD asymmetry is evaluated using Eq. (4.12). This yields a value of 5.89 %.
With increasing time after Cs deposition the work function starts to increase from the saturation value of 2.11 eV due to a contamination by residual gas adsorption. A time dependent measurement thus enables detecting the 1PPE MCD asymmetry at a work function of $\Phi \sim 2.49$ eV. Furthermore, the general dependence of the asymmetry on a varying sample work function can be investigated. Within 320 min 626 asymmetry values are recorded. For each value one hysteresis loop is acquired, and the asymmetry is computed by using the sample currents in remanence. In order to display the dependence of the asymmetry on the excess energy $h\nu - \Phi$, the measurement time is translated to work-function values. For this conversion the dependence of the average sample current on the work function is derived from the initial Cs deposition experiment shown in Fig. 4.22 assuming a linear relation between coverage and deposition time and using the relation between coverage and work function known from Ref. [99]. Fig. 4.24 shows the dependence of the sample current and the asymmetry on the excess energy $h\nu - \Phi$. The sample current (a) increases continuously for both magnetization directions with decreasing work function. The asymmetry curve (b) shows a shallow linear

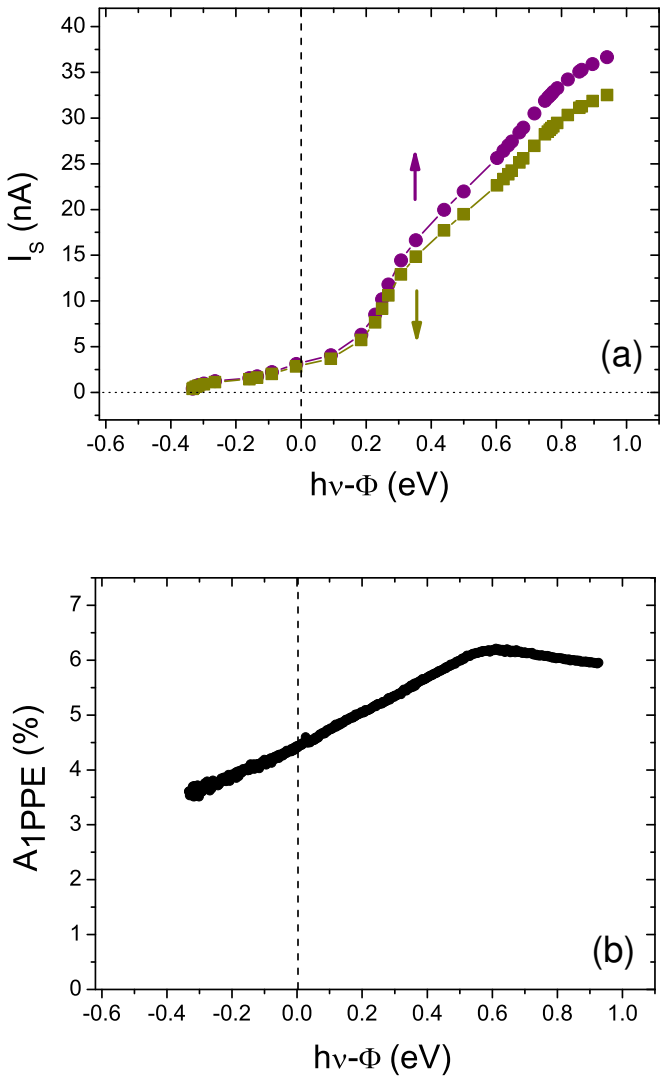

Figure 4.24: (a) Dependence of the sample current on the excess energy $h\nu - \Phi$ at $h\nu = 3.06$ eV for both magnetization directions. (b) Corresponding asymmetry curve. The dashed line denotes the photoemission threshold.

increase at low work functions until a maximum of 6.21 % is reached at hν - Φ = 0.61 eV. Here the slope changes sign and the asymmetry decreases to a value of 4.4 % at threshold (dashed line). The initial increase in asymmetry to the maximum is associated with particular electronic excitations most effectively triggered at Φ = 2.45 eV. This will be discussed in detail below. At the only slightly different work function of Φ = 2.49 eV an asymmetry of 6.17 % is reached. This enables a direct comparison to the mentioned 2PPE case and will be discussed later as well. Asymmetries below threshold, where hν is smaller than Φ (left hand side of the dashed line), have already been observed in the measurements presented in Ch. 4.3 and are attributed to finite temperature and photon energy broadening effects. Furthermore, an excitation of electrons below the macroscopic work function threshold due to local inhomogeneities of the surface cannot be exluded since the work function of such defects is locally reduced [100]. Finally, the increased statistical scatter in the asymmetry values below threshold is attributed to small sample currents in the low nA range in the sub-threshold region.

2PPE measurements

For the 2PPE experiments Cs is dosed on a freshly deposited Co film. After deposition no current signal is detected for photon energies lower than hν = 1.95 eV. Using ultrashort pulsed laser light and a focusing lens in close distance to the sample, the photon intensity is increased allowing for 2PPE processes. Now a sample current appears for a 2PPE energy exceeding 2hν = 3.06 eV. The work-function value can therefore be localized at $\Phi \approx 3$ eV.
To trigger excitations to real intermediate states different from those excited in the 2PPE measurement of the previous chapter we choose a photon energy of 2hν = 3.22 eV. This yields A_{2PPE} = 16.8 %. Fig. 4.25 (a) shows the corresponding MCD measurement for which 30 hysteresis loops are averaged. Each hysteresis loop consists of 240 current readings. In Fig. 4.25 (b) we depict the spectral variation of the 2PPE asymmetry in the energy range of 2hν = (3.06 - 3.31) eV. Unlike the 1PPE case, we find an almost constant asymmetry independent of the photon energy. An average value of about 17 % persists in the full photon energy range investigated.

4.4.3 Discussion

1PPE measurements

Unlike almost all cases studied so far, the MCD asymmetry of Co(111) increases with increasing excess energy in 1PPE. A prominent counterexample is Ni(100) where the asymmetry drops to zero within the first 600 meV above threshold. The 1PPE asymmetry curve in Fig. 4.24 (b), however, still reveals an asymmetry value of 5.95 % at an excess energy of 0.93 eV (implying a maximum binding energy of 0.93 eV). This is another proof that the MCD asymmetry in the case of Co(111) is not threshold-sensitive.
The results shown in Fig. 4.24 enable a direct comparison with the 2PPE measurement of Ch. 4.3. While for 2PPE an asymmetry of 8.37 % (hν = 2.92 eV, Φ = 4.98 eV) has been detected, the 1PPE measurement already yields a value of 6.17 % (hν = 3.06 eV, Φ = 4.98/2 =

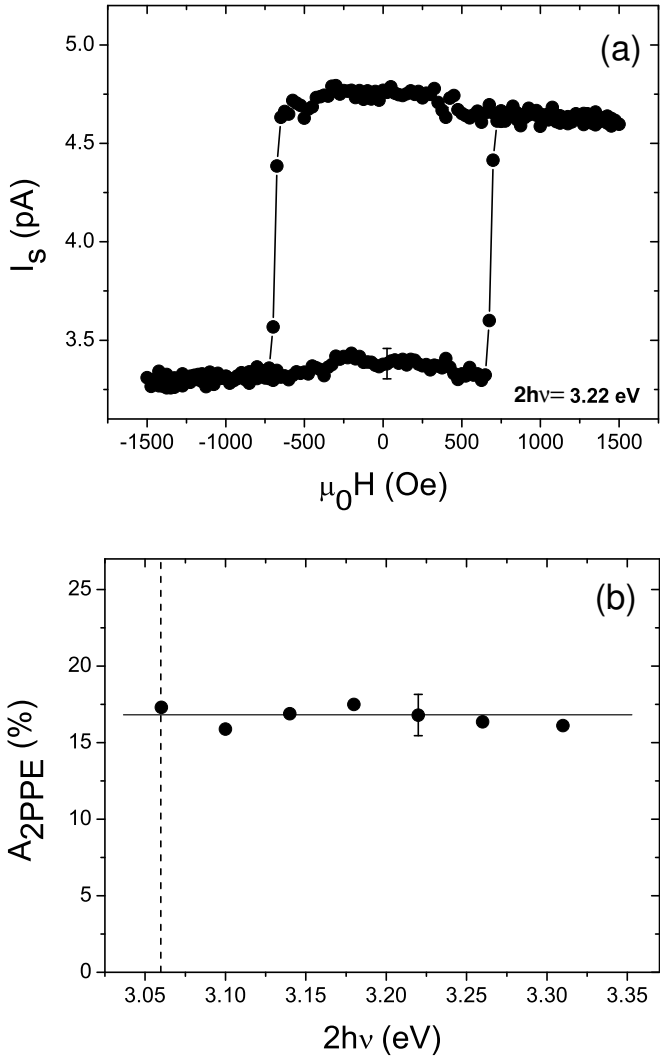

Figure 4.25: (a) 2PPE MCD measurement at 2hν = 3.22 eV. The figure represents an average over 30 hysteresis loops. A typical error bar that is mainly due to the detection of small sample currents is shown on the bottom branch. (b) Photon-energy dependence of the 2PPE MCD asymmetry. A characteristic error has been derived exemplary for 3.22 eV. The dashed line denotes the photoemission threshold (with an error of $\pm$ 0.1 eV).

2.49 eV) for the first excitation step which amounts to 74 % of the 2PPE asymmetry. This leads to the conclusion that the first excitation step is the dominant asymmetry-generating process. As expected, the value of 6.17 % (in comparison to 8.37 %) coincides better with the calculation for the first excitation step. The curve with lying triangles in Fig. 4.21 shows the MCD calculation for a 1PPE transition into a real final-state band. It predicts an asymmetry of ~ 2.5 % for hν = 3.06 eV. A possible reason for the remaining difference might be the fact that Fig. 4.24 is accompanied by several approximations concerning the determination of work-function values. Another reason might be attributed to a selection mechanism in the phonon-scattering process. In theory all k-directions are averaged equally. In reality phonon-scattering with lower momentum transfer is more probable than scattering with higher momentum transfer. As already mentioned in Ch. 4.3 this would favor k-vectors with larger projection onto the surface normal against those with a smaller one. Furthermore, the fact that the experimental as well as the calculated 1PPE asymmetries are smaller than those measured for 2PPE points out that enlarged asymmetries are only reached with two excitation steps passing an intermediate state. Gaining clearer insight into the characteristics of the intermediate states, their particular influence with respect to both excitation steps and the physics of the second excitation step would deliver fruitful information about the different mechanisms leading to the asymmetry values we observe in the experiment.

To interpret the origin and the behavior of the 1PPE MCD asymmetry in dependence of the excess energy it is worth analyzing possible excitation pathways within a spin-resolved band structure calculation for Co(111) in analogy to Ch. 4.3. Fig. 4.26 depicts the same energy band calculation as Fig. 4.18. Additionally the density of bars at each line marks the strength of the d-character of the particular bands ('fat band representation'). Again, dashed vertical arrows denote possible transitions for 1PPE and the full arrows indicate those for 2PPE. As usual, only the low index directions are shown. For 1PPE the accessible regime of final-state energies is marked as shaded area. For 2PPE the estimated work-function value (~ 3 eV) is marked by a dashed line. Following the previously discussed model of photoemission for Co(111) in the vicinity of the threshold we will look in particular for direct interband transitions to real final states in 1PPE (for 2PPE, we look for transitions to real intermediate states, as discussed below) in directions deviating from (Γ-L).

At Φ = 2.45 eV (maximum binding energy 0.61 eV) the 1PPE asymmetry shows a maximum value of 6.2 % indicating that particular transitions might be effectively triggered at that work-function value. This can also be recognized by analyzing the increase in asymmetry from 4.4 % at threshold to 6.2 % at hν - Φ = 0.61 eV. Increasing the binding energy from 0 to 0.61 eV implies the onset of several band-to-band transitions in the crystallographic directions Γ-X and Γ-K. In all possible transitions bands 11 and 12 serve as final states. While in Γ-K only band 9 serves as initial state, bands 6 and 7 are the appropriate initial states in the Γ-X direction. Here, all excitations take place in the vicinity of the high-symmetry X-point where the initial as well as the final states carry a high density of states promising high transition probabilities. Furthermore, the band-structure scheme indicates that the final bands 11 and 12 exhibit pure p-character directly at X while the initial states are d-states. This means that an excitation according to the dipole selection rules can most effectively be triggered in the vicinity of the

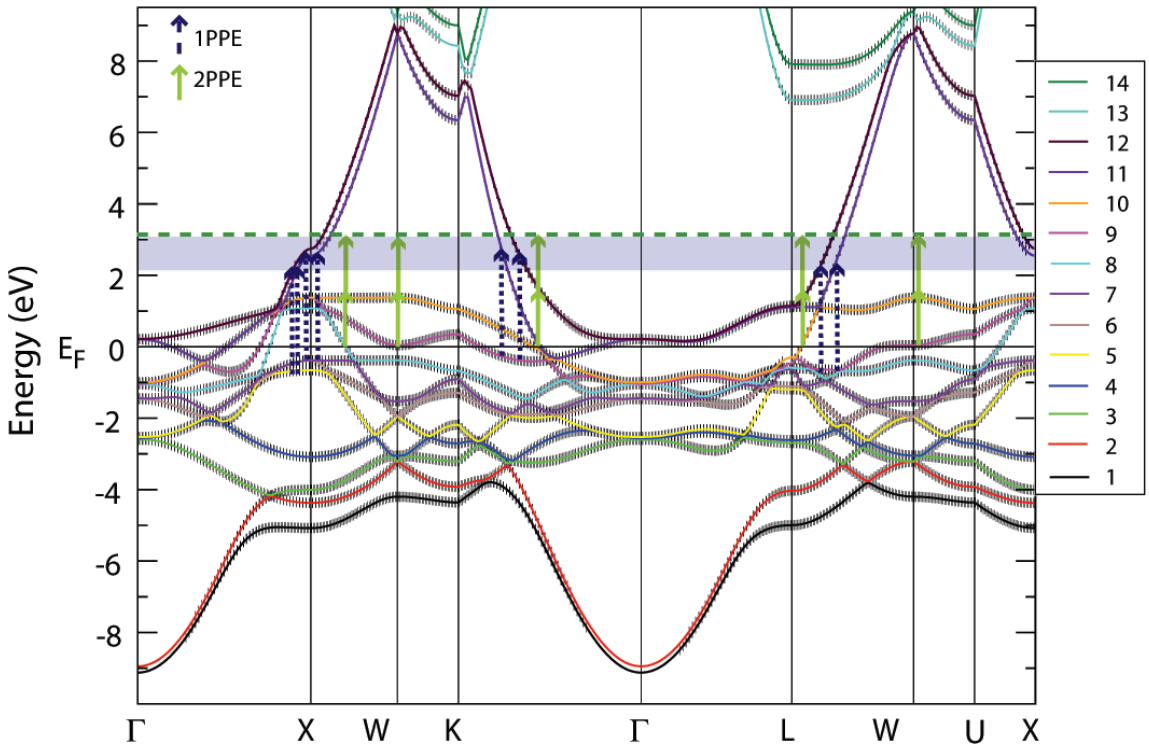

Figure 4.26: Relativistic band structure calculation for fcc Co (lattice constant a = 0.35457 nm) [101]. For each band the d-character is indicated over the whole Brillouin zone by small rods (i. e. a high density of rods reflects a pure d-character of the corresponding band). The dashed (continuous) arrows show possible 1PPE (2PPE) transitions in different crystallographic directions. The shaded area denotes the range in which the work function has been varied (2.13 - 3.06 eV) during the 1PPE measurement. The dashed line at 3 eV marks the estimated value of the vacuum level E_V.

X-point. At work-function values < 2.45 eV, further contributions from the initial bands 5 in Γ-X and 8 and 9 in L-W set in. These onsets might be the reason for the slight reduction of the 1PPE asymmetry to 5.95 % at a maximum binding energy of 0.93 eV.
In analogy to Fig. 4.19, Fig. 4.27 shows a spin-resolved calculation of the imaginary and real parts of the conductivities σ_{xy} and σ_{xx} for the 1PPE excitation as a function of photon energy [101]. The green curve gives the conductivity spectra due to majority-spin excitations, the red curve those due to minority-spin transitions. A work function of 2.0 eV and a typical lifetime-broadening of 0.4 eV of the final state are assumed. Fig. 4.27 approximately reflects the situation at the end of the experimentally-probed range with a highest excess energy of $h\nu - \Phi = 0.93$ eV in Fig. 4.24 (b). At a photon energy of $h\nu = 3.06$ eV the MCD-related terms

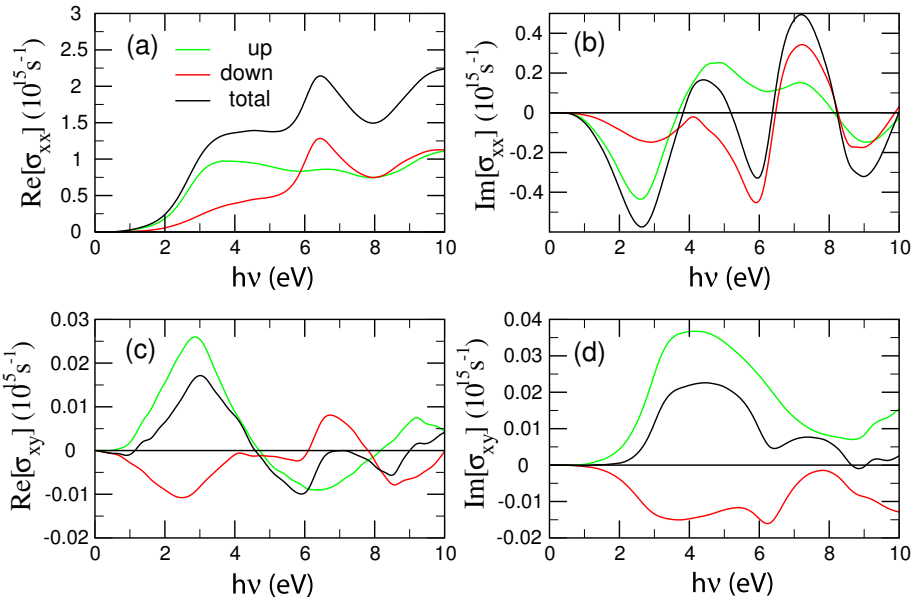

Figure 4.27: Calculated spin-resolved 1PPE optical conductivity spectra. Shown are the imaginary (b,d) and real (a,c) parts of σ_{xx} and σ_{xy} for 1PPE as a function of the photon energy. A work function of 2.0 eV and a lifetime broadening of 0.4 eV are assumed.

$Im[\sigma_{xy}]$ and $Re[\sigma_{xx}]$ already yield an asymmetry value of $A_{\mathrm{1PPE}} \approx 1.5\,\%$ using the crude approximation $A_{\mathrm{1PPE}} \approx \frac{Im[\sigma_{xy}]}{Re[\sigma_{xx}]}$. Furthermore, in both spectra the calculated curves for the total signal reveal a point of inflection which might be identified with the asymmetry maximum observed in the 1PPE measurement. However, this could only be proven by further calculations. Here, also a computed 1PPE MCD spectrum of single excitation channels would deliver precious information about the influence of single band-to-band transitions and the resulting averaged asymmetry signal. This could provide a microscopic explanation of the non-monotonous behavior of the 1PPE asymmetry with respect to the excess energy as a result of the onset of particular bands and their individual contributions.
Finally, note that for the above discussion lifetime broadening is ignored to simplify matter. In fact all excited real electronic states are lifetime-broadened and cannot be regarded as sharp lines. Therefore, also other interband transitions than the ones mentioned above might be involved. The importance of lifetime broadening becomes evident checking the origin of the 1PPE asymmetry directly at threshold: as shown in the band-structure scheme no band crosses the Fermi level in regions where an excitation to a real final state is possible. Only by including a typical lifetime-broadening of 0.4 eV excitations become feasible.

2PPE measurements

In order to gain more information about the role of the real intermediate state in a two step process, 2PPE measurements are carried out for a different photon energy range ($2h\nu$ = (3.06 - 3.31) eV) as compared to Ch. 4.3. The measurements yield an almost constant asymmetry of 17 %, which is larger than the 2PPE asymmetry (8 - 12 %) for $2h\nu$ = (4.92 - 5.84) eV. Assuming 3 eV as the lowest limit for the work-function value electrons can stem from initial bands with a maximum binding energy of 0.31 eV. In analogy to the 1PPE measurement the enlarged asymmetry values might be explained by direct transitions along crystallographic directions other than Γ-L. Here, photon energies in the range of (1.53 - 1.66) eV are expected to connect initial states with real intermediate states. Referring to the band-structure scheme the final states of these two step processes are evanescent. This is comparable to the 2PPE measurement in Ch. 4.3. However, since the used photon energies are different, completely other transitions are triggered resulting in different asymmetry values.
Directly at the Fermi level electrons can be excited in four low-index crystallographic directions, X-W, Γ-K, L-W, and W-U as shown in Fig. 4.26. Besides the transition $8 \rightarrow 10$ in X-W direction, the transition $9 \rightarrow 10$ might be of particular interest since it takes place directly at the W-point, and initial as well as intermediate states carry a high density of states associated with large transition probabilities. However, one should keep in mind that in addition to the energy conservation the dipole selection rules have to be respected. In this context, the excitation from band 9 to band 10 might be suppressed or at least strongly reduced since both bands carry strong d-character directly at the W-point (c. f. Fig. 4.26). In the Γ-K direction bands 10 and 11 are the appropriate initial and band 12 is the adequate real intermediate state. Additionally, a transition from band 10 to 12 exists in L-W direction. Since it takes place in the vicinity of L where band 10 exhibits p- and band 12 carries d-character, this transition could also be

a candidate for enlarged MCD asymmetries. Furthermore, the vicinity to the high-symmetry point L favors the excitation and could even enable a direct transition in the normal emission direction Γ-L without the participation of scattering processes. All mentioned transitions directly set in at the threshold and still contribute at the maximum binding energy of 0.31 eV due to lifetime-broadening. This is also reflected by the constant behavior of the 2PPE MCD asymmetry. In summary, the present 2PPE measurement proves that excitations into real intermediate states lead to enhanced 2PPE asymmetries independent of the probed energy region in the band-structure scheme. Further statements concerning the influence of the second excitation step are not possible as long as evanescent states are involved which cannot be described by our theoretical approach. This inhibits a direct comparison between experiment and theory in the case of 2PPE.

Finally, we add two general remarks: With respect to a possible hcp Co phase we will shortly discuss the appropriate band-structure scheme for the present measurements. Based on the band-structure calculations of Ref. [98], in the case of 1PPE electrons can only be excited into evanescent final states in the majority- as well as in the minority-spin channel in the direction of normal electron emission Γ-A. This is comparable to the situation of fcc Co, and the enlarged 1PPE asymmetries can also not be explained via the conventional model of photoemission. The same holds for the energy-dependent 2PPE measurements where transitions in the majority- and the minority band structure lead to virtual intermediate and evanescent final states in Γ-A. Therefore, in the case of hcp Co the enhanced asymmetry values for 1PPE and 2PPE can also only be explained by direct interband transitions in directions deviating from (Γ-A). Irrespective of the measured bulk-sensitivity of the asymmetry which demands participating intermediate or final states to stem from the Co bulk band structure, the Cs coverage on the Co sample additionally inhibits excitations to evanescent states. The application of the conventional model of photoemission is therefore categorically ruled out for the fcc as well as the hcp structure of cesiated ultrathin Co films. This is another strong argument for phonon- or magnon-mediated photoexcitation from various k-directions.

From a general point of view it is worth mentioning that MCD measurements under variation of the photon energy do not directly correspond to experiments under variation of the sample work function. In both experimental setups a particular asymmetry is reached directly at threshold. With each increase in photon energy the length of the arrows connecting initial and final states in the transition scheme becomes larger while the vacuum level stays fixed. Therefore, with each change of the photon energy the possible asymmetry generating transitions differ from each other, so that the asymmetry values in dependence of the photon energy arise from *energy-selective* electronic excitations. Of course, these considerations only hold if lifetime broadening is neglected. For experiments under variation of the work function the situation is different. Lowering the work function from the threshold value ($\Phi = h\nu$) at a fixed photon energy leads to an opening of more and more electronic excitation channels. This is also the reason for the increase of the 1PPE asymmetry from $\Phi = 3.06$ eV to its maximum at $\Phi = 2.45$ eV. Note that the existence of lifetime broadening weakens the instantaneous onset of new channels. In this context the theoretical calculations for the two Heusler systems in Ch. 4.1 also demonstrate that a variation of photon energy compared to a variation of work

function leads to different MCD values.

4.4.4 Summary and conclusions

Magnetic circular dichroism for one- and two-photon photoemission in the vicinity of the Fermi level has been investigated for a 4.5 ML fcc Co/Pt(111) sample under wide-range variation of the sample work function in the case of 1PPE and variation of the photon energy at low work function for 2PPE.
In the 1PPE case ($h\nu = 3.06$ eV) the asymmetry values reveal a non-monotonous behavior in dependence of the excess energy $h\nu$-Φ. Unlike the Ni(100) case [9] the asymmetry increases with increasing excess energy from its threshold value of 4.4 % to a kink-like maximum of 6.2 % at $h\nu$-Φ = 0.61 eV, followed by a shallow drop to 5.95 %. The 1PPE result is traced back to direct interband transitions in k-directions other than the direction of observation (Γ-L) following a model introduced in Ch. 4.3. Ab initio calculations of the MCD are performed adopting this model and yield a first approximation of the average asymmetry ($A_{1\mathrm{PPE}} = 1.5\,\%$ at $h\nu = 3.06$ eV) which is of the same order of magnitude as the measured signal. The 1PPE result furthermore enables a statement concerning the influence of the first excitation step in a 2PPE process. Since it maps the first excitation process of a previous 2PPE measurement, we can conclude that exciting an electron from a populated intermediate state to a final evanescent state in a 2PPE transition (assuming sequential excitation) further increases the asymmetry from 6.2 % to 8.3 % [95]. This observation suggests a major contribution from the first excitation step to the asymmetry. Larger asymmetry values only seem to be reachable by means of a real intermediate state and a second excitation step.
To sustain this assumption 2PPE measurements in a different photon energy range ($2h\nu = 3.06$-3.31 eV) compared to the experiments in Ch. 4.3 are carried out. Energy-dependent measurements at decreased work function yield a constant asymmetry with a maximum value of about 17 %. The enlarged asymmetry values can again be explained by direct interband transitions in crystallographic directions other than Γ-L. Since this measurement also yields an enhanced 2PPE asymmetry, one can conclude that at least for the case of Co(111) the existence of a real intermediate state and a second excitation causes an enhancement of the asymmetry independent of the probed energy range in the band-structure scheme.
The origin of the enhancement of the 2PPE signal with respect to the 1PPE case can also be related to different selection rules for 1PPE and 2PPE. While for 1PPE the parity is changed in the excitation process it does not change in the case of 2PPE. Principal differences between 1,2 and 3PPE processes also show up in spin-resolved measurements as discussed by Winkelmann et al.[102, 103, 104]. Additionally we notice that the asymmetry increases by decreasing the available binding energy range. This observation cannot be generalized since only two measurements have been carried out so far, and the enhanced asymmetry values could also be associated with particular band structure features.

5 Summary and outlook

In this work magnetic circular dichroism (MCD) is investigated in the regime of near-threshold photoemission, where the photon energy is just slightly larger than the sample work function. For Heusler alloys as well as ultrathin Co films MCD is analyzed for one-photon photoemission (1PPE) as well as for two-photon photoemission (2PPE) by using ultrashort pulsed laser light.

After the first experimental proof of enhanced 1PPE MCD asymmetries ($\geq 10\%$) for a perpendicularly magnetized Ni/Cu(001) film in near-threshold photoemission [9] the question occured whether MCD is also observable in the multi-photon photoemission regime close to threshold. In Ch. 4.1 of this work we present measurements on two ferromagnetic Heusler alloys that provide first evidence of magnetic circular dichroism in two-photon photoemission. For Ni_2MnGa and Co_2FeSi MCD asymmetries of $A_{2PPE} = (3.5 \pm 0.5) \cdot 10^{-3}$ and $A_{2PPE} = (2.1 \pm 1.0) \cdot 10^{-3}$ are obtained at a photon energy of $h\nu = 3.1$ eV. Besides the experimental results a first theoretical explanation based on relativistic energy-band theory in combination with linear-response theory is given.

The experimental findings of 1PPE and 2PPE MCD in near-threshold photoemission provide a basis for systematic investigations concerning general properties of MCD in single and multi-photon photoemission and motivate the search for an adequate theoretical description of MCD in the vicinity of the threshold.
Firstly, we investigate the dependence of the MCD asymmetry on the film thickness for a Pt-capped wedged Co sample grown on Pt(111)/W(110) by means of magneto-optical Kerr (MOKE) and near-threshold MCD measurements. This does not only yield information about the influence of the Co thickness, but also about the effects of the magnetic anisotropy and a capping layer on the MCD asymmetries. The corresponding results are presented in Ch. 4.2.
At a Co film thickness of 5 ML we find asymmetry values of 0.07 % for 1PPE ($h\nu = 4.64$ eV) and 0.11 % for 2PPE ($h\nu = 3.1$ eV), which are of the same order of magnitude as those of the capped Heusler alloys but ~ 100 times smaller than asymmetries measured for uncapped Ni(001) films [9]. This points out that an additional capping layer reduces the MCD asymmetries.
The key result shining light on the nature of the dichroism is found investigating the dependence of the asymmetry on the thickness of the magnetic film. For 1PPE as well as for 2PPE the MCD asymmetry increases continuously with the film thickness. This behavior reflects a bulk-sensitivity of the MCD asymmetry for the case of Co. The basic mechanism leading to near-threshold MCD must therefore be related to Co bulk properties; surface effects do not play a crucial role. The steady increase in asymmetry furthermore shows that the spin-reorientation transition (SRT) of the system does not visibly affect the MCD asymmetries.

Apparently, the magnetic anisotropy defining the direction of the magnetization easy axis does not influence the MCD asymmetry of the perpendicularly magnetized film. The experiments moreover reveal the information depth of the magnetic dichroic signals to lie between 1.6 and 9 nm.
In view of a possible theoretical description of MCD in near-threshold photoemission its connection to the related magneto-optical Kerr effect is finally investigated. As MCD and MOKE are based on the same microscopic mechanisms a description of the MCD asymmetry by the polar Kerr ellipticity in the framework of a Jones matrix formalism would be a straightforward and handy tool for the prediction of MCD asymmetries. However, a comparison of the thickness-dependence of the near-threshold MCD asymmetry and measured as well as calculated Kerr ellipticities shows that such a description of MCD is not adequate.

In order to investigate enhanced MCD effects in dependence of the photon energy as well as of the angle of light incidence we grow uncapped ultrathin Co films. Ch. 4.3 depicts the results for a 4.5 ML Co film grown on Pt(111).
Photon-energy dependent measurements reveal maximum asymmetries at the threshold of 1.9 % for 1PPE ($h\nu$ =5.23 eV) and 11.7 % for 2PPE ($h\nu$ =2.49 eV). This proves that enhanced asymmetries are related to the absence of a capping layer and demonstrate that enlarged dichroic signals are also possible for systems other than Ni/Cu(001). For both cases the MCD asymmetry is almost energy-independent, i. e. it is not threshold-sensitive, so that a fine-tuning of the photon energy is not needed.
Measurements in dependence of the light incidence angle reveal a decrease in asymmetry with increasing angle of incidence in the case of 2PPE. This behavior is attributed to a loss of circular polarization in bulk material with increasing angle of incidence and is simulated by using a Fresnel-field approximation. For 1PPE a constant asymmetry is detected which is explained by the influence of the second (Co/Pt) interface. The angle-dependent measurements moreover demonstrate that large angles of incidence as used in standard photoemission microscopy setups are still sufficient to exploit huge dichroic effects as magnetic contrast mechanism.
Since simulations on the basis of spin-resolved band-structure calculations in combination with linear response theory seem to be promising for a quantitative analysis of the magnetic dichroic signals (c. f. Ch. 4.1), we furthermore use this formalism to explain the MCD asymmetries for Co/Pt(111) in near-threshold photoemission. The analysis of the fcc Co band-structure scheme reveals that in the direction of normal electron emission (i. e. Γ-L) electrons can only be excited to evanescent final states passing a virtual intermediate state in the case of 2PPE. The excitation to evanescent states, however, is at variance with the measured bulk-sensitivity of the asymmetry (c. f. Ch. 4.2). Therefore, the conventional photoemission model of direct interband transitions in the direction of normal electron emission cannot be applied to the case of Co(111). As a consequence, we propose to consider band-to-band transitions in crystallographic directions different from Γ-L. Analogously to MOKE-theory the dichroic response is then obtained by averaging over all participating transitions in the whole Brillouin zone, and additionally considering that only a narrow energy interval of initial states contribute to the MCD signal due to the existence of the sample work function in the photoemission pro-

cess. As the electrons are excited in directions other than Γ-L additional momentum has to be supplied by a secondary process to enable the electrons to surmount the surface barrier after photoexcitation. We propose electron-phonon and/or electron-magnon scattering as assisting mechanisms. For 1PPE as well as for 2PPE the calculations on basis of this model are in reasonable agreement with the experimental results (for 2PPE only the first excitation step can be simulated), indicating that the chosen theoretical approach constitutes an adequate description of near-threshold MCD. Furthermore, the calculations demonstrate that the origin of the magneto-dichroic effect is indeed given by the combined influence of the exchange splitting and the spin-orbit coupling. Finally, with calculations in a band-resolved mode the enhanced 2PPE asymmetries are traced back to specific band-to-band transitions contributing with large single-transition asymmetries and the existence of a real intermediate state.

1PPE and 2PPE measurements do not only deliver the corresponding MCD asymmetry values but also give insights into the excitation process from initial to final states in the case of 1PPE as well as the two excitation steps and the intermediate state involved in a 2PPE process. In this context, the question occurs whether both excitation steps of a 2PPE process equally contribute to the asymmetry or whether one of the steps is the major asymmetry generating process.
To investigate this issue we experimentally avoid the second excitation step of the 2PPE process by lowering the work function of the material. In this way, we obtain a 1PPE excitation into a real final-state band whose MCD asymmetry can be directly compared to the MCD signal of the corresponding two-step process. The appropriate measurement on a cesiated 4.5 ML Co film on Pt(111) is presented in Ch. 4.4 of this work. Since it reveals an asymmetry of already $A_{\text{first step}} = 6.2\,\%$ for the first step which is 74 % of the whole two-step process ($A_{\text{both steps}} = 8.3\,\%$) it suggests a major contribution to the asymmetry from the first excitation step. The result likewise supports the previous assumption that asymmetry values larger than those obtained in a 1PPE process might only be available through the existence of a real intermediate state and a second excitation step. This is confirmed by an energy-dependent 2PPE measurement (hν =1.53 - 1.66 eV) at decreased work function ($\Phi \sim 3$ eV) where excitations to real intermediate states are triggered for a different photon energy compared to the 2PPE measurements in Ch. 4.3. The observed MCD asymmetries reach 17 %. Therefore, we conclude that the existence of a real intermediate state and a second excitation step cause an enhancement of asymmetry independent of the probed energy range in the band-structure scheme. For 1PPE as well as for 2PPE measurements the asymmetry values are again traced back to direct interband transitions in k-directions other than Γ-L following the model introduced in Ch. 4.3.

The above findings demonstrate that enlarged 1PPE and 2PPE-MCD effects in near-threshold photoemission occur for Co/Pt(111) films. Furthermore, an explanation of the MCD signal in terms of phonon- or magnon-mediated emission processes following photoexcitation in other directions than Γ-L is provided. This interpretation opens the way for different future perspectives: Up to now the assumed assisting mechanism of phonon/magnon-scattering is only scarcely investigated [19]. A key experiment might be the measurement of the temperature

dependence because phonon-scattering in the bulk is temperature-dependent. Measurements on flat and rough surfaces could yield precious information about the occurrence and the influence of such scattering processes in the surface region. In addition, time-resolved measurements could investigate whether scattering with a phonon or magnon predominantly appears after the first excitation of a 2PPE process or whether the electron is firstly excited to the final state before it interacts with a phonon. This could provide an explanation for the remarkable difference in 1PPE and 2PPE asymmetries. Furthermore, it would allow for a microscopic insight into the time relation between the phonon-or magnon-mediated emission process and the electronic excitations initiated by the incoming photons.

Moreover, our experiments point out that fundamental questions especially arise investigating MCD in the multi-photon photoemission regime. For 2PPE detailed characteristics of the second excitation step are scarcely investigated. Above all, it is still unclear whether a 2PPE process is predominantly marked by an instantaneous, coherent two step process or by a sequence of two independent processes. Our MCD calculations for Co(111) suggest that a sequential process might be more probable. However, in other cases both mechanisms could also contribute equally and could strongly depend on the investigated material. Additionally the role of parity conservation during the two step process has not been investigated up to now. All these questions are strongly related to the characteristics of the excited intermediate state and can only be treated by a precise investigation of its properties. An elegant access to the physics of the excited intermediate state is provided by $all\ optical\ pump-probe\ experiments$ using ultrashort laser pulses. In this approach, the electron is optically excited by a first pump pulse to an intermediate state. A second laser pulse which is delayed with respect to the first one finally probes the excited state. In this way the magnetization dynamics after the optical excitation can be investigated [105, 106]. Applying this technique to our experimental setup would also provide insight into the magnetization dynamics of ferromagnetic films in MCD measurements near the threshold. However, with the knowledge of the present work we cannot only expect information about the dynamical behavior of the entity of triggered intermediate states in threshold photoemission. Most strikingly, an observation of magnetization dynamics on a microscopic level might be attainable by selecting single interband transitions leading to single intermediate states. This is not only possible since a restricted range of initial states contribute to the signal in near-threshold photoemission. Also the fixed circular polarization used in the MCD experiments serves as an additional selection mechanism. Additionally implementing this technique in the context of photoemission electron microscopy (PEEM) would enable a real time imaging of magnetization dynamics of single excited states in a ferromagnetic material on a femtosecond timescale.

List of Used Abbreviations

ARUPS	Angle-Resolved Ultraviolet Photoelectron Spectroscopy
BZ	Brillouin Zone
DFT	Desity Functional Theory
DMFT	Dynamical Mean Field Theory
LDA	Local Density Approximation
LEED	Low Energy Electron Diffraction
LSDA	Local Spin Density Approximation
MCD	Magnetic Circular Dichroism
MLD	Magnetic Linear Dichroism
MOKE	Magneto-Optical Kerr Effect
1PPE	One-Photon Photoemission
PEEM	Photoemission Electron Microscopy
PMOKE	Polar Magneto-optical Kerr Effect
SOC	Spin-Orbit Coupling
SRT	Spin-Reorientation Transition
TiSa	Titan-Sapphire
2PPE	Two-Photon Photoemission
UHV	Ultra High Vacuum
UPS	Ultraviolet Photoelectron Spectroscopy
XMCD	X-ray Magnetic Circular Dichroism
XMLD	X-ray Magnetic Linear Dichroism

List of Figures

Bibliography

[1] V. Sharma, M. Crne, J. O. Park, M. Srinivasarao, Science **325**, 449 (2009).

[2] G. Schütz, W. Wagner, W. Wilhelm, P. Kienle, R. Zeller, R. Frahm, and G. Materlik, Phys. Rev. Lett. **58**, 737 (1987).

[3] P. Carra, B. T. Thole, M. Altarelli, and X. Wang, Phys. Rev. Lett. **70**, 694 (1993).

[4] J. Stöhr, J. Magn. Magn. Mater. **200**, 470 (1999).

[5] A. Krasyuk, F. Wegelin, S. A. Nepijko, H. J. Elmers, and G. Schönhense, Phys. Rev. Lett. **95**, 207201 (2005).

[6] W. Kuch, A. Dittschar, M. Salvietti, M.-T. Lin, M. Zharnikov, C. M. Schneider, J. Camarero, J. J. de Miguel, R. Miranda, and J. Kirschner, Phys. Rev. B **57**, 5340 (1998).

[7] W. Kuch, A. Dittschar, K. Meinel, M. Zharnikov, C. M. Schneider, J. Kirschner, J. Henk, and R. Feder, Phys. Rev. B **53**, 11621 (1996).

[8] G. K. L. Marx, H. J. Elmers, and G. Schönhense, Phys. Rev. Lett. **84**, 5888 (2000).

[9] T. Nakagawa and T. Yokoyama, Phys. Rev. Lett. **96**, 237402 (2006).

[10] A. Einstein, Ann. Phys. **17**, 132 (1905).

[11] M. Aeschlimann, M. Bauer, S. Pawlik, W. Weber, R. Burgermeister, D. Oberli, and H. C. Siegmann, Phys. Rev. Lett. **79**, 5158 (1997).

[12] M. Bauer and M. Aeschlimann, J. Electron Spectrosc. Relat. Phenom. **124**, 225 (2002).

[13] M. Cinchetti, PhD thesis, Johannes Gutenberg Universität Mainz, Germany (2004).

[14] M. P. Seah and W. A. Dench, Surf. Interf. Anal. **1**, 2 (1979).

[15] S. Hüfner, *Photoelectron Spectroscopy* (Springer, Berlin, 2003), 3rd edition.

[16] C. N. Berglund and W. E. Spicer, Phys. Rev. Lett. **136**, 1030A and 1044A (1964).

[17] J. Garbe and J. Kirschner, Phys. Rev. B **39**, 9859 (1989).

[18] C. M. Schneider, M. S. Hammond, P. Schuster, A. Cebollada, R. Miranda, and J. Kirschner, Phys. Rev. B **44**, 12066 (1991).

[19] T. Miller, W. E. Mc Mahon, and T. C. Chiang, Phys. Rev. Lett. **77**, 1167 (1996).

[20] D. Claesson, S. A. Lundgren, L. Wallden, and T. C. Chiang, Phys. Rev. Lett. **82**, 1740 (1999).

[21] S. R. Barman and K. Horn, Appl. Phys. A **69**, 519 (1999).

[22] S. R. Barman, C. Biswas, and K. Horn, Phys. Rev. B **69**, 045413 (2004).

[23] P. J. Feibelmann and D. E. Eastman, Phys. Rev. B **10**, 4932 (1974).

[24] G. D. Mahan, Phys. Rev. B **2**, 4334 (1970).

[25] H. Ebert and Ya. Perlov, in *Vorlesungsskripte des 30. Ferienkurses des Instituts für Festkörperforschung 1999 - Magnetische Schichtsysteme*,
(Research Center Jülich GmbH, Jülich, 1999), Vol. 2, p. C5.1-C5.24.

[26] W. Kuch and C. M. Schneider, Rep. Prog. Phys. **64**, 147 (2001).

[27] C. M. Schneider, PhD thesis, Freie Universität Berlin, Germany (1990).

[28] W. Eberhardt and F. J. Himpsel, Phys. Rev. B **21**, 5572 (1980).

[29] G. Borstel, M. Neumann, and M. Wöhlecke, Phys. Rev. B **23**, 3121 (1981).

[30] M. Pickel, A. B. Schmidt, F. Giesen, J. Braun, J. Minár, H. Ebert, M. Donath, and M. Weinelt, Phys. Rev. Lett. **101**, 066402 (2008).

[31] J. Hermanson, Solid State Commun. **22**, 9 (1977).

[32] H. Przybylski, A. Baalmann, G. Borstel, and N. Neumann, Phys. Rev. B **27**, 6669 (1983).

[33] J. Henk, T. Scheunemann, S. V. Halilov, and R. Feder, J. Phys.:Condens. Matter **8**, 47 (1996).

[34] R. Feder in *Polarized electrons in surface physics*,
(World Scientific, Singapore, 1985), Ch. 4.5.

[35] P. Hohenberg and W. Kohn, Phys. Rev. **136**, B864 (1964).

[36] W. Kohn and L. Sham, Phys. Rev. **140**, A1133 (1965).

[37] P. M. Opppeneer, private communication, (2010).

[38] P. M. Oppeneer, in *Handbook of Magnetic Materials*, (Elsevier, Amsterdam, 2001), Vol. 13, p. 229-422.

[39] R. Kubo, Can. J. Phys. **34**, 1274 (1956).

[40] R. Kubo, J. Phys. Soc. Jpn. **12**, 570 (1957).

[41] H. S. Bennett and E. A. Stern, Phys. Rev. **137** (1965).

[42] H. A. Kramers, Nature (London) **117**, 775 (1926).

[43] R. de L. Kronig, J. Opt. Soc. Am. **12**, 547 (1926).

[44] P. M. Oppeneer, T. Maurer, J. Sticht, and J. Kübler, Phys. Rev. B **45**, 10924 (1992).

[45] K. Hild, Diploma thesis, Johannes Gutenberg Universität Mainz, Germany (2007).

[46] J. Kerr, Phil. Mag. **3**, 321 (1877).

[47] H. R. Hulme, Proc. Roy. Soc. A **135**, 237 (1932).

[48] P. N. Argyres, Phys. Rev. **97**, 334 (1995).

[49] H. Ebert, Rep. Prog. Phys. **59**, 1665 (1996).

[50] H. Hornauer, T. M. Atmono, and K. Röll, J. Magn. Magn. Mater. **83**, 551 (1990).

[51] F. Heusler, Verhandlungen der Deutschen Physikalischen Gesellschaft **5**, 219 (1903).

[52] P. J. Webster and K. R. A. Ziebeck, J. Phys. Chem. Solids **34**, 1647 (1973).

[53] R. A. de Groot, F. M. Mueller, P. G. van Engen, and K. H. J. Buschow, Phys. Rev. Lett. **50**, 2024 (1983).

[54] I. Galanakis, P. H. Dederichs, and N. Papanikolaou, Phys. Rev. B **66**, 174429 (2002).

[55] C. Felser, G. H. Fecher, and B. Balke, Angew. Chem. Int. Ed. **46**, 668 (2007).

[56] I. Žutić, J. Fabian, and S. Das Sarma, Rev. Mod. Phys. **76**, 323 (2004).

[57] S. Chadov, X. Qi, J. Kübler, G. H. Fecher, C. Felser, and S. C. Zhang, Nat. Mater **9**, 541 (2010).

[58] G. Jakob and H. J. Elmers, J. Magn. Magn. Mater. **310**, 2779 (2007).

[59] H. Schneider, G. Jakob, M. Kallmayer, H. J. Elmers, M. Chinchetti, B. Balke, S. Wurmehl, C. Felser, M. Aeschlimann, and H. Adrian, Phys. Rev. B **74**, 174426 (2006).

[60] P. M. Oppeneer and A. Liebsch, J. Phys. Condens. Matter **16**, 5519 (2004).

[61] K. Hild, J. Maul, G. Schönhense, H. J. Elmers, M. Amft, and P. M. Oppeneer, Phys. Rev. Lett. **102**, 057207 (2009).

[62] G. K. L. Marx, P. O. Jubert, A. Bischof, and R. Allenspach, Appl. Phys. Lett. **83**, 2925 (2003).

[63] T. Nakagawa, T. Yokoyama, T. Hosaka, and M Katoh, Rev. Sci. Instrum. **78**, 023907 (2007).

[64] T. Yokoyama, T. Nakagawa, and Y. Takagi, Int. Rev. Phys. Chem. **27**, 449 (2008).

[65] T. Nakagawa, I. Yamamoto, Y. Takagi, K. Watanabe, Y. Matsumoto, and T. Yokoyama, Phys. Rev. B **79**, 172404 (2009).

[66] C. T. Chiang, A. Winkelmann, P. Yu, and J. Kirschner, Phys. Rev. Lett. **103**, 077601 (2009).

[67] K. Hild, J. Maul, T. Meng, M. Kallmayer, G. Schönhense, H. J. Elmers, R. Ramos, S. K. Arora, and I. V. Shvets, J. Phys.: Condens. Matter **20**, 235218 (2008).

[68] P. M. Oppeneer, J. Sticht, T. Maurer, and J. Kübler, Z. Phys. B: Condens. Matter **88**, 309 (1992).

[69] J. Kołaczkiewicz and E. Bauer, Surf. Sci. **314**, 221 (1994).

[70] E. Bauer, Appl. Surf. Sci. **11/12**, 479 (1982).

[71] M. T. Lin, H. Y. Her, Y. E. Wu, C. S. Shern, J. W. Ho, C. C. Kuo, and H. L. Huang, J. Magn. Magn. Mater. **209**, 211 (2000).

[72] M. T. Lin, C. C. Kuo, J. W. Ho, Y. E. Wu, H. Y. Her, C. S. Shern, and H. L. Huang, Appl. Surf. Sci. **169**, 231 (2001).

[73] P. Bruno, Y. Suzuki, and C. Chappert, Phys. Rev. B **53**, 9214 (1996).

[74] Y. Suzuki, T. Katayama, S. Yoshida, and K. Tanaka, Phys. Rev. Lett. **68**, 3355 (1992).

[75] T. Katayama, Y. Suzuki, H. Awano, Y. Nishihara, and N. Koshizuka, Phys. Rev. Lett. **60**, 1426 (1988).

[76] D. Weller, A. Carl, R. Savoy, T. C. Huang, M. F. Toney, and C. Chappert, J. Phys. Chem. Solids **56**, 1563 (1995).

[77] C. S. Shern, J. S. Tsay, H. Y. Her, Y. E. Wu, and R. H. Chen, Surf. Sci. **429**, L497 (1999).

[78] J. Kim, J.-W. Lee, J.-R. Jeong, S.-C. Shin, Y. H. Ha, Y. Park, and D. W. Moon, Phys. Rev. B **65**, 104428 (2002).

[79] U. Pustogowa, J. Zabloudil, C. Uiberacker, C. Blaas, P. Weinberger, L. Szunyogh, and C. Sommers, Phys. Rev. B **60**, 414 (1999).

[80] J. Kim, J.-W.Lee, J.-R. Jeong, S.-K. Kim, and S.-C.-Shin, Appl. Phys. Lett. **79**, 93 (2001).

[81] N. W. E. Mc Gee, M. T. Johnson, J. J. de Vries, and J. van de Stegge, J. Appl. Phys. **73**, 3418 (1993).

[82] M. Przybylski, L. Yan, J. Zukrowski, M. Nyvlt, Y. Shi, A. Winkelmann, J. Barthel, M. Wasniowska, and J. Kirschner, Phys. Rev. B **73**, 085413 (2006).

[83] H. Fritzsche, J. Kohlhepp, H. J. Elmers, and U. Gradmann, Phys. Rev. B **49**, 15665 (1994).

[84] N. Weber, Diploma thesis, Universität Clausthal-Zellerfeld (1996).

[85] A. Nabok and A. Tsargorodskaya, Thin Solid Films **516**, 8993 (2007).

[86] K. Hild, J. Emmel, G. Schönhense, and H. J. Elmers, Phys. Rev. B. **80**, 224426 (2009).

[87] program code based on transfer matrix calculations, http://www.msd.anl.gov/groups/mf/jmkerrcalc.php.

[88] J. Zak, E. R. Moog, C. Liu, and S. D. Bader, J. Magn. Magn. Mat. **89**, 107 (1990).

[89] U. Gradmann and G. Waller, Surf. Science **116**, 539 (1982).

[90] E. Lundgren, B. Stanka, M. Schmid, and P. Varga, Phys. Rev. B **62**, 2843 (2000).

[91] C.-J. Lin, G. L. Gorman, C. H. Lee, R. F. C. Farrow, E. E. Marinero, H. V. Do, H. Notarys, and C. J. Chien, J. Magn. Magn. Mater. **93**, 19 (1991).

[92] J. Henk and R. Feder, Phys. Rev. B **55**, 11476 (1997).

[93] M. Polyanskiy, http://refractiveindex.info, Refractive index data base.

[94] F. J. Himpsel and D. E. Eastman, Phys. Rev. B **21**, 3207 (1980).

[95] K. Hild, G. Schönhense, H. J. Elmers, T. Nakagawa, T. Yokoyama, K. Tarafder, and P. M. Oppeneer, Phys. Rev. B **82**, 195430 (2010).

[96] P. M. Oppeneer, private communication (2010).

[97] C. Quirós, S. M. Valvidares, O. Robach, and S. Ferrer, J. Phys.:Condens. Matter **17**, 5551 (2005).

[98] A. Grechnev, I. Di Marco, M. I. Katsnelson, A. I. Lichtenstein, J. Wills, and O. Eriksson, Phys. Rev. B **76**, 035107 (2007).

[99] H. Schall, W. Huber, H. Hoermann, W. Maus-Friedrichs, and V. Kempter, Surf. Sci. **210**, 174 (1989).

[100] M. Cinchetti, A. Oelsner, G. H. Fecher, H. J. Elmers, and G. Schönhense, Appl. Phys. Lett. **83**, 1503 (2003).

[101] K. Hild, G. Schönhense, H. J. Elmers, T. Nakagawa, T. Yokoyama, K. Tarafder, and P. M. Oppeneer, in preparation for submission to Phys. Rev. B.

[102] A. Winkelmann, F. Bisio, R. Ocaña, W.-C. Lin, M. Nývlt, H. Petek, and J. Kirschner, Phys. Rev. Lett. **98**, 226601 (2007).

[103] A. Winkelmann, W.-C. Lin, C.-T. Chiang, F. Bisio, H. Petek, and J. Kirschner, Phys. Rev. B **80**, 155128 (2009).

[104] C.-T. Chiang, A. Winkelmann, P. Yu, J. Kirschner, and J. Henk, Phys. Rev. B **81**, 115130 (2010).

[105] C. Boeglin, E. Beaurepaire, V. Halté, V. López-Flores, C. Stamm, N. Pontius, H. A. Dürr, and J.-Y. Bigot, Nature **465**, 458 (2010).

[106] D. Steil, S. Alebrand, T. Roth, M. Krauß, T. Kubota, M. Oogane, Y. Ando, H. C. Schneider, M. Aeschlimann, and M. Cinchetti, Phys. Rev. Lett. **105**, 217202 (2010).

Publications

Part of this work has been published in:

- *Magnetic Circular Dichroism in Two Photon Photoemission*,
  K. Hild, J. Maul, H. J. Elmers, and G. Schönhense, Phys. Rev. Lett. **102**, 057207 (2009).
- *Threshold photoemission magnetic circular dichroism at the spin-reorietation transition of ultrathin epitaxial Pt/Co/Pt(111)/W(110) films*,
  K. Hild, J. Emmel, G. Schönhense, and H. J. Elmers, Phys. Rev. B **80**, 224426, (2009).
- *Energy- and angle-dependent threshold photoemission magnetic circular dichroism from an ultrathin Co/Pt(111) film*,
  K. Hild, G. Schönhense, H. J. Elmers, T. Nakagawa, T. Yokoyama, K. Tarafder, and P. M. Oppeneer, Phys. Rev. B **82**, 195430 (2010).
- *Magnetic circular dichroism in near-threshold photoemission from an ultrathin Co/Pt(111) film at low work functions*,
  K. Hild, G. Schönhense, H. J. Elmers, T. Nakagawa, T. Yokoyama, K. Tarafder, and P. M. Oppeneer, in preparation for submission to Phys. Rev. B.

Further publications:

- *Optical magnetic circular dichroism in threshold photoemission from a magnetite thin film*,
  K. Hild, J. Maul, T. Meng, M. Kallmayer, G. Schönhense, H. J. Elmers, R. Ramos, S. K. Arora, and I. V. Shvets, J. Phys.: Condens. Matter **20**, 235218 (2008).
- *Solid state reaction at the interface between Heusler alloys and Al cap accelerated by elevated temperature and rough surface*,
  M. Kallmayer, K. Hild, T. Eichhorn, H. Schneider, G. Jakob, A. Conca, M. Jourdan, and H. J. Elmers, Appl. Phys. Lett. **91**, 192501 (2007).
- *Magnetic moment investigations of epitaxial magnetite thin films*,
  M. Kallmayer, K. Hild, H. J. Elmers, S. K. Arora, Han-Chun Wu, R. G. S. Sofin, and I. V. Shvets, J. Appl. Phys. **103**, 07D715 (2008).
- *Magnetic and Electronic Properties of Heusler Alloy Films Investigated by X-Ray Magnetic Circular Dichroism*,
  H. J. Elmers, A. Conca, T. Eichhorn, A. Gloskovskii, K. Hild, G. Jakob, M. Jourdan, and M. Kallmayer, Advances in solid state physics **48**,171 (2009).